Aus dem Fachbereich Medizin
der Johann Wolfgang-Goethe-Universität
Frankfurt am Main

betreut am
Zentrum der Pharmakologie
Institut für Klinische Pharmakologie
Direktor: Prof. Dr. Dr. Gerd Geißlinger

The organization of microenvironments by eosinophil granulocytes and macrophages during local inflammation

Dissertation
zur Erlangung des Doktorgrades der theoretischen Medizin
des Fachbereichs Medizin
der Johann Wolfgang-Goethe-Universität
Frankfurt am Main

vorgelegt von
Anja Kolbinger

aus Jena

Frankfurt am Main, 2023

Aus dem Fachbereich Medizin
der Johann Wolfgang-Goethe-Universität
Frankfurt am Main

betreut am
Zentrum der Pharmakologie
Institut für Klinische Pharmakologie
Direktor: Prof. Dr. Dr. Gerd Geißlinger

The organization of microenvironments by eosinophil granulocytes and macrophages during local inflammation

Dissertation
zur Erlangung des Doktorgrades der theoretischen Medizin
des Fachbereichs Medizin
der Johann Wolfgang-Goethe-Universität
Frankfurt am Main

vorgelegt von
Anja Kolbinger

aus Jena

Frankfurt am Main, 2023

Dekan:	Prof. Dr. Stefan Zeuzem
Referent:	Prof. Dr. Klaus Scholich
Korreferent/in:	Prof. Dr. Andreas Weigert
ggf. 2. Korreferent/in:	Prof. Dr. Stefan Offermanns
Tag der mündlichen Prüfung:	11.04.2024

Table of content

1. Zusammenfassung

Eine Entzündung ist ein wichtiger Abwehrmechanismus des Immunsystems, der bei Verletzung oder Infektion aktiviert wird. Hauptziel ist es, die Störungsquelle zu eliminieren, geschädigtes Gewebe zu reparieren und die Homöostase wiederherzustellen. Beginnende Entzündungsprozesse sind durch erhöhten Blutfluss, höhere vaskuläre Permeabilität und die Rekrutierung von Leukozyten und Plasmaproteinen in das Gewebe gekennzeichnet. Eine durch Pathogene induzierte Entzündung löst verschiedene pro- und antiinflammatorische Prozesse aus. Als Reaktion auf den Eindringling werden Immunzellen des angeborenen Immunsystems wie Neutrophile, dendritische Zellen und Monozyten durch residente Gewebezellen und Toll-like-Rezeptoren rekrutiert. Nach dem Übergang vom Blut ins Gewebe reagieren sie auf lokale Signale mit der Freisetzung unterschiedlicher Mediatoren, zytotoxischer Verbindungen, Phagozytose oder Polarisation.

Um lokale durch Pathogene induzierte Entzündungen zu untersuchen, wurde ein Zymosan-induziertes Entzündungsmodell verwendet. Durch Injektion des Pathogens in die Hinterpfoten von Mäusen ensteht eine Toll-like-Rezeptor-2-vermittelte Entzündung. Multi-Epitope-Ligand-Cartography (MELC) wurde verwendet, um sequenzielle Immunhistochemie mit 40 verschiedenen Antikörpern auf dem gleichen Gewebe durchzuführen. Die anschließende bioinformatische Analyse und grafische Darstellung der Ergebnisse zeigten eine spezifische Entzündungsarchitektur, die auf der Polarisation der Makrophagen und ihren zellulären Nachbarschaften basiert. Die Struktur enthält eine Kernregion mit dem Pathogen, eine proinflammatorische Region mit M1 Makrophagen und eine Region mit antiinflammatorischen Zellen. Diese Entdeckung hebt die Koexistenz von pro- und antiinflammatorischen Prozessen während einer laufenden Entzündung hervor und korrigiert das Konzept eines allmählichen zeitlichen Übergangs von proentzündlichen- zu antientzündlichen Vorgängen. Die Durchführung von Durchflusszytometrie mit der gesamten Pfote unterstützte die MELC-Ergebnisse.

Anhand von Eosinophilen wurde die Rolle einer spezifischen Immunzellpopulation in der Entzündungsstruktur zu untersucht. Sie waren in allen drei entzündlichen

Regionen zu finden und passten ihr Zytokinprofil entsprechend ihrer Lokalisation an. Eine Depletion von Eosinophilen mit einem Anti-Siglec F Antikörper reduzierte den Interleukin 4 (IL-4) -Spiegel und erhöhte die Ödembildung sowie mechanische und thermische Hypersensitivitäten während der Entzündungsauflösung.

In Abwesenheit von Eosinophilen lösten sich die pro- und anti-entzündliche Region in der Architektur auf, die Anzahl der Neutrophilen erhöhte sich, und sowohl die Efferozytose als auch die M2-Makrophagenpolarisation wurden reduziert. Die Verabreichung von IL-4 stellte die Architektur vollständig wieder her, normalisierte die Anzahl der Neutrophilen, die Efferozytose und die M2-Makrophagenpolarisation sowie die Auflösung der durch Zymosan verursachten Hypersensitivität. Die Ergebnisse zeigen, dass Eosinophile, die IL-4 exprimieren, die Auflösung der Entzündung unterstützen, indem sie die Entwicklung eines anti-entzündlichen Rahmens ermöglichen, der die pro-entzündliche Region umschließt.

2. Abstract

Inflammation is a crucial host defense mechanism activated in response to injury or infection. Its primary goal is to eliminate the source of the disturbance, repair the damaged tissue, and restore homeostasis. Inflammatory processes can be recognized through increased blood flow, higher vascular permeability, and the recruitment of leukocytes and plasma proteins to the tissue. A pathogen-induced inflammation triggers various pro- and anti-inflammatory processes. Local tissue cells and Toll-like receptors call upon innate immune cells like neutrophils, dendritic cells (DCs), and monocytes to respond to the intruder. They move across the endothelium and respond to local signals by releasing mediators or cytotoxic compounds, phagocytosing, or polarizing.

To study local pathogen-induced inflammation, a zymosan-induced inflammation model was used in the hind paws of mice, which caused a Toll-like receptor 2 mediated inflammation. Multi-Epitope-Ligand-Cartography (MELC) was used for multiple sequential immunohistochemistry with 40 different antibodies on the same tissue. Bioinformatic analysis and graphical representation revealed a specific inflammatory architecture consisting of three major areas based on macrophage polarization and their cellular neighborhoods: a core region containing the pathogen, a pro-inflammatory region containing M1-like macrophages, and a region containing anti-inflammatory cells. This discovery highlights the coexistence of pro- and anti-inflammatory processes during an ongoing inflammation and challenges the concept of a gradual temporal transition from pro- to anti-inflammation. Flow cytometry of the whole paw was performed to support and refine the MELC results.

Eosinophils were used as a specific immune cell population to investigate their role in the inflammatory structure. They were found to be present in all three inflammatory regions, adapting their cytokine profile according to their localization. Depleting eosinophils reduced Interleukin 4 (IL-4)- levels, increased edema formation, and mechanical and thermal hypersensitivities during inflammation resolution. In the absence of eosinophils, pro- and anti-inflammatory region could not be determined in the inflammatory architecture, neutrophil numbers increased, and efferocytosis and M2-macrophage polarization were reduced. IL-4 administration restored these

regions, normalized neutrophil numbers, efferocytosis, M2-macrophage polarization, and resolution of zymosan-induced hypersensitivity. The results show that eosinophils expressing IL-4 support the resolution of inflammation by enabling the development of an anti-inflammatory framework that encloses pro-inflammatory regions.

List of abbreviations

A

AI-region · Anti-inflammatory region

DCs · Dendritic cells

F

FACS · Fluorescence-activated cell scanning

H

HistoCAT: Histology Topography Cytometry Analysis Toolbox ·

I

IFN · Interferon
IL- · Interleukine
ILC · Innate lymphoid cells

M

MAPK · Mitogen-activated protein kinase
MELC· Multi-Epitope-Ligand-Cartography

P

PI-region · Proinflammatory region
PMN · Polymorphonuclear neutrophils

R

ROS · Reactive oxygen species

S

SPADE: Spanning-tree progression analysis of density-normalized events

T

TGF · Transforming growth factor
TLRs · Toll-like receptors

Table of figures

3. Introduction

3.1 Acute inflammation

3.1.1 Initiation of inflammation

Inflammation is an adaptive host defense mechanism triggered through injury or infection. The primary function is to destroy the source of disturbance, remove and repair damaged tissue and finally restore tissue homeostasis[1]. Tissue inflammation can be recognized by typical signs: redness, swelling, heat, pain, and loss of function[2]. An inflammatory process can be divided into acute and stable phases. The acute phase is characterized by an increased blood flow, higher vascular permeability, recruitment of leukocytes, and the movement of plasma proteins to the extravascular tissue[3,4]. The characterizing element of the following stable phase is the development of specific humoral and cellular immune responses against the source of inflammation[5].

The first step of an acute inflammatory response is the initiation phase, which starts with recognizing the disturbance's source. In the case of an infection, pathogen-associated molecular patterns (PAMPs) can be identified by germline-encoded pattern recognition receptors (PRRs) on the surface of different innate immune system cell types. These receptors also react to danger-associated molecular patterns (DAMPs), endogenous molecules that signal tissue damage or necrosis[4]. The pattern recognition receptors can be divided into four significant sub-groups: Toll-like receptors (TLRs), NOD-like receptors (NLRs), RIG-like receptors (RLRs), and C-type lectin receptors (CLRs)[6]. Different inflammatory pathways get activated after ligand binding through one of these receptors. The most common ones are the nuclear factor kappa-B (NF-κB), Mitogen-activated protein kinase (MAPK), and Janus kinase-signal transducer as well as activator of transcription (JAK-STAT) pathways. Their activation produces and releases mediators like cytokines, chemokines, histamine, prostaglandins, and reactive oxygen species (ROS). The release of the different molecules starts a cascade of events, including profound changes in the local environment of the tissue and the vasculature, like enhanced permeability of the capillaries and vascular dilation[7]. These changes lead to

increased migration of leukocytes and plasma flow to the side of inflammation. The leukocytes first to arrive are neutrophils, followed by monocytes which mature into macrophages, DCs and eosinophils. After arriving, the neutrophils and macrophages release many mediators to kill and degrade pathogens before removing them by phagocytosis. After the clearance of the disruption, neutrophils undergo apoptosis and get cleared by macrophages. During the degranulation, the neutrophils release destructive substances for the pathogen and the host[4,8]. To limit the collateral damage to the host, initiating the resolution of inflammation is essential[9] (Figure 1).

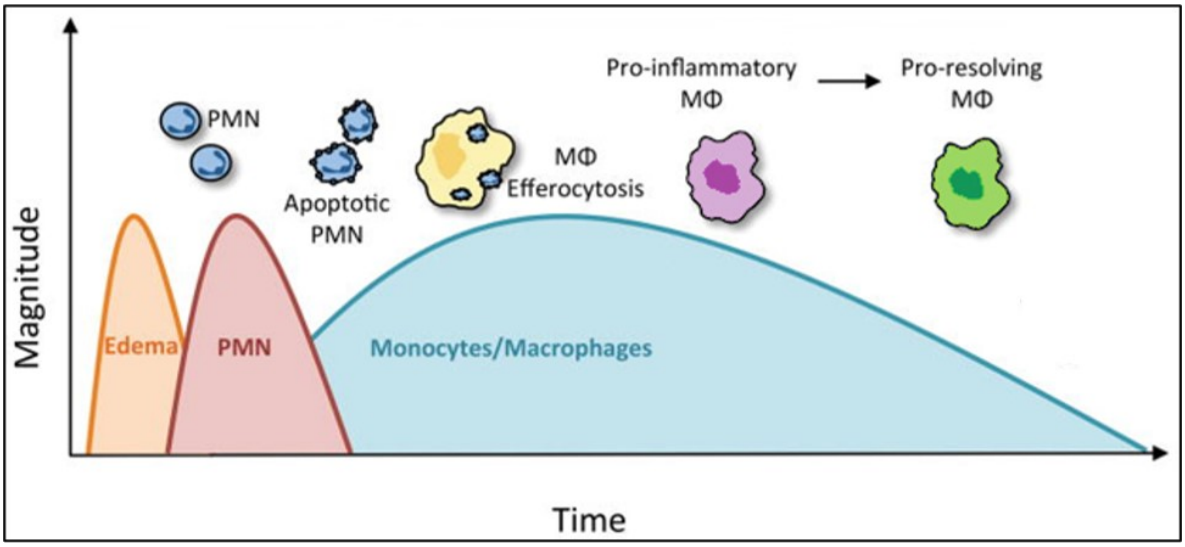

Figure 1: Events during a self-limited acute inflammatory response. The initiation of the inflammation is marked by tissue edema and infiltration of Polymorphonuclear neutrophils (PMN). After the neutrophils, other immune cells, like eosinophils and monocytes, enter the inflammatory tissue. In the resolution phase, the PMN infiltration stops, and the inflammatory site neutrophils undergo apoptosis. The macrophages polarize from a pro-inflammatory to an anti-inflammatory phenotype. Macrophages clear dead neutrophils through efferocytosis. Modified after Sansbury and Spite 2016[10]

3.1.2 Resolution of inflammation

Traditionally resolution of inflammation was seen as a passive process responsible for the end of inflammation. This view has changed in recent years through numerous studies, which could show that resolution is an active process characterized by different events and coordinated through various mediators like the initiation phase of inflammation[11,12].

The elimination of the inciting stimulus is required to resolve acute inflammation effectively. In bacterial infection, the initiation stimulus for resolution is the removal of the pathogen[12]. While neutrophils are the most critical cell type for removing noxious stimuli from the tissue, an exaggerated influx to the tissue can be detrimental. Therefore, their recruitment has to be limited, and the vascular permeability must return to normal to prevent additional income. Neutrophil migration is orchestrated mainly by chemokines, which can be removed by proteolysis and chemokine sequestration. Neutrophils generally have a short life span, regulated by the local inflammatory environment. One possibility are death receptor ligands such as Fas-ligand or TNF (tumor necrosis factor) secreted by macrophages. These mediators can promote neutrophil survival at low concentrations and announce neutrophil death at higher concentrations[13,14]. Additionally, dying neutrophils secrete mediators inhibiting further neutrophil recruitment, such as annexin A1 and lactoferrin, thereby supporting the resolution of inflammation [15,16].

Macrophages phagocytose apoptotic neutrophils to prevent the release of intracellular components by the dying cells. So-called “find me “and “eat me” signals commit macrophages to phagocytose them in a process called efferocytosis[17,18].

Macrophages can polarize towards different phenotypes with specific biological functions in response to stimuli from their microenvironment. The polarization to an anti-inflammatory phenotype is crucial for tissue repair and homeostasis maintenance. Classically activated macrophages also called M1 macrophages, mainly produce pro-inflammatory mediators and eliminate pathogens. During the resolution of inflammation, they differentiate into anti-inflammatory M2-like macrophages. These types of macrophages release anti-inflammatory and pro-resolving mediators, clear apoptotic cells, and regulate tissue repair[19,20]. Prominent

mediators to induce the M2-like phenotype are IL-10, transforming growth factor beta (TGF-β), IL-4, IL-13, and Toll-like receptor agonists. The first two substances also inhibit the production of pro-inflammatory mediators[21,22].

The last step of the resolution phase is the recovery of tissue homeostasis, which requires tissue repair and reestablishing the functionality of the tissue. Therefore, a tight interplay of macrophages, stem and progenitor cells, and stromal cells is necessary to prevent fibrosis or scar formation. Alternatively, activated macrophages play a critical role by secreting the anti-inflammatory mediators IL10, TGF-β, and vascular endothelial growth factor (VEGF) [23].

3.2 Eosinophil granulocytes

3.2.1 Development and general functions

Eosinophils granulocytes are members of the innate immune system. They form approximately 1-3 % of leukocytes in the peripheral blood of humans[24]. Eosinophils differentiate from $CD34^+$ progenitor cells in the bone marrow[25]. Development and maturation of eosinophils under exposure to the myeloid precursors IL-3, granulocyte-macrophage colony-stimulating factor (GM-CSF), and IL-5 last nearly a week. The most relevant mediator for the last stage of differentiation is IL-5. This cytokine also triggers the migration of eosinophils into the circulating blood and is a key factor for eosinophils' survival by preventing apoptosis and promoting cell activation. Significant sources of IL-5 are CD34+ progenitor cells, group 2 innate lymphoid cells (ILC-2), Th2 lymphocytes, invariant natural killer T cells, and mast cells. In an auto/paracrine manner, eosinophils can also release IL-5 by themselves [26,27]. Within 8-12 hours after the release from the bone marrow, eosinophils get recruited to the tissue by eotaxins. Humans express CCL-11, CCL-24, and CCL-26, which bind to the chemokine receptor CCR3 on the surface of the cells[28]. In mice, only the first two can be found[29]. Additional eosinophil chemoattractants are CCL5 and lipid mediators such as leukotriene B4 and prostaglandin D2[30]. Eosinophils exert different homeostatic tasks in several primary and secondary lymphoid organs, for example, the thymus, lymph nodes, spleen, gut, lung, and uterus. They promote plasma cell survival, regulate the physiological balance between T-helper cells and

regulatory T-cells, perform antigen presentation, and contribute to tissue repair[31,32]. A primary or secondary increase in the circulating number of eosinophils and inflammation-induced surges cause the migration of eosinophils to no physiologically homing tissues[33]. When the absolute count of eosinophils exceeds 450-500 cells/µl blood in humans, it is referred to as eosinophilia, and counts over 1500 cells/µl as hypereosinophilia[34] or Hypereosinophilic syndrome. The patients show various symptoms, including skin rashes, dizziness, memory loss, cough, fatigue, fever, and shortness of breath caused trough eosinophilic inflammation in different body parts leading to organ dysfunction[35]. The preferential target for this type of inflammation is the heart. But also several other tissues as the skin, the esophageal mucosa, parts of the gastrointestinal tract, central or peripheral nerves, blood vessels, and the upper and lower airways, can be affected by different diseases caused by eosinophil infiltration[36,37].

3.2.2 Role during local inflammation

The characteristic of eosinophils is their secretory vesicles called specific granules. These produce various cytokines, chemokines, and growth factors (Figure 2). Also, the four major granule proteins eosinophil cationic protein (ECP), eosinophil-derived neurotoxin (EDN), eosinophil peroxidase (EPO), and major basic protein (MBP) are stored in the granules. All four have cytotoxic effects on pathogens and host tissue[38]. Degranulation and release of mediators are tightly regulated. Instead of a complete degranulation and parallel release of all substances, only small quanta of selected cytotoxins are released in the extracellular space with the help of the so-called sombrero vesicles. This process of limited and selective release of mediators is termed “piecemeal degranulation.” Eosinophils can hold the content of the granules during their whole lifespan and replenish missing mediators[39]. Besides the granules and sombrero vesicles, eosinophils also have lipid bodies. These cell compartments are the place of synthesis for numerous lipid mediators like leukotrienes, thromboxane, and prostaglandins. On the surface, eosinophils carry multiple receptors, including chemokine receptors, Fc receptors, pattern recognition receptors, receptors for lipid mediators, cytokine receptors, complement receptors,

and adhesion receptors (Figure 2)[36]. During inflammation, eosinophils can have very different functions. Similar to neutrophils, they can kill invading pathogens in different ways: the release of their cytotoxic substances, by degranulation, by performing a respiratory burst, or through extracellular DNA trapping. Eosinophils are also capable of phagocytosing the intruders and killing them intracellularly. However, they are less effective in fulfilling these tasks than neutrophils[40,41]. Like macrophages, eosinophils express surface components that are required for antigen presentation. Additionally, they can process antigens and stimulate T-cells, resulting in T-cell proliferation and cytokine release[42]. Eosinophils interact intensively with Type 2 immune cells. These cells can stimulate eosinophils through the release of IL-5 or by promoting the production of IgE through a humeral adaptive immune response. Activated mast cells can also release chymase, which prevents eosinophils from undergoing apoptosis. Conversely, Eosinophils can maintain and exacerbate Type 2 immune responses by providing plasma cells with survival factors[43].

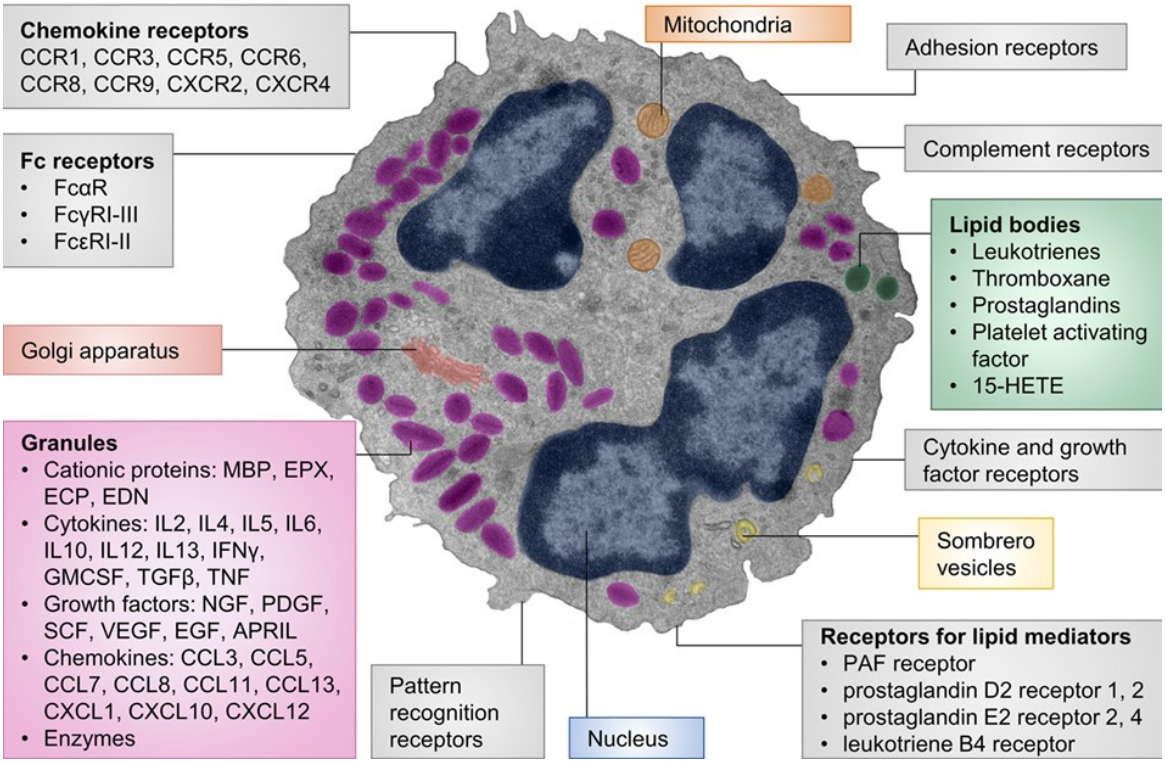

Figure 2: Cellular structure, receptors, and mediators of eosinophils.
Characteristic features of eosinophils are the multilobed nucleus, specific eosinophil granules, lipid bodies, and sombrero vesicles. They produce and release mediators like cationic proteins, cytokines, growth factors, chemokines, enzymes, and lipid mediators. On the cell surface numerous receptors, including chemokine receptors, Fc receptors, pattern recognition receptors, receptors for lipid mediators, cytokine receptors, complement receptors, and adhesion receptors, are expressed. Modified after Diny et. Al 2017[36].

3.3 Macrophages

Macrophages are myeloid immune cells classified together with monocytes and DCs as part of the mononuclear phagocyte system[44–46]. Macrophages can be divided into monocyte-derived macrophages and tissue-resident macrophages. Monocytes maturate from progenitor cells in the bone marrow and enter the peripheral blood, representing between 4-10% of nucleated cells in healthy humans[47]. During homeostasis and inflammation, they migrate into the tissue, differentiating into macrophages through exposure to local growth factors, cytokines, and microbial products[48]. Most tissue-resident macrophages are derived from the yolk sac during embryonic development and are seeded before birth. They have self-renewal capacities and are independent of monocytes[49]. Both types of macrophages coexist in different tissues; each organ has a unique combination. The primary function of tissue-resident macrophages is tissue remodeling, while monocyte-derived macrophages primarily assist in host defense[46,50]. Examples of specialized tissue-resident macrophages with different functional phenotypes based on their anatomical location are the microglia in the central nervous system, osteoblasts in the bone, alveolar macrophages in the lung, and Kupffer cells in the liver. Such distinct macrophages reside in immune-privileged tissues where they engulf dead cells and invading pathogens, orchestrate the immune response, and recruit additional macrophages[51,52].

Macrophages are highly plastic cells that can change their phenotype in response to their surroundings and the local cytokine milieu[53]. Based on their cell surface markers, biological activities, and production of specific mediators, several classes of macrophages have been described in humans and mice. They can be classified in two idealized phenotypes, the classically activated M1 macrophages and the alternatively activated M2 macrophages (Figure 3). Between these two idealized classes, macrophages exist in numerous phenotypes labeled M1-like or M2-like macrophages. The according expression changes leading to the development of these phenotypes are called macrophage polarization[54,55]. M1-like macrophages can be induced through Th1 cytokines like Interferon (IFN)-γ and TNF-α or bacteria

or lipopolysaccharide (LPS) recognition. They produce and secrete high levels of the pro-inflammatory cytokines TNF-α, IL-1α, IL-1β, IL-6, IL-12, IL-23, and cyclooxygenase-2 (COX-2), and low levels of IL-10. These macrophages participate in removing pathogens through infection, show robust anti-microbial and anti-tumoral activities, mediate ROS-induced tissue damage, and impair tissue regeneration and wound healing[54–56]. M2-like macrophages instead prevent irrecoverable tissue damage and ongoing stable inflammation. These anti-inflammatory macrophages can be polarized through different pathways by Th2 cytokines. IL-4 and IL-13 can activate STAT6 through the IL-4 receptor alpha (IL-4Rα), while IL-10 can bind to the IL-10 receptor (IL-10R) and activate STAT3. Additional cytokines which drive the M2-like polarization are IL-33 and IL-21[57–59]. M2 macrophages produce mainly anti-inflammatory cytokines like IL-12, IL-10, and TGF-β. They phagocytose apoptotic cells and cell debris, promote tissue repair and wound healing and show pro-angiogenic and pro-fibrotic properties. Therefore, this type of macrophage plays a role in Th2 responses, parasite clearance, tissue remodeling, and angiogenesis. Also, they mitigate inflammation and participate in immunoregulation and tumor formation and progression[58–61]. However, the separation in M1-like and M2-like macrophages is very flexible and can change radically depending on the incoming signals from their microenvironment.

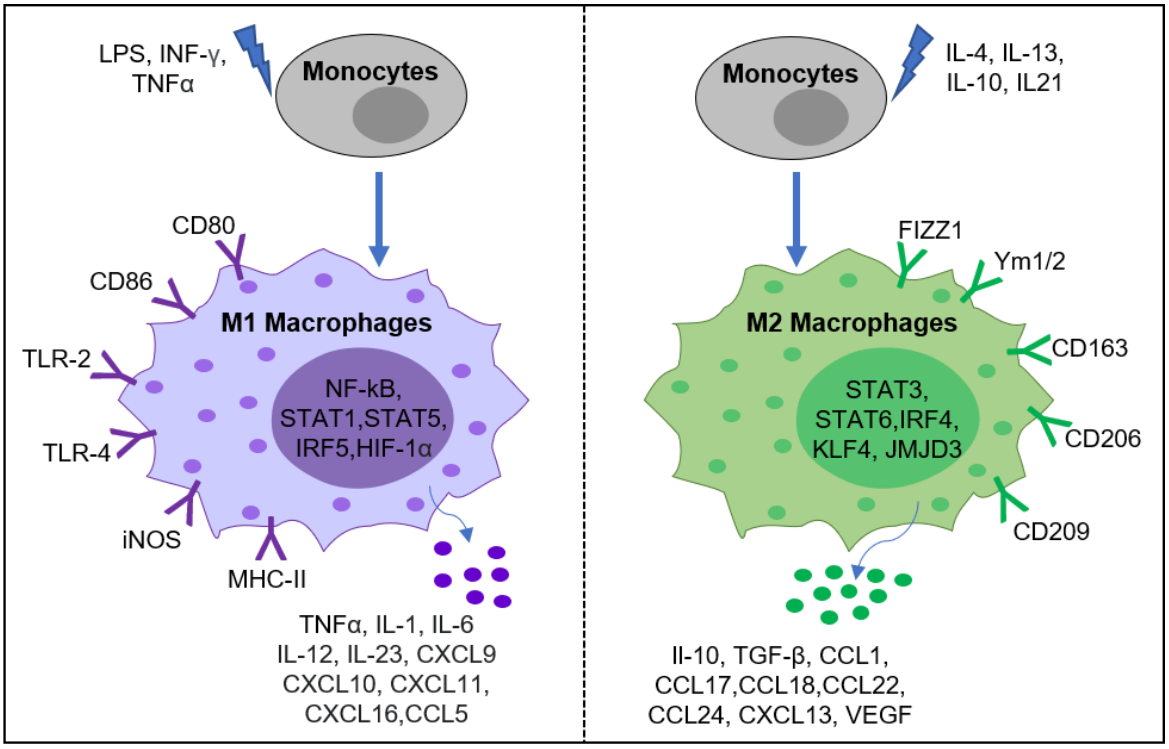

Figure 3: Schematic view of macrophage polarization. Monocytes differentiate into macrophages after entering the tissue. These macrophages can polarize through different specific microenvironments in pro-inflammatory M1 macrophages or anti-inflammatory M2 macrophages. Both subsets express other surface markers and release various mediators through the activation of additional transcription factors[62]

3.4 Aim of the thesis

The acute inflammatory response can be divided into initiation and resolution. The initiation phase is characterized by the rapid infiltration of PMNs and edema formation in response to injury. In the resolution phase, PMNs undergo apoptosis and are ingested by macrophages that emigrate rapidly from the inflamed site to the draining lymph nodes. After the onset of inflammation, neutrophils and eosinophils are among the first cell types recruited to the tissue, followed by some delay by monocytes and DCs. Once crossing the endothelium and entering the inflamed tissue, the immune cells react according to the signals they receive from their microenvironment. The recruited monocytes differentiate into macrophages and polarize towards M1-like or M2-like phenotypes depending on their microenvironment. Various receptors control the exact positioning of macrophages within the inflamed tissue and decide their polarization. While the regulation of the activity of immune cells is well investigated, their localization during inflammation and their spatial relationships to each other are less well understood. To elucidate the structure of a pathogen-caused inflammation, zymosan was used to induce a TLR-2 mediated local inflammation in the hind paws of mice. The collected tissue was analyzed with MELC.

Aim 1 was to develop a bioinformatical analysis pipeline for the data generated with the MELC method and a graphical representation to display the results (Figure 4 part 1). The main steps of the developed pipeline are image generation and processing, image correction, and single-cell extraction, followed by single-cell analysis and, finally, analysis of the neighborhood and network.

In Aim 2, we used the here established analysis methods to investigate the positioning of the immune cells in the inflamed paw and to define an inflammatory structure based on the specific microenvironment they form (Figure 4 part 2).

Aim 3 was to study the role of eosinophils during local inflammation and their interactions with different immune cells (Figure 4 part 3) to characterize the influence of a single immune cell type on the course of inflammation. Therefore, eosinophils were depleted with an anti-Siglec F antibody before injecting the pathogen.

Afterward, paw tissue, blood, and bone marrow were investigated with Flow Cytometry or MELC and the developed analysis pipeline.

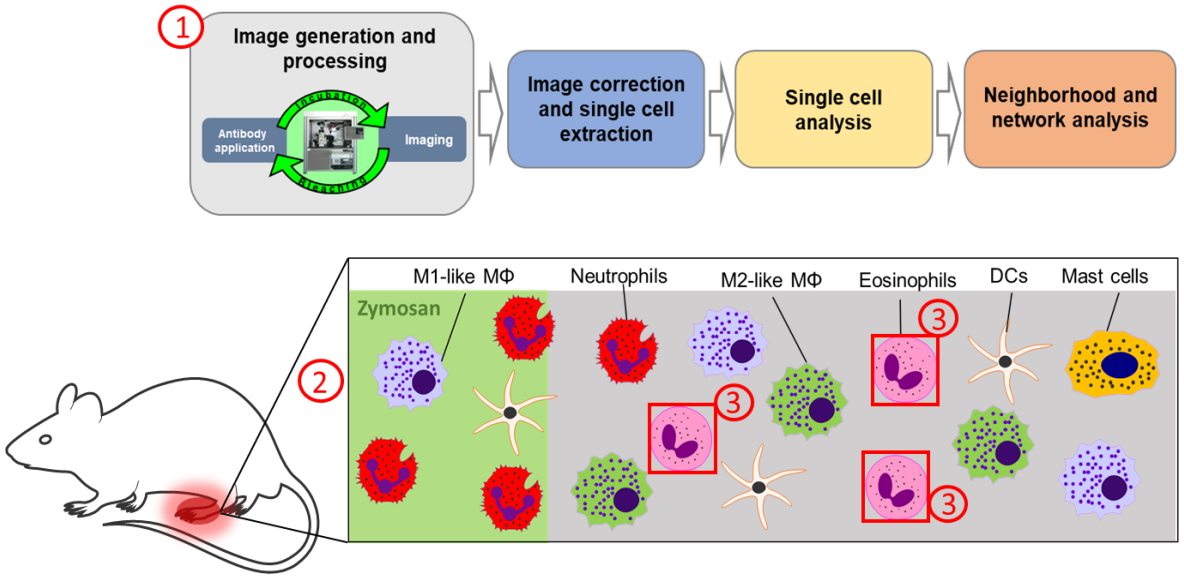

Figure 4: Aims of the thesis. Aim 1 is the development of a bioinformatical analysis pipeline for images generated with the MELC. Aim 2 investigates the positioning of different immune cell types in local zymosan-induced inflammation. Aim 3 is the analysis of the function of eosinophils and their interactions with various immune cells in this inflammation model.

4. Results

4.1 Establishing a bioinformatic pipeline for the analysis of the microenvironments of immune cells

MELC is an automated imaging method that allows visualizing an unlimited number of fluorescence-labeled antibodies on the same tissue slide. During an automated procedure, the tissue sample is incubated with the antibody, which is washed away afterward with PBS. After the incubation time, phase contrast and fluorescence images are taken. A bleaching step with high-intensity light is performed to delete the antibody's fluorescence signal later. After recording the post-bleaching image, the next antibody is applied, and the process is repeated. The first step of this thesis was to establish antibody panels to detect immune and non-immune cells in zymosan-induced paw inflammation. Therefore, different antibodies in different concentrations were tested on the paw tissue of the mice. Afterward, the order of the antibodies during the MELC run was tested and determined, which considers the antibodies' individual stability. After the MELC run ended, all fluorescent images representing the antibodies used during the run were aligned pixel-wise, and illumination faults were corrected by flat-field correction. The postbleaching images were subtracted from the subsequent fluorescence image to exclude autofluorescence and the remaining fluorescence of the previous antibody. In the next step, ImageJ v1.52 (NIH, Bethesda, MD, USA) was used to remove noise, background fluorescence, and artifacts from all subtracted grayscale images.

All further analyses of the data were based on single-cell phenotyping. Therefore, a mask was generated to define which object should be treated as cells. To achieve accurate results, the propidium iodide signals, which mark nuclei, were combined with signals for CD45, which is expressed in the cell membrane of all immune cells in the mouse paw. For mask generation and additional illumination correction of all greyscale images, Cell Profiler v4.2.1 was used. In the next step, all antibody images and the corresponding segmentation mask were imported into the Histology Topography Cytometry Analysis Toolbox (HistoCAT) v1.76 for analyzing the phenotype of the immune cells. All images, excluding those used for single-cell mask generation, were z-score normalized. The cells are then sorted based on their

similarity using the Barnes-Hut-t-SNE (BH-t-SNE)[63], which reduces high-dimensional data into two dimensions. A higher proximity in the t-SNE plot indicates a more similar marker expression (Kolbinger, Kestner et al. 2022, Figure 3C). PhenoGraph sorts single cells based on the single-cell mask and marker colocalization (k set between 10 and 30) and put similar cells in clusters visible in a colored heatmap. The resulting groups were determined based on marker expression and classified as different immune cell types.

The number of objects in every cluster was normalized to the total number of objects in the cell mask to calculate the relative number of cells per immune cell type (Kolbinger, Kestner et al. 2022, Figure 4C, 5B). The neighborhood analysis implemented in HistoCAT was used under standard conditions to investigate the spatial relationships between the clusters. During this analysis, pairwise interactions between cell phenotypes were calculated for each cell and its neighbors, defined as objects at a maximum distance of four pixels. They were compared to a randomized version of the cell distribution. This permutation test indicated a significant interaction, no likelihood of exchange, or avoidance between cell phenotypes. The results were displayed in a heatmap with three different colors (Kolbinger et al. 2023, Figure S4). To display the relative distance between specific immune cell types, Cytoscape v3.8.2 or Excel were used to generate dual-centered neighborhood networks or relative distance maps. Therefore, the results of the neighborhood analysis were assigned a score of 0–100 before importing them into the program (Kolbinger, Kestner et al. 2022, Figure 6A). To further separate the immune cell types identified with HistoCAT, we used spanning-tree progression analysis of density-normalized events (SPADE) in MATLAB. This algorithm views single-cell data as a high-dimensional point cloud and places the density-normalized events on spanning trees (Kolbinger, Kestner et al. 2022, Figure 3D).

The here developed analysis pipeline (Figure 5) allows the analysis of the MELC data in a relatively short time. All datasets were analyzed with the same algorithms and parameters, evaluating the results objective and reproducible.

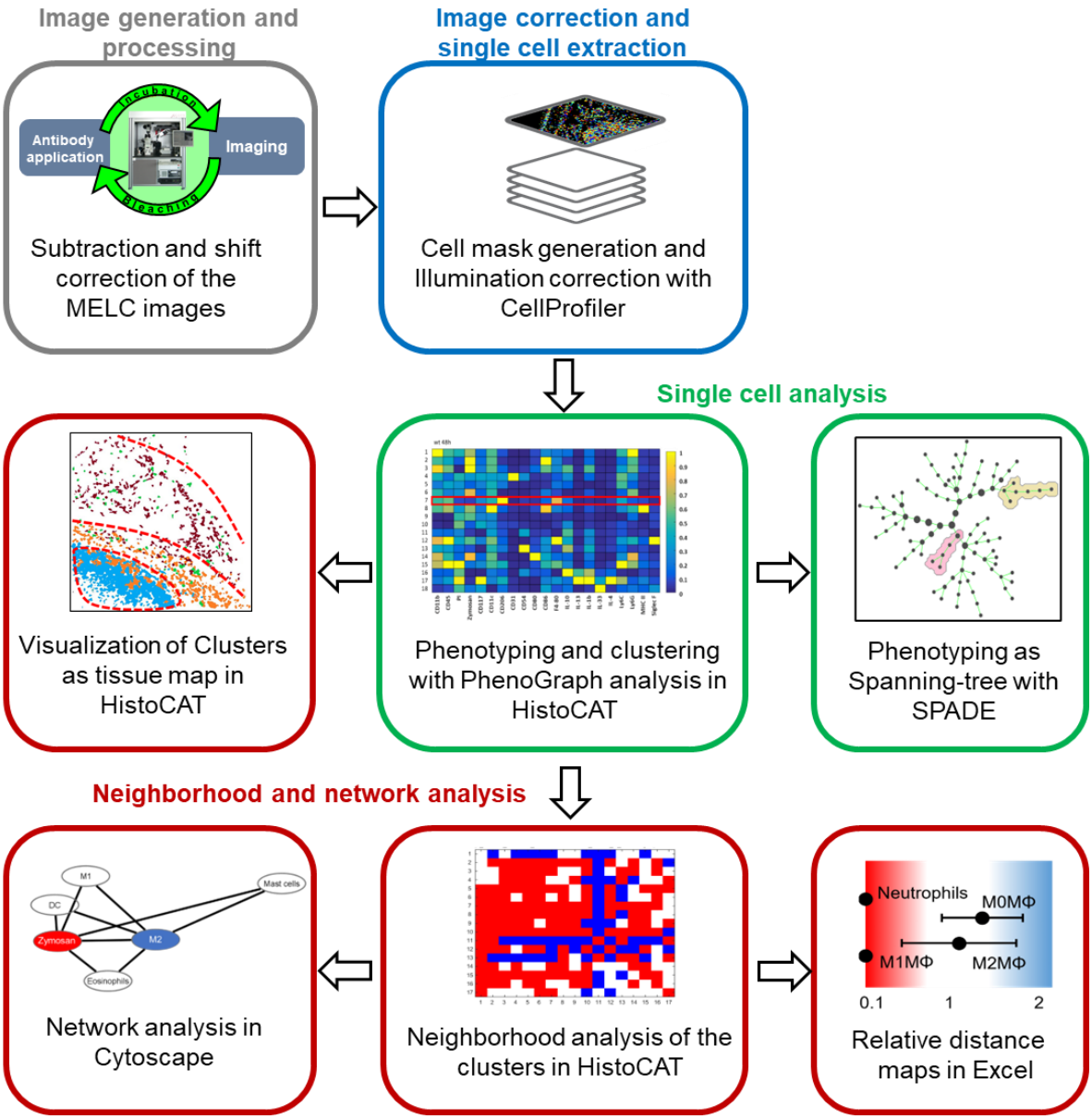

Figure 5: Workflow of the bioinformatic analysis of the MELC images. After generating the images using the MELC technology, all images were processed to remove false fluorescent signals and perform shift correction. Afterward, image correction and generation of a cell mask for a single cell extraction were performed using CellProfiler. The PhenoGraph algorithm in HistoCAT and SPADE was used for single-cell analysis. The neighborhood and the network of the clusters from the PhenoGraph analysis were investigated using HistoCAT, Excel, and Cytoscape.

4.2 During local inflammation, a basic inflammatory structure is formed based on the immune cell distribution

To induce a TLR-2-mediated innate immune response, the TLR-2 agonist zymosan was injected into the hind paw of male C57BL/6J mice. Due to its particulate structure, zymosan is immobilized at the injection site, and after labeling with FITC, its exact localization in the tissue can be determined. The MELC technology and the developed bioinformatic pipeline were used to identify and localize the cells in the inflamed tissue at different time points after the zymosan injection. The most abundant immune cells 24 hours after the zymosan injection were macrophages, neutrophils, eosinophils, DCs, and mast cells. ILCs, NK-cells, and cells of the adaptive immune system, like T-cells and B-cells, could not be distinguished (Kolbinger et al. 2023, Figure 2A). Macrophages could be divided into three subtypes based on their phenotype: undifferentiated M0 macrophages ($F480^+/CD86^+/CD206^+$), M1-like macrophages ($F480^+/CD86^+/CD206^-$), and M2-like macrophages ($F480^+/CD86^-/CD206^+$). Polarization of undifferentiated M0 macrophages started eight hours after injection of the pathogen to the M1-like macrophages and after 24 h to M2-like macrophages. This time course was visible in the analysis of the MELC data (Kolbinger et al. 2023, Figure 1A-D) and FACS analysis of the whole inflamed paw (Kolbinger et al. 2023, Figure 1E-H).

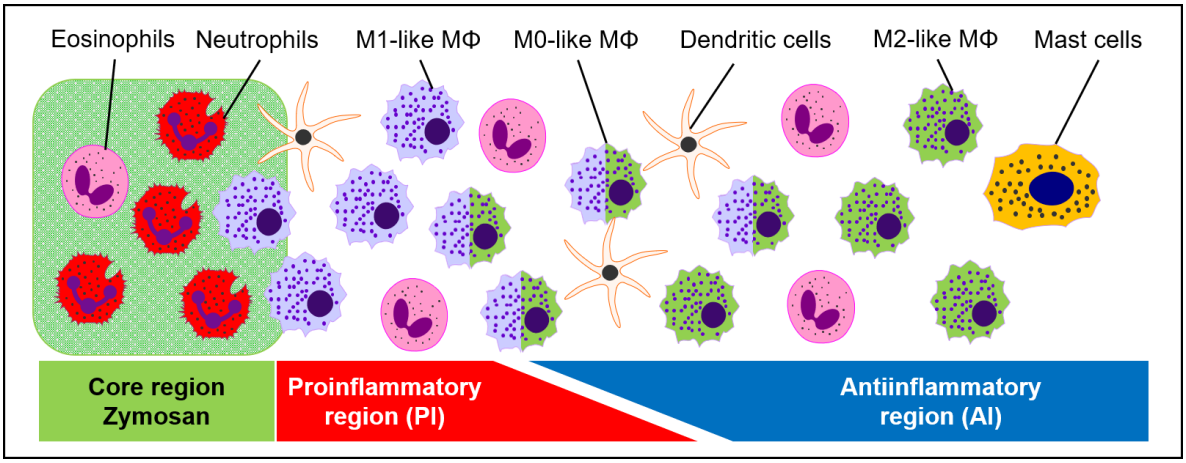

Figure 6: Schematic representation of the inflammatory structure. Based on the zymosan and the distribution of the macrophages, an inflammatory structure with three different regions was defined. 1. Core region defined through zymosan contains neutrophils, eosinophils, and some M1-like macrophages. 2. Pro-inflammatory region (PI-region), dominated by M1-like macrophages, contains DCs, eosinophils, and M0 macrophages. 3. Anti-inflammatory region (AI-region) dominated by M2-like macrophages contains DCs, eosinophils, M0 macrophages, and mast cells.

The macrophage subtypes in the fluorescent images showed a specific arrangement in the inflamed tissue within and adjacent to the zymosan-containing area (Figure 6). Starting 24 h after zymosan injection, the M1-like macrophages were located in the zymosan-covered area or nearby. The M2-like macrophages, in contrast, were at a greater distance from the zymosan (Kolbinger et al. 2023, Figure 1A). The neighborhood analysis was used to determine the likelihood for the macrophage subtypes to be a direct neighbor of zymosan compared to a randomized version of the same tissue. The result of this analysis was a defined pattern with M1-like macrophages as significant neighbors of zymosan and M2-like macrophages, which were significantly not neighbored, while M0 macrophages were randomly distributed. This structure appeared 24 h after the pathogen injection and was still stable 48 h later (Kolbinger et al. 2023, Figure 1I). The pathogen zymosan and the M2-like macrophages formed the external borders of the inflammation. Analyzing the positioning of the other immune cell types in the inflamed tissue, a neighborhood analysis with zymosan or M2-like macrophages as reference points were performed. The results show that besides the M1-like macrophages also, neutrophils, eosinophils, and DCs were direct neighbors of zymosan. Apart from neutrophils,

these cell types were also in the immediate neighborhood of M2-like macrophages, together with CD117-positive mast cells. The neighborhood scores were used to make a combined dual-centered network showing the positioning of the different immune cell types to zymosan and M2-like macrophages (Kolbinger et al. 2023, Figure 2B-D). Based on this network and the cell clusters of the major immune cell types, three inflammatory regions were defined (Figure 6). The first is the core region based on the distribution of the zymosan particles. The neutrophils and some M1-like macrophages dominate this region. The second region is the pro-inflammatory region (PI-region) formed by the M1-like macrophages outside the core region. The anti-inflammatory region (AI-region) is defined by M2-like macrophages and borders at the PI-region. Mast cells were only found in this region, while eosinophils and DCs were spread over all three areas (Kolbinger et al. 2023, Figure 2E).

4.3 Eosinophil Granulocytes influence the formation of the inflammatory structure and resolution of inflammation

Examining the inflammatory structure showed that eosinophils were spread over all three inflammatory regions in pro- and anti-inflammatory microenvironments. To investigate the role of the eosinophils during the establishment of the inflammatory structure and the interactions with pro- and anti-inflammatory immune cells, MELC-analysis was performed at different time points after zymosan injection. The MELC data were further analyzed with SPADE to test whether distinct eosinophils phenotype can be detected. The resulting SPADE trees showed three eosinophil subtypes. In the onset of inflammation four hours after zymosan-injection, only one significant population of eosinophils was visible. This population was defined through the expression of the eosinophil marker Siglec F and the interleukins IL-4, IL-6, IL-10, and IL-13. At 24 h, when the inflammatory structure had been established, two distinct groups of eosinophils could be detected. They expressed either IL-4 and IL-13 or IL-6 and IL10. Four hours after injecting the pathogen, the IL-4-positive eosinophil subtype was visible inside and outside the core region. However, 24 h after zymosan injection, the IL4-expressing eosinophils vanished entirely from the core region and were only visible in the PI and AI region. In the latter, 60% of the

eosinophils expressed IL-4, while only 25 % of the IL-4-positive eosinophils were detectable in the PI region (Kolbinger et al. 2023, Figure 3).

In the next step, eosinophils were depleted with an anti-Siglec F antibody injected 24 h before the pathogen to examine the function of the eosinophils during inflammation. The depletion was confirmed by FACS analysis in the blood and paw of the treated mice. In the control group injected with an IgG2A antibody instead of the anti-Siglec F antibody, eosinophils recruited to the tissue were initially high. They started decreasing eight hours after the zymosan injection. After treatment with depletion antibody, the eosinophil number was significantly reduced by around 90 % in blood and whole paw tissue up to 48 h after zymosan injection (Kolbinger et al. 2023, Figure 4A-C). Importantly, in the MELC images, no eosinophils were detectable in the core-, PI-, and AI-region. To see the influence of the depletion on the course of inflammation, edema measurement, and behavioral tests were performed (Kolbinger et al. 2023, Figure 4D-F). While the eosinophil depletion did not alter the onset of edema formation and its maximal size, the resolution of the edema was significantly delayed by the injection of the depletion antibody. Eosinophil depletion also caused a delayed resolution of zymosan-induced mechanical and thermal hypersensitivities without affecting the onset or the maximal responses. Since 24 h after zymosan injection, edema formation and hypersensitivities showed significant differences between the isotype control and the anti-Siglec F antibody-treated mice, this time point was chosen for further analysis. The inflammatory structure in the paws of eosinophil-depleted mice showed a breakdown of the borders between the PI and AI region. In these mice, M1-like and M2-like macrophages were evenly distributed around the core region with the zymosan (Kolbinger et al. 2023, Figure 5A).

The difference in the positioning of the M2-like macrophages compared to the control was also visible in the neighborhood analysis for zymosan. Here, the relative distance score was decreased, leading to the M2-like macrophages being rated as random neighbors of zymosan. The dual-centered networks of zymosan and M2-like macrophages showed a shorter distance between the two centers, zymosan, and

M2-like macrophages, and reduced relative distances for all observed immune cells toward a direct neighborhood (Kolbinger et al. 2023, Figure 5B).

Quantifying the different immune cell types visible in the MELC analysis showed a reduced number of M2-like macrophages and a reduced efferocytosis capacity of all macrophages in the mice with eosinophil depletion. At the same time, the number of free neutrophils increased (Kolbinger et al. 2023, Figure 5 C-I). Measurement of different chemokines, cytokines, and Interleukins in the inflamed paws showed that Eosinophil depletion caused the upregulation of TNFα and the neutrophil-attractant chemokines CXCL1, CCL-2, CCL-3, CCL-4, CCL-5, and CCL-11 (Kolbinger et al. 2023, Figure 7A). The only mediator, which was reduced in the absence of eosinophils, was IL-4 (Kolbinger et al. 2023, Figure 6A). Therefore, mice were injected with the depletion antibody anti-Siglec F and a stabilized form of IL-4 (IL-4c) before the zymosan-injection. The other group was injected with IL-4c alone. The behavioral test with all four groups (+/- anti-Siglec F antibody and +/- IL-4c) showed that the delayed resolution of thermal hypersensitivity caused by Eosinophil depletion could be avoided by treatment with IL-4c (Kolbinger et al. 2023, Figure 8C). Mice treated with the depletion antibody and IL4-c showed no significant differences from those with the IL-4c single treatment.

Furthermore, MELC analysis showed that IL-4c treatment restored the inflammatory structure of the core, PI region, and AI region (Kolbinger et al. 2023, Figure 8A-B). To quantify the number of different immune cell types in the whole inflamed tissue, FACS analysis of the mouse paws was performed. As seen in the MELC analysis, mice treated with the anti-Siglec F antibody showed an increased number of neutrophils, fewer M2-like macrophages, and a reduced efferocytosis capacity of all macrophages compared to the control mice. However, the survival rate of neutrophils and the amount of all macrophages in the tissue were not altered. Notably, the effect of the depletion antibody on neutrophil numbers, efferocytosis, and M2-like macrophage numbers was reversed by IL-4c treatment. Compared with the IgG2A-treated control mice, all mice treated with IL4-c showed a slight shift towards M2-like macrophage polarization and a higher amount of M0 macrophages

while the number of M1-like macrophages was reduced (Kolbinger et al. 2023, Figure 6B-F, Figure 7B-E)

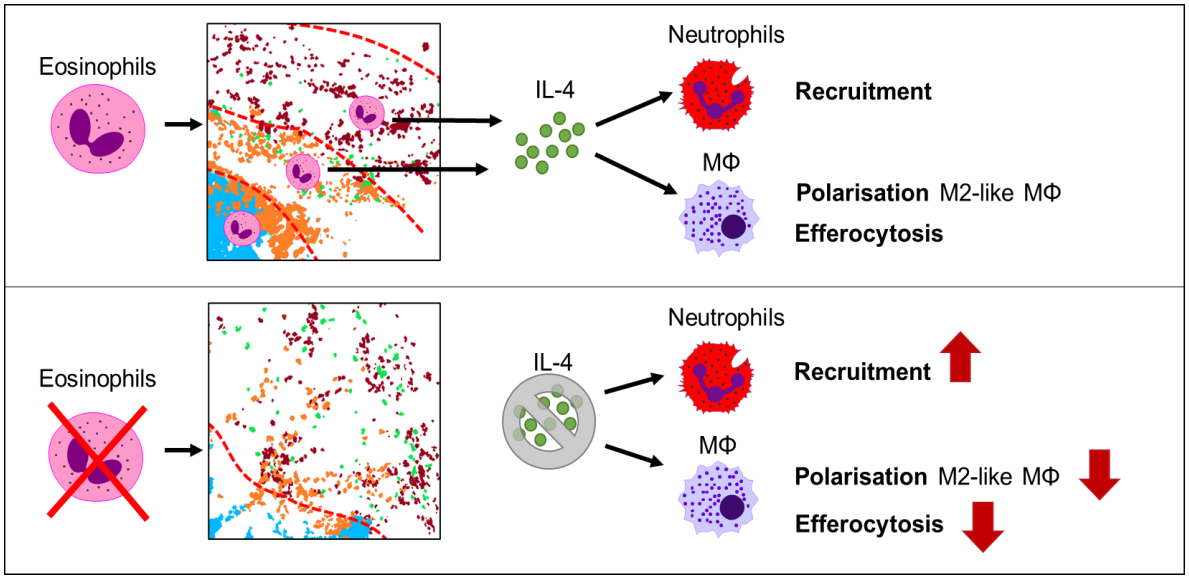

Figure 7: Role of eosinophils during a zymosan-induced local inflammation. Eosinophils can be found in all three inflammatory regions, adapted to their surrounding by downregulating IL-4 in the core region, indicating environment-specific eosinophil subtypes. The secretion of IL4 in the PI-region and AI-region influences the recruitment of the neutrophils, the efferocytosis, and the polarization of the macrophages. Depletion of eosinophils caused a breakdown of the inflammatory structure and led to increased recruitment of the neutrophils and decreased polarization and efferocytosis of the macrophages.

5. Discussion

A local inflammation induced by a pathogen involves various pro- and anti-inflammatory processes that detect and remove the disturbance's source, eventually causing the resolution of inflammation and tissue repair. A complex innate immune response is started after recognizing the intruder by local tissue cells and Toll-like receptors. Local and blood-derived innate immune cells like neutrophils, eosinophils, DCs, and monocytes are recruited to the tissue. After crossing the endothelium, immune cells react to signals from their direct surroundings, the microenvironment, with cell-specific responses such as releasing mediators, cytotoxic compounds, phagocytosis, or polarization. Similar microenvironments form together higher-ranking regions, which build the architecture of an inflammation. It is essential to understand the role of the different immune cells during the inflammation and to uncover the reasons for a failure of the inflammatory response leading to chronic inflammation. Therefore, more information about the mechanisms driving inflammatory regions' formation, maintenance, and interaction is necessary. This thesis aimed to identify the development of microenvironments and their care through the course of a TLR- 2 mediated inflammation. Eosinophils were used to determine the effect of different microenvironments on a specific immune cell type. The relevance of single immune cell types for the formation of microenvironments and the resolution of inflammation was investigated through the depletion of eosinophils.

5.1 Visualization and analysis of microenvironments

Knowledge about the formation of microenvironments and their role in inflammation is very rudimentary because of the lack of methods for investigation. Most techniques for quantifying immune cells, like FACS analysis, require tissue destruction, which leads to the loss of information about the microenvironments. Classical immunohistochemistry can be used to visualize the amount and the localization of an immune cell type in the tissue. However, due to the limitation of using only 3-5 markers on the same tissue slide, information about the composition

of the specific environment around each cell and the interaction of two or more microenvironments with each other is very limited. In addition, serial staining of consecutive tissue slices does not solve this problem satisfactorily since not every slide will contain the same cells and therefore lacks the necessary single-cell data in combination with information about the direct neighbors of specific immune cells. Consequently, only a vague idea of the composition of particular microenvironments was available. Because of this, different multiplex tissue imaging methods have been developed in the last years, such as Cyclic Immunofluorescence (CyCIF)[64], Multiplex Immunohistochemistry (mIHC)[65], Imaging Mass Cytometry (IMC)[66], Multi-Epitope-Ligand-Carthography (MELC)[67], Multiplexed Immuno-fluorescence (mxIF)[68], Co-detection by indexing (CODEX)[69], and MIBI Multiplexed Ion Beam Imaging (MIBI)[70]. The basis of these methods is antibody staining combined with either fluorescence microscopy or imaging mass spectrometry. Cyclic imaging or multiple rounds of staining are used to achieve many different stains on the same tissue slide. The MELC was used in our case, which uses fluorescence microscopy in different staining rounds. In between, the fluorescence tags are removed through bleaching with bright light. The new multiplex imaging approaches generate big datasets which require further analysis methods and analytical tools, as well as new best practice guidelines and standards for data generation, storage, and reproducibility[71,72]. A first approach is suggested in “The minimum information guidelines for highly multiplexed tissue images” (MITI) [73] and “Multiple Choice MICROscopy” (MCMICRO), which is a bioinformatical end-to-end pipeline that transforms pictures in single-cell data and provides different algorithms for data analysis. A toolbox for quantitative analysis of multiplexed imaging data but not a complete analysis pipeline is HistoCAT, used during this thesis[74]. As it is necessary to choose specific antibodies for the different multiplex technologies and to validate the used antibody panels separately for every kind of tissue, it is difficult to give general advice, which sets the barrier high for new users. The same problem exists for bioinformatic analysis of the generated data, which must be adjusted precisely to the used tissue type. Therefore, the project’s first step was establishing a suitable antibody panel and developing a bioinformatical pipeline (Figure 8). All the programs we used in our pipeline are freely available,

making our data analysis method readily available. The pipeline was successfully used on paw tissue (Kolbinger et al. 2023) and post-stroke brain tissue (Kolbinger, Kestner et al. 2022).

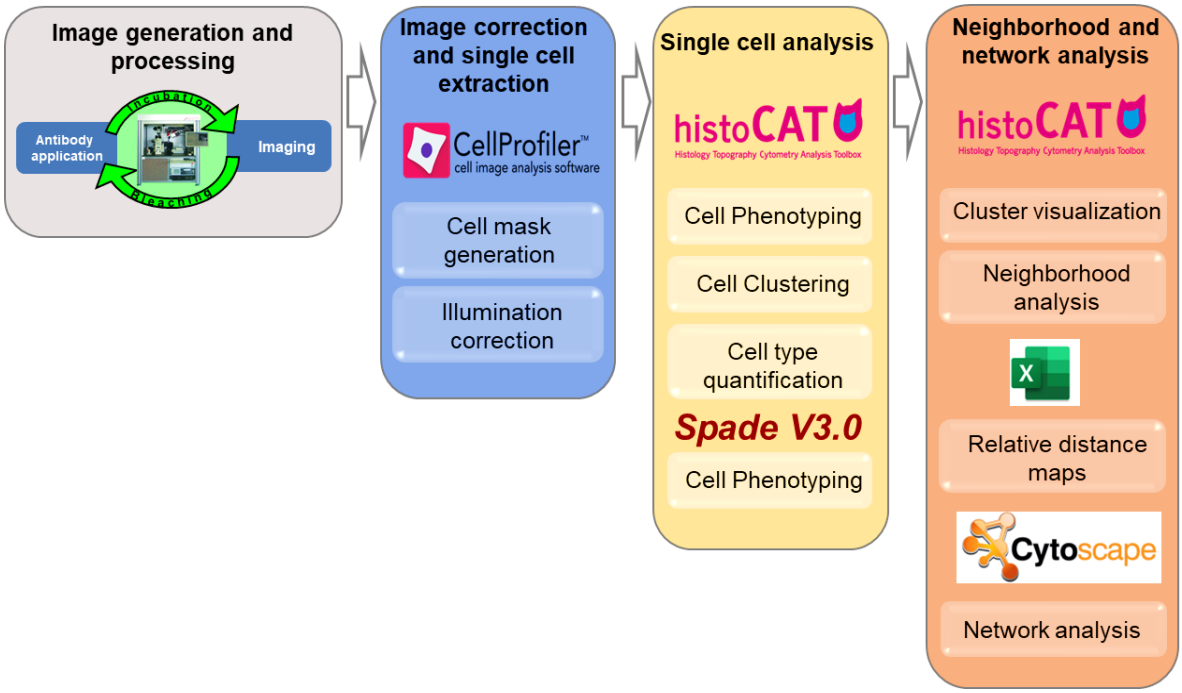

Figure 8: Overview of the main steps and the used programs of the bioinformatic analysis pipeline. High-dimensional image data was generated using the MELC technology. At first, the images were processed by the MELC software to remove background signals and autofluorescence and to align the images. In the next step, Cell Profiler was used for illumination correction and generating a cell mask to define single cells. The corrected images and the cell mask were used for single-cell analysis in HistoCAT and SPADE, including cell phenotyping, clustering, and cell type quantification. Based on the single-cell analysis results, neighborhood analysis and cluster visualization were performed in HistoCAT. The neighborhood analysis data generated relative distance maps in Microsoft Excel and cellular networks in Cytoscape.

The first step of the pipeline is illumination correction, which is essential to generate accurate and reliable data. Images with uneven illumination, acquisition artifacts, or vignetting can bias the downstream analysis[75]. CellProfiler offers two different methods for illumination correction: regular and background. The first function calculates the illumination function based on the intensity at each image pixel, which is an ideal solution for images with objects evenly dispersed over most of the image. As this was not the case for our paw tissue, we chose the background method for defining the minimum pixel intensities within defined blocks across image [76]. Using the MELC images without the illumination correction step caused missing objects in the cell mask and incorrect clustering of the immune cells in HistoCAT.

Single-cell mask generation was performed with Otsu's thresholding method using the "IdentifyPrimaryObjects" and "IdentifySecondaryObjects" modules in CellProfiler. In this case, an object is a generic term for an identified feature in an image, usually a cellular sub-compartment. Ideal primary objects are stained nuclei of the cells as they have a uniform morphology and can distinguish without the assistance of another cellular feature as a reference [77]. In our case, we used the marker propidium iodide to define the number of objects covered by the cell mask. The pan cell surface marker CD45 was used as a secondary object determining the cell borders to define the size of the objects in our cell mask. To get an accurate cell mask, it is essential to use makers as primary and secondary objects expressed in every sample cell. That can be a problem with the marker used for the cell membrane and the secondary object module in some tissues. Therefore, cell mask generation was also tested using only primary objects based on the nuclei marker and defining the size of the detected objects manually using the ExpandOrShrinkObjects module in CellProfiler. This strategy was successfully employed on the post-stroke brain tissue. As this method needs a careful adjustment of the correct object size, it is unsuitable for a high number of different datasets or samples with a great variety of object sizes. Additional cytoskeleton staining with phalloidin or actin should be tested for such tissues. The segmentation of the images with the CellProfiler modules is based on different intensities of background and foreground. If the differences in the intensity between these two are too low for an adequate segmentation, a program called

Ilastik[78], a supervised machine learning approach, could be used in combination with CellProfiler to perform a pixel-based classification. To further enhance the object detection quality for the cell mask, deep learning algorithms like DeepCell[79] or U-net[80] can be used. As the training of these algorithms needs a great variety of high-quality training data and careful manual annotation, we did not use them during this project. Their establishment is only worthwhile for big datasets.

After image correction and cell mask generation, the single cells were analyzed with HistoCAT and SPADE.

The first mentioned is an analysis toolbox, which enables interactive, quantitative, and comprehensive exploration of individual cell phenotypes, cell-cell interactions, microenvironments, and morphological structures within intact tissues[74]. Using the implemented PhenoGraph algorithm, cells were sorted into phenotype clusters based on their marker expression. The number of clusters was predicted automatically based on the input of the variable k value. This factor determines the number of clustered neighbors based on proximity. A small k value results in more clusters than bigger values based on grouping fewer cells with higher proximity into the same cluster. Finding the correct k value for every sample type is crucial for the correct interpretation of the data. It requires experience with this algorithm and knowledge about the histology of the used tissue to prevent over-clustering or under-clustering. The first can lead to the merging of similar clusters and cause rare populations' complete disappearance. Over-clustering duplicates clusters with similar expression patterns letting single immune cell populations appear to be overrepresented.

The interpretation of final clusters displayed as colored heatmap must be handled with great care and documented detailed as it might lead to different ways of interpretation in some cases. It is essential to notice that the strength of the marker expression in a single cluster is relative compared to the other clusters visible in the same heatmap and can not be equated with data from a different PhenoGraph analysis. To minimize false results, the clusters should constantly be reviewed in context with their positioning in the tissue available in HistoCAT and the underlying

image data. Sometimes it can be challenging to interpret similar colors correctly in the heatmap. Displaying the marker intensities additional as values would be an advantage in this case. The PhenoGraph algorithm can resolve populations as rare as 1/2000 cells[81] and creates only a small number of clusters which is an excellent opportunity to discover immune cell populations in large data sets and sort the cells into main groups.
A different algorithm has to be used to uncover rarer populations or analyze tissues that contain only a small number of objects in the cell mask.

We implemented SPADE in our pipeline to detect the different phenotypes of the eosinophils in the inflamed paw and the neoangiogenesis in the stroke area. In contrast to HistoCAT, which integrates spatial information from tissue sections with high-dimensional single-cell data, allowing spatially-resolved analysis, SPADE creates a spanning-tree representation of the cell populations, providing a hierarchical view of cellular relationships. The program performs four computational modules. First, a density-dependent down-sampling is performed to equalize the density in different cloud parts and achieve equal representation of rare and abundant cell types. Second, SPADE performs agglomerative clustering to partition the down-sampled cloud into clusters of cells with similar phenotypes which show similar marker intensities. Because of the down-sampling step, rare populations are separated into their own clusters and are not outnumbered, as happens during the clustering in HistoCAT with PhenoGraph. During the third and fourth steps, the program constructs a spanning tree to link the cell clusters and does an up-sampling to map all the cells onto the resulting tree structure[82].
In contrast to the PhenoGraph algorithm, the user must manually define the number of desired clusters and determine the clustering process's stopping criterion and the number of nodes in the SPADE tree. As the k value in HistoCAT, the cluster number must be chosen carefully for every experiment and depend on the complexity of the sample and the expected number of subpopulations in the data.
Also, the choice of markers used for the SPADE tree generation and the interpretation of the biological relevance of the results make prior knowledge of the

tissue necessary. Because of the different underlying methodology, SPADE produces a much higher number of clusters than the PhenoGraph in HistoCAT, making it more complex and time-consuming to interpret the results. Therefore, it is advisable to use SPADE focusing on single previously defined populations.

For the investigation of the neighborhoods of the clusters, we used HistoCAT again. The provided neighborhood analysis uses an iterative permutation approach, yielding a Boolean score to determine the position of a PhenoGraph cluster concerning the other clusters. This method allows a relative perspective on the positioning of the clusters, making samples with different similarities and appearances more comparable to a physical distance measurement. The scores could display the cellular networks in the analyzed tissue with Cytoscape. Nevertheless, it is necessary to include an additional method for distance measurement in the pipeline to get additional information about cell frequencies within a defined distance to analyze specific microenvironments further.

The main disadvantage of our developed pipeline is the necessary data transfer between the different programs, which is time-consuming and must be done carefully regarding the required file format for the next pipeline step. A solution for this problem would be recreating the algorithms used in a programming environment like R or Python. Recent developments like the Steinbock framework[83] or cytomapper[84] cover only parts of the pipeline and require programming skills but might be an option later as they are still under development.

5.2 Inflammatory architecture based on macrophage subtypes

To investigate a TLR-2 induced inflammation, the pathogen zymosan was injected into the hind paw of mice. The inflamed tissue was analyzed at different time points after the zymosan injection, with MELC and the established bioinformatical pipeline, to investigate the microenvironments and the inflammatory architecture. With this method, an inflammatory structure based on three major regions could be identified. The structure is based on the different macrophage subtypes and their cellular neighborhoods. The region containing the pathogen zymosan is called the core region and is dominated by neutrophils and some M1-like macrophages. This region is surrounded by a pro-inflammatory PI- region based on the distribution of the M1-like macrophages. M2-like macrophages characterize an outer anti-inflammatory region called the AI- region. The formation of the pro-inflammatory region starts 8 hours after the pathogen injection with the polarization of the M1-like macrophages and is completely established after the polarization of the M2-like macrophages 24 hours after zymosan-injection.

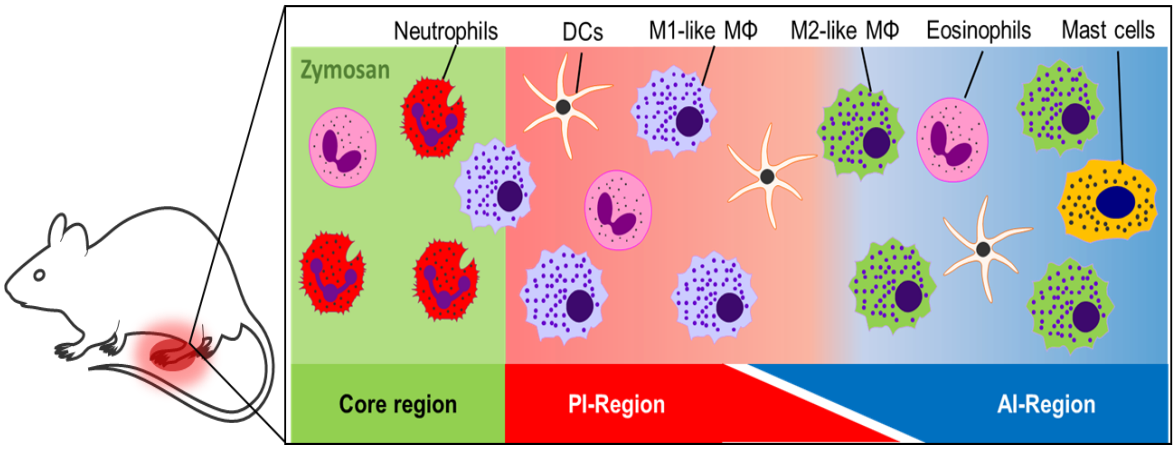

Figure 9: Spatial organization of immune cells during an innate inflammation. A TLR-2 mediated inflammation was induced in the hind paw of mice with zymosan injection. The immune cells formed a specific inflammatory structure with three separable regions containing either a pro-or an anti-inflammatory microenvironment.

The general understanding is that an acute inflammatory response consists of pro-inflammatory initiation and anti-inflammatory resolution phases. Both parts are time-dependent and take place one after another[10,85]. Our results show that pro-and anti-inflammatory processes coincide in different parts of the inflamed tissue. A temporal transition is only reflected in a change in the ratio and the size of the two regions. The size of the two regions in MELC data followed the amount of M1- and M2-like macrophages in the FACS analysis of the whole paw. The balance between these regions is defined by the amount of pro- and anti-inflammatory mediators generated by immune cells in these regions, which leads to a flexible expansion or shrinking of one region.

One important starting point for the formation of the anti-inflammatory region in our model might be the apoptosis of the neutrophils. This process can be induced by the expression of death ligands as TRAIL or FasL produced by macrophages[86,87] and is after the cessation of neutrophil influx, the second known key factor for the start of the resolution phase[85]. Efferocytosis of the neutrophils induces a metabolic switch in macrophages, leading to a repolarization from M1-like macrophages towards the M2-like phenotype and the release of anti-inflammatory mediators[88]. These changes in the macrophage phenotype are considered the third critical factor for the induction of the resolution. If these three key factors do not occur or are reduced due to dysfunctional pro-inflammatory mechanisms, the resolution phase is disrupted or delayed, as we could observe after the eosinophil depletion. Consequently, the transition from inflammation to tissue repair is impaired, and chronic inflammation may ensue. Therefore, maintaining intact pro-inflammatory processes is vital for ensuring a smooth and effective resolution of inflammation and preventing the establishment of chronic inflammatory conditions[17,85,89].

After the inflammatory structure is established, newly recruited immune cells adapt their phenotype to the region they arrive in and reinforce this region's character[90]. The microenvironment initiates cell type-specific responses such as the release of cytotoxic compounds, phagocytosis, or a further release of proinflammatory

mediators or influences the phenotype of the immune cells, for example, macrophages or eosinophils.

Zymosan was chosen as a pathogen for the project because of its particular structure. This structure leads to remaining zymosan at the injection site until it is phagocytosed, which was necessary for the observation with the MELC. The inflammatory structure could form around zymosan and maintain the same part of the tissue for the whole course of inflammation. Models for innate inflammation caused by mobile pathogens are expected to have the same structure. Still, they will have a more diffuse appearance since the pathogens will form separated core regions with overlapping PI and AI regions. Also, inflammation models, including the adaptive immune system, might show another inflammatory structure. Studying and comparing the inflammatory structure in different inflammation models may provide the possibility to predict the role of an immune cell and its interaction with other cells based on their positioning in the architecture, which could give new insights into therapeutic approaches and consequences for immunosuppressants.

5.3 Role of eosinophils during zymosan-induced inflammation

In the zymosan-induced inflammation model, eosinophils belong together with neutrophils to the first immune cells, which could be observed in the inflamed tissue after pathogen injection, which is in line with previous reports about the initiation of an innate immune response[91,92]. In our proposed inflammatory architecture, eosinophils are located in all three regions, which makes them an exciting cell type regarding their role in developing the structure and the influence of the structure on their phenotype.

I found that eosinophils adapted their phenotype to the different microenvironments leading to a different cytokine expression. This microenvironment influence on the phenotype of the immune cells is best understood in the case of macrophages. These exhibit reversible phenotypic states between pro-inflammatory M1-like and

anti-inflammatory M2-like macrophages. Changes in the microenvironment of these cells induce corresponding transcriptional reprogramming.[93,94] The observed environment-induced changes in the phenotype of eosinophils are in line with previous reports.

It has been shown that eosinophils can polarize towards so-called Type 1 or Type 2 phenotypes in response to different conditions, which could be found during Type 1 or Type 2 inflammatory responses. The two eosinophil types differed in their transcriptional profiles, surface markers, and release mediators.[95] Contrary environment-specific subtypes of eosinophils have been described in synovium and lung cases. A pro-inflammatory eosinophil subset could be identified in the latter, while the synovium showed a pro-resolving phenotype of the eosinophils[96]. Besides macrophages and eosinophils, other immune cell types might also express different phenotypes depending on their surrounding microenvironment. In the case of this project, I expect this for DCs, as they were located in all regions of our inflammatory structure, like the eosinophils. Because of missing markers, we could not detect and characterize these different phenotypes yet.

Eosinophils produce and release toxic granule proteins like eosinophil peroxidase (EPO), eosinophil cationic protein (ECP), eosinophil-derived neurotoxin (EDN), and major basic protein (MBP) and synthesize nitric oxide[97]. Due to the release of these substances and the production of leukotrienes, which have direct or indirect vasodilatory effects, eosinophils contribute to edema formation in skin diseases[98,99]. Our model instead found a predominantly anti-inflammatory role of the eosinophils in the course of inflammation. After the depletion of the eosinophils with an anti-Siglec F antibody, the onset or maximal size of the edema was not altered. In contrast, the size of the edema during the resolution was increased. Additionally, mechanical and thermal zymosan-induced hypersensitivity resolution was delayed after depleting the eosinophils without affecting the onset or the maximal behavioral response. Taking in account that the amount of cytotoxic substances released by eosinophils is much less compared with neutrophils and the high amount of neutrophils in our inflamed tissue, the importance of the eosinophils during the

edema formation might be to vague to see an effect after the depletion in our model. Instead neutropils seem to be the key player for the edema formation as demonstrated in other publications[100,101].

The only inflammatory mediator that was downregulated after Eosinophil depletion was IL-4. This finding follows a previous report showing decreased levels of IL-4 after Eosinophil depletion with anti-Siglec F antibody in mice[102]. Different cell types can produce this interleukin, for example, CD4 positive T-cells, basophils, eosinophils, mast cells, NK T-cells, and ILC2 cells[103]. During allergic inflammation and murine asthma in mice, eosinophils and T-helper cells were discovered to be the primary source of pulmonary IL-4 production and promote a Type 2 immune response[104,105]. Eosinophils were also the leading producer of IL-4 in inflammatory dilated cardiomyopathy[106] and during the innate phase of *Leishmania major* infection[107].

On the cellular level, Eosinophil depletion reduced the amount of anti-inflammatory M2-like macrophages, reduced the efferocytosis capacity of macrophages, and increased the number of free neutrophils. Consequently, a breakdown of the border between PI and AI region occurred. Administration of IL-4 restored the inflammatory architecture and normalized the number of M2-like macrophages neutrophils and the efferocytosis capacity of the macrophages during our project. These results are in line with the following previous publications.

The polarization of M2-like macrophages occurs in response to downstream signals of cytokines like IL-4, IL-13, IL-10, IL-33, and TGF- β, while only the first two directly induce M2-like polarization[19,108]. On myeloid cells, IL-4 acts through two receptors (IL-4Rs)[109] activating the signaling pathways STAT-6[110] and PI3K[111] and induces phosphorylation of p38 MAPK[112].

Other studies could also demonstrate that selective phagocytosis of neutrophils by macrophages could be increased through the treatment with IL-4[113]. This effect is caused by the increased expression and activity of the nuclear receptor PPARγ via STAT6[114] and the induced production of potential PPARγ-activating ligands, 13-

HODE, and 15-HETE through 15-lipoxygenase activity on the one hand[115]. On the other hand, IL-4 can increase the expression of the efferocytosis receptors stabilin-1 and stabilin-2[116,117].

In the case of the neutrophils, it was demonstrated that IL-4 and IL-13 stop their migration and tissue infiltration, influence their chemotaxis, inhibit the formation of extracellular traps, and antagonize the effects of granulocyte colony-stimulating factors[118,119]. In the bone marrow, increased IL-4 concentration during infection resulted in decreased G-CSF (granulocyte colony-stimulating factor)-mediated egress and increased retention of neutrophils[120] through the activation of STAT6 and p38 MAPK, which led to an upregulation of CXCR4 as well as a downregulation of CXCR2. The G-CSF induces the egress from the bone marrow by weakening CXCR4-mediated retention signals and augmenting the neutrophils' sensitivity toward CXCR2-binding chemokines[121]. Mice lacking IL-4 and IL-13 showed increased neutrophil recruitment to the liver after infection with *Schistosoma japonicum*[119]*.* Animals sensitized with house dust mite extract showed increased lung neutrophil counts after treatment with a neutralizing anti-IL-4 antibody[122].

5.4 Conclusion

Inflammation is a complex physiological process involving various immune cells and molecular mediators. The failure of the inflammatory response can lead to persistent inflammation and the development of autoimmune diseases. To uncover the reasons for a failure understanding the mechanisms driving the formation, maintenance, and interaction of inflammatory microenvironment is essential. The observed inflammatory architecture based on three regions presented in this thesis demonstrates that pro-inflammatory and anti-inflammatory processes coexist in distinct areas of inflamed tissues. The balance between these regions is modulated by immune cell-generated pro- and anti-inflammatory mediators, allowing each region's flexible expansion or contraction. Immune cells respond to signals from the microenvironment by releasing mediators, exhibiting cytotoxic effects, performing phagocytosis, or undergoing polarization. Previous studies have proposed a temporal transition during inflammation, where pro-inflammatory processes dominate initially, followed by a shift towards anti-inflammatory resolution mechanisms. The current findings challenge the concept of a gradual temporal transition from pro- to anti-inflammation, suggesting that the temporal transition is characterized by changes in the ratio of the sizes of pro- and anti-inflammatory regions rather than a linear progression from one state to another. The balance between these regions is not simply a sequential shift but a flexible and complex interplay influenced by immune cell interactions and the local microenvironment. The observed coexistence of these regions implies that pro-inflammatory and anti-inflammatory mechanisms are concurrently active, likely contributing to the overall inflammatory response and its regulation. Refining our understanding of the spatiotemporal dynamics of pro- and anti-inflammatory processes will contribute to developing more precise therapeutic strategies. Targeting and modulating specific immune cell populations or their interactions within the inflammatory microenvironment may restore a balanced and controlled immune response, ultimately leading to improved treatment outcomes for inflammatory diseases and autoimmune conditions. While the observed architecture may provide predictive

value in determining the role of immune cells based on their localization within the inflammatory setting, it is crucial to consider the existence of diverse immune cell subtypes/phenotypes with distinct and, at times, opposing functions. Eosinophils, for instance, were found to be present in all three inflammatory regions but displayed altered cytokine expression depending on their surroundings. The breakdown of the inflammatory structure after Eosinophil-depletion proves the important role of single immune cell types in maintaining the microenvironment and the complex interaction between cells of the same or a different immune cell type. The focus of this study was the investigation of the innate immune response. Different animal models, like the ovalbumin model, offer the possibility of studying the function of the adaptive immune system. Following sensitization with ovalbumin, the mice undergo repeated challenges with this protein, which leads to the activation of antigen-presenting cells, primarily DCs, and specific T cells' activation and proliferation. Investigating the inflammatory architecture and the different microenvironments in different inflammation models will enhance the possible treatments for chronic and allergic diseases and asthma.

6. Publications

6.1 List of publications

1) Kolbinger A, Schäufele TJ, Steigerwald H, Friedel J, Pierre S, Geisslinger G, Scholich K. **Eosinophil-derived IL-4 is necessary to establish the inflammatory structure in innate inflammation.** *EMBO Molecular Medicine.* 2023;15(2):e16796. doi:10.15252/emmm.202216796
2) Kolbinger A, Kestner RI, Jencio L, Schäufele TJ, Vutukuri R, Pfeilschifter W, Scholich K. **Behind the Wall - Compartment-Specific Neovascularisation during Post-Stroke Recovery in Mice**. *Cells*. 2022;11(10):1659. doi:10.3390/cells11101659

As co-author (not included in this thesis)

1) Kornstädt L, Pierre S, Weigert A, Ebersberger S, Schäufele TJ, Kolbinger A, Schmid T, Cohnen J, Thomas D, Ferreirós N, Brüne B, Ebersberger I, Scholich K. **Bacterial and Fungal Toll-Like Receptor Activation Elicits Type I IFN Responses in Mast Cells.** *Front Immunol.* 2021;11. doi:10.3389/fimmu.2020.607048
2) Dorochow E, Kraus N, Chenaux-Repond N, Pierre S, Kolbinger A, Geisslinger G, Ortiz C, Welsch C, Trebicka J, Gurke R, Hahnefeld L, Klein S, Scholich K. **Differential lipidomics, metabolomics and immunological analysis of alcoholic and non-alcoholic steatohepatitis in mice.** *International Journal of Molecular Sciences.* Accepted
3) Schäufele TJ, Kolbinger A, Friedel J, Gurke R, Geisslinger G, Weigert A, Pierre S, Scholich K. **Meloxicam treatment disrupts the regional structure of innate inflammation sites by targeting the pro-inflammatory effects of prostanoids.** *British Journal of Pharmacology.* Under review

6.2 Publications

Article

SOURCE DATA | TRANSPARENT PROCESS | OPEN ACCESS

EMBO Molecular Medicine

Eosinophil-derived IL-4 is necessary to establish the inflammatory structure in innate inflammation

Anja Kolbinger[1], Tim J Schäufele[1], Hanna Steigerwald[1], Joschua Friedel[1], Sandra Pierre[1], Gerd Geisslinger[1,2,3] & Klaus Scholich[1,2,3,*]

Abstract

Pathogen-induced inflammation comprises pro- and anti-inflammatory processes, which ensure pathogen removal and containment of the proinflammatory activities. Here, we aimed to identify the development of inflammatory microenvironments and their maintenance throughout the course of a toll-like receptor 2-mediated paw inflammation. Within 24 h after pathogen-injection, the immune cells were organized in three zones, which comprised a pathogen-containing "core-region", a bordering proinflammatory (PI)-region and an outer anti-inflammatory (AI)-region. Eosinophils were present in all three inflammatory regions and adapted their cytokine profile according to their localization. Eosinophil depletion reduced IL-4 levels and increased edema formation as well as mechanical and thermal hypersensitivities during resolution of inflammation. Also, in the absence of eosinophils PI- and AI-regions could not be determined anymore, neutrophil numbers increased, and efferocytosis as well as M2-macrophage polarization were reduced. IL-4 administration restored in eosinophil-depleted mice PI- and AI-regions, normalized neutrophil numbers, efferocytosis, M2-macrophage polarization as well as resolution of zymosan-induced hypersensitivity. In conclusion, IL-4-expressing eosinophils support the resolution of inflammation by enabling the development of an anti-inflammatory framework, which encloses proinflammatory regions.

Keywords eosinophil; innate inflammation; interleukin-4; macrophages; microenvironments

Subject Category Immunology

DOI 10.15252/emmm.202216796 | Received 25 August 2022 | Revised 6 December 2022 | Accepted 8 December 2022 | Published online 21 December 2022

EMBO Mol Med (2023) 15: e16796

Introduction

Pathogen-induced inflammation involves pro- and anti-inflammatory processes to ensure pathogen removal as well as containment and resolution of the proinflammatory activities. After tissue intrusion by pathogens, a complex innate immune response is triggered by local cells following the recognition by toll-like receptors (TLR), which initiate the recruitment of local and blood-derived innate immune cells. Neutrophilic and eosinophilic granulocytes are among the first cell types recruited to the tissue followed, with some delay, by monocytes and dendritic cells (DC) (Kolaczkowska & Kubes, 2013; Lastrucci *et al*, 2015). Once having crossed the endothelium and entered the inflamed tissue the immune cells react according to the signals they receive from their microenvironment and initiate cell type-specific responses such as the release of cytotoxic compounds, phagocytosis or a further release of proinflammatory mediators. The entity of all cells interacting with an immune cell are forming its microenvironment.

The best understood example for the influence of microenvironments on immune cells is the polarization of macrophages toward proinflammatory M1-like or anti-inflammatory M2-like phenotypes depending on their microenvironment (Imhof & Aurrand-Lions, 2004; Shi & Pamer, 2011). Macrophages exhibit various reversible phenotypic states within the M1/M2 spectrum whereby changes in the microenvironment induce a corresponding transcriptional reprogramming (Murray & Wynn, 2011; Okabe & Medzhitov, 2014). As a consequence, the specific positioning of macrophages within the inflamed tissue decides their polarization fate as demonstrated by the fatty acid/lactate receptor G2A (GPR132), which indirectly regulates macrophage polarization towards proinflammatory M1-like phenotypes by positioning the macrophages in a proinflammatory microenvironment (Kern *et al*, 2018). Similar environment-induced changes might also occur in other cells types. For example, eosinophils have various pro- and anti-inflammatory mediators, which can be rapidly released from specific granules and lipid bodies according to the situation (Weller & Spencer, 2017; Rigoni *et al*, 2018). However, tissue-specific subsets of pro-resolution eosinophils in the synovium and proinflammatory eosinophils in lungs have been described (Andreev *et al*, 2020). Moreover, it was shown that eosinophils can polarize toward distinct Type 1 or Type 2 inflammatory response phenotypes (Dolitzky *et al*, 2021).

To better comprehend the interaction between cellular microenvironments and immune cells during an ongoing inflammation, it is crucial to understand how these cellular microenvironments are

1 Institute of Clinical Pharmacology, Goethe-University Frankfurt, Frankfurt, Germany
2 Fraunhofer Institute for Translational Medicine and Pharmacology ITMP, Frankfurt, Germany
3 Fraunhofer Cluster of Excellence for Immune-Mediated Diseases CIMD, Frankfurt, Germany
*Corresponding author. Tel: +49 69 6301 83103; Fax: +49 69 6301 83103; E-mail: scholich@em.uni-frankfurt.de

formed and maintained. Important information about the microenvironment of immune cells are normally rudimentary due to the limited numbers of markers, which can be visualized by classical immunohistochemical approaches. Therefore several methods have been developed in the last years to visualize dozens of cellular marker on the same tissue, allowing investigation of formation and regulation of cellular networks under physiological or pathophysiological conditions (Hoch *et al*, 2022; Moldoveanu *et al*, 2022). Here, we used the multiepitope-ligand-carthography (MELC) technology for multiple sequential immunohistochemistry to visualize 40 antibodies on the same tissue (Schubert *et al*, 2006; Friedenberger *et al*, 2007). Established bioinformatics approaches (Schapiro *et al*, 2017; Kornstädt *et al*, 2020; Kolbinger *et al*, 2022) were applied to analyze the formation of the basic inflammatory structure based on the immune cell distribution. Using eosinophils as an example, we determined the impact of distinct microenvironments on immune cells and investigated the role of a specific immune cell type, using eosinophils as example, on the formation of microenvironments.

Results

Macrophages define distinct subregions of a local zymosan-induced inflammation

Zymosan-induced paw inflammation is a common model to study TLR-2-mediated innate immune responses. It is especially suited to investigate the distribution of immune cells in relation to the pathogen, since the particulate structure of zymosan immobilizes it at the site of injection and usage of FITC-labeled zymosan allows to determine its exact localization in the tissue (Pierre *et al*, 2017; Kern *et al*, 2018). To detect immune cells, the MELC technology (Schubert *et al*, 2006; Schuh *et al*, 2014) was used, 40 antibodies were used to identify and localize immune and nonimmune cells in the tissue (Appendix Table S1). The field of visions (600 × 600 µm) were chosen to cover a part of the zymosan-containing region together with its adjacent areas, whereby the zymosan covered area represented around 30% of the field of visions. For quantitative assessment of cells, a segmentation mask was generated based on the staining for CD45 and nuclei (Propidiumiodide), which was then used to extract single-cell expression data from images of all measured markers (Fig EV1). Single-cell phenotyping was performed using PhenoGraph analysis and was followed by the identification of cell clusters representing the different immune cell types. It should be noted that for better clarity only the markers are explicitly mentioned in the text, which were used to define a specific cell type.

In the first step, we used this bioinformatic pipeline to track macrophage polarization over the course of the zymosan-induced inflammation. We found that within and adjacent to the zymosan-containing area 8 h after zymosan injection cell clusters representing macrophages started to diverge from an undifferentiated phenotype (M0 macrophages, defined by expression of Siglec F^-/F4-80^+/$CD86^+$/$CD206^-$) to M1-like macrophages (Siglec F^-/F4-80^+/$CD86^+$/$CD206^-$) and after 24 h also to M2-like phenotypes (Siglec F^-/F4-80^+/$CD86^-$/$CD206^+$; Fig 1A–D; Appendix Fig S1). Markers for dendritic cells such as CD11c and MHC II were absent in clusters considered as representing macrophages. The time course of macrophage polarization seen in MELC analyses was confirmed by FACS analysis of the paw tissue demonstrating that the macrophage populations in the observed areas are representative for the macrophages in the inflamed paw (Fig 1E–H). Macrophage specific expression of CD86 and CD206 was ensured by applying the gating strategy shown in Appendix Fig S3. The immunohistochemical staining suggested that starting at 24 h after zymosan injection M1-like macrophages were located within the zymosan-containing area or in its close proximity, whereas M2-like macrophages were localized in greater distance to zymosan (Fig 1A). To quantify this observation a bioinformatic assessment of the relative distance of zymosan to clusters representing M1- and M2-like macrophages was performed using a neighborhood analysis. Here, the likelihood of cells neighboring each other is determined in comparison to a randomized version of the same tissue (Schapiro *et al*, 2017). The analysis confirmed a spatial pattern with a direct neighborhood of M1-like macrophages to zymosan, while M2-like macrophages were excluded as direct neighbors of zymosan (Fig 1I; Appendix Fig S3).

To determine which immune cells were localized in the inflamed tissue, cell clusters representing immune cells were quantified 24 h after zymosan injection. The most abundant immune cell clusters were macrophages (defined by $CD45^+$/$Ly6C^{-/+}$/F4-80^+/$CD11b^+$), neutrophils ($CD45^+$/$Ly6G^+$), eosinophils ($CD45^+$/Siglec F^+/F4-80^+), DCs ($CD45^+$/F4-80^-/$CD11c^+$) and mast cells ($CD117^+$/cytokeratin$^-$) (Fig 2A). Clusters representing B-cells ($CD45^+$/$CD19^+$ or $CD22^+$), T-cells ($CD45^+$/$CD3^+$/$CD4^{-/+}$/$CD8^{-/+}$), NK- and NK-like cells ($CD45^+$/$CD3^{-/+}$/$NK1.1^{-/+}$), and ILCs ($CD45^+$/$CD3^-$/$GATA3^{-/+}$/T-$Bet^{-/+}$/$ROR\gamma T^{-/+}$) were not found in the observed areas of the inflamed tissue (Fig 2A). Next, we created a linear map of the immune cell distribution using either zymosan or M2-like macrophages as reference points, since they represent the contrasting pro- and anti-inflammatory extremes. Direct neighbors of zymosan were cell clusters representing M1-like macrophages (defined by F4-80^+/$CD86^+$/$CD206^-$), neutrophils ($Ly6G^+$/F4 80^-), DCs ($CD11c^+$/MHC II^+/$CD86^+$), and eosinophils ($Ly6C^+$/F4-80^+/$SiglecF^+$) (Fig 2B). In the

Figure 1. M1- and M2-like macrophages arrange at distinct distances around zymosan.

A Representative MELC images showing the distribution of macrophage polarization markers at the indicated time points after injection of FITC-labeled zymosan (3 mg/ml, 10 µl) in one hind paw. White dotted lines show the position of zymosan. Size bar represents 100 µm.

B–D Quantification of the number of macrophages and their subtypes 8, 24, 48, and 72 h after zymosan injection based on the MELC images. Data are shown as mean ($n = 5$ mice) ± SEM, one-way ANOVA/Bonferroni $^*P < 0.05$, $^{***}P < 0.001$. $^{\#}P < 0.05$, $^{\#\#\#}P < 0.001$ as compared to naïve mice.

E–H FACS analysis of macrophages and their subtypes 8, 24 and 48 h after zymosan injection. Data are shown as mean ($n = 8$ mice) ± SEM, one-way ANOVA/Bonferroni $^{**}P < 0.01$, $^{***}P < 0.001$.

I Relative distances from the zymosan-containing area based on the probability for an immediate neighborhood of macrophage subtypes at the indicated time points after zymosan injection. Data are shown as mean ($n = 5$ mice) ± SEM.

Source data are available online for this figure.

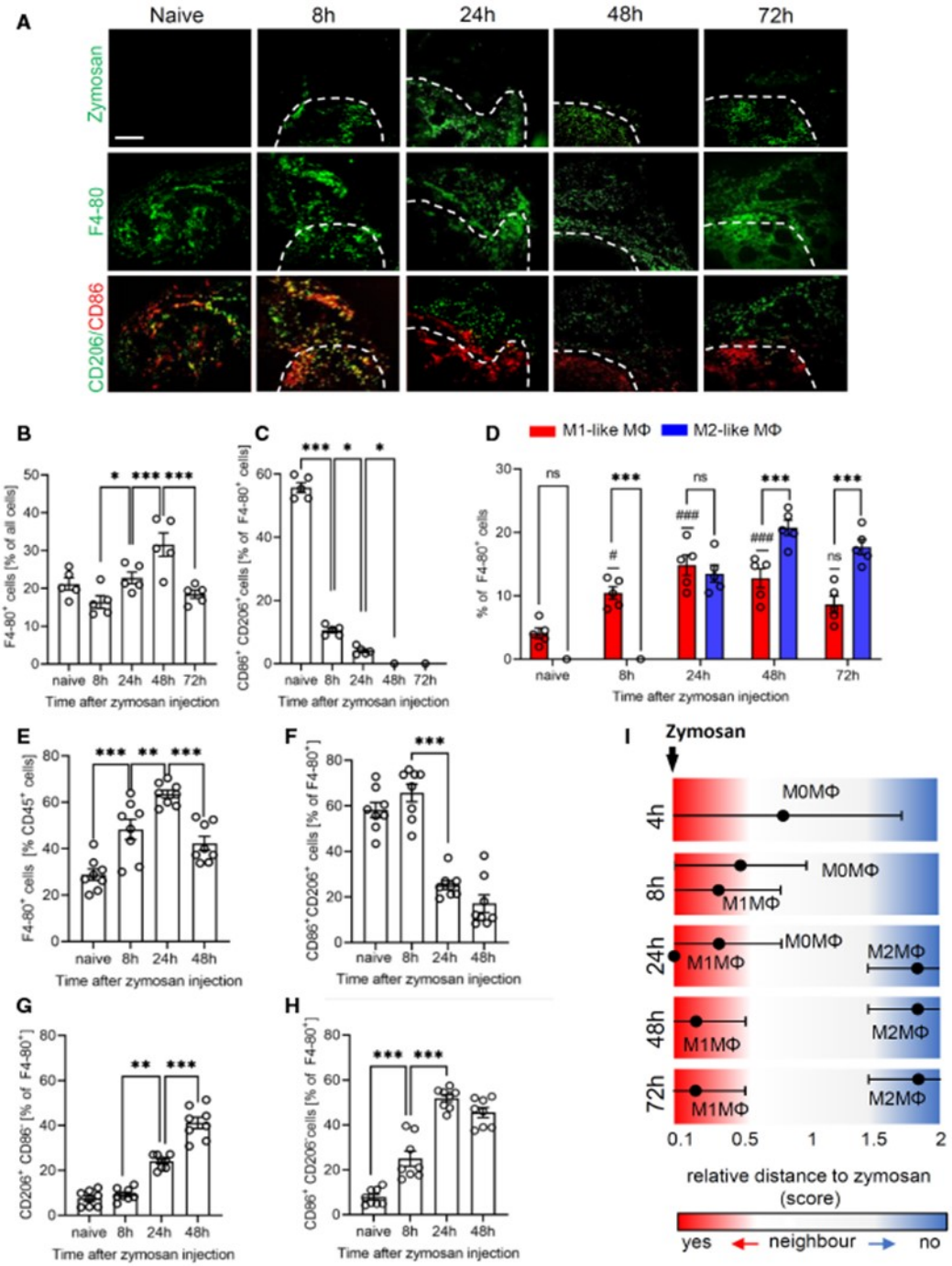

Figure 1

direct neighborhood of M2-like macrophages were, in accordance to a recent report, mast cells ($CD117^+$) (Kornstädt *et al*, 2020) as well as M1-like macrophages, DCs, and eosinophils (Fig 2C). The scores received by the neighborhood analysis were plotted to visualize the data as a combined dual-centered network based on zymosan and M2-like macrophages (Fig 2D). The network analyses in combination with the visualization of the major immune cell clusters in the tissue (Fig 2E) marked a proinflammatory "core-region" defined by the presence of zymosan. The core-region is bordered by a proinflammatory region (PI) comprising the area containing M1-like macrophages outside the core region. The PI-region is then adjoined by an anti-inflammatory region (AI), which is defined as the M2-like macrophage-containing area (Fig 2E). Neutrophils were mainly found in the core region and to a lesser degree in the PI region. Mast cells, as direct neighbors of M2-like macrophages, were localized in the AI-region. DCs and eosinophils were evenly distributed throughout the three inflammatory regions (Fig 2E, Appendix Fig S4A,B). Notably, the inflammatory architecture, consisting of core-, PI and AI-regions, was also observed at later time points during the inflammation demonstrating that this structure provides a stable framework for the inflammatory response until the pathogen is removed (Fig EV2).

Expression of IL-4 in eosinophils depends on their localization

Since cell clusters representing eosinophils and DCs were found in all three inflammatory regions, we determined whether region-dependent subtypes can be identified 24 h after zymosan injection, the time point when inflammatory regions and macrophage polarization were established. SPADE cluster analysis did not reveal distinct major DC subtypes based on the antibodies used (Appendix Fig S4C). In contrast, 4 h after zymosan injection only one major eosinophil population was seen (Fig 3A) while after 24 h two discrete major eosinophil subpopulations appeared (Fig 3B). Four hours after zymosan injection eosinophils expressed IL-4, IL-6, IL-13, and IL-10 while after 24 h eosinophils expressed either IL-4 and IL-13 or IL-6 and IL-10. Accordingly, IL-4-expressing eosinophils were evenly distributed throughout the monitored area including the core region 4 h after zymosan injection (Fig 3C) whereas after 24 h the IL-4-positive eosinophil subpopulation was not found in the core-region (Fig 3D). Since in early inflammation (4 h), all eosinophils express IL-4, the downregulation of IL-4 expression within the core region is likely an adaption to this microenvironment. Quantification of the percent of IL-4-expressing eosinophils 4 h after zymosan injection showed approximately 20% more IL-4 expressing eosinophils outside the core region (Fig 3E). Twenty-four hours after zymosan injection no IL-4 expressing eosinophils were detected in the core region, while in the AI region and the PI region, the percentage of IL-4-expressing cells increased to 25 and 60%, respectively (Fig 3F). Notably, eosinophil numbers in the paw were initially high and declined after 8 h (Fig 3G) suggesting that the recruitment of eosinophils slows or stops after 8 h and that the remaining eosinophils adapt to their specific microenvironment by downregulation of IL-4 expression.

Eosinophil depletion disrupts the inflammatory structure and resolution of inflammation

Next, we depleted eosinophils using anti-Siglec F antibodies following established protocols (Zimmermann *et al*, 2008; Driss *et al*, 2016; Wang *et al*, 2021). Compared to the isotype control the treatment with anti-Siglec F antibody reduced the number of eosinophils by around 90% in blood and inflamed paws (Fig 4A–C). Notably, the anti-Siglec F antibody used for depletion antibody did not interfere with binding of the detection antibody (Appendix Fig S5). Eosinophil depletion increased edema formation during its resolution phase without altering onset or maximal size of edema formation (Fig 4D). Also, the resolution of mechanical and thermal zymosan-induced hypersensitivity was delayed by eosinophil depletion without affecting the onset or the maximal behavioral response (Fig 4E and F) demonstrating that eosinophils fulfill predominantly anti-inflammatory functions in this inflammation model.

On the cellular-level eosinophil depletion caused a breakdown of the boundaries between the AI- and PI-regions, marked by an even distribution of M1- and M2-like macrophages around the core-region (Fig 5A). Fittingly, superimposition of the cellular networks of zymosan and M2-like macrophages showed in eosinophil-depleted mice a reduction of the relative distances for basically all observed immune cells toward a direct neighborhood (Fig 5B). Further analysis of the cell clusters derived from the MELC analysis showed a complete absence of eosinophils at the site of inflammation after anti-Siglec F treatment (Fig 5C), while the number of macrophages was not altered (Fig 5D). Importantly, M2-like macrophage numbers were significantly decreased in the observed areas (Fig 5E), whereas the number of M1-like macrophages was not changed (Fig 5F) and the number of M0-macrophages increased (Fig 5G). The altered macrophage polarization was accompanied by a decreased efferocytosis ($Ly6G^+/F4\text{-}80^+$; Fig 5H) and increased neutrophil numbers (Fig 5I). Taken together, the consequences of eosinophil depletion in regard to the decreased M2-like macrophage polarization support the *in vivo* data showing a predominantly anti-inflammatory effect of the eosinophils.

Figure 2. Based on immune cell distribution three inflammatory regions can be defined.

A Frequency of different immune cell types in the MELC images 24 h after zymosan injection. Data are shown as mean ($n = 5$ mice) ± SEM (n.d., not determinable).

B, C Relative distance of various immune cell types based on the likelihood for an direct neighborhood of macrophage subtypes in regard to zymosan (panel B) or M2-like macrophages (panel C).

D Network visualization using Cytoscape of the cellular neighborhoods of zymosan and M2-like macrophages. The distances between the cells in the visualization represents the statistical likelihood of being direct neighbors.

E Composite MELC images showing the position of the core-, the proinflammatory (PI) and the anti-inflammatory (AI) regions in the tissue in regard to the localization of M1- and M2-like macrophages (MΦ) and zymosan (left panel) or eosinophils, neutrophils and DCs (right panel). The red dotted lines depict the area where the transition between the neighboring regions occurs.

Source data are available online for this figure.

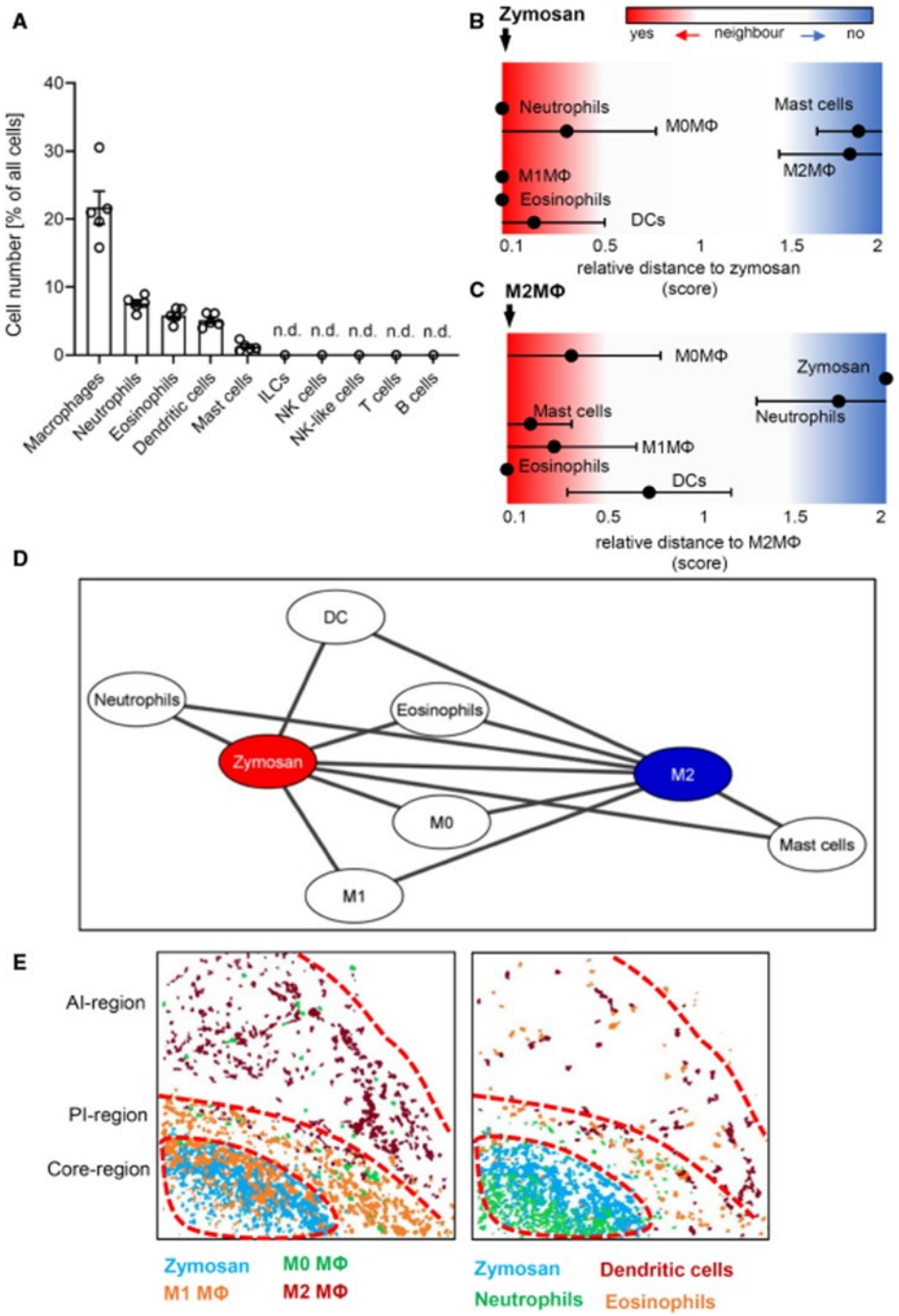

Figure 2.

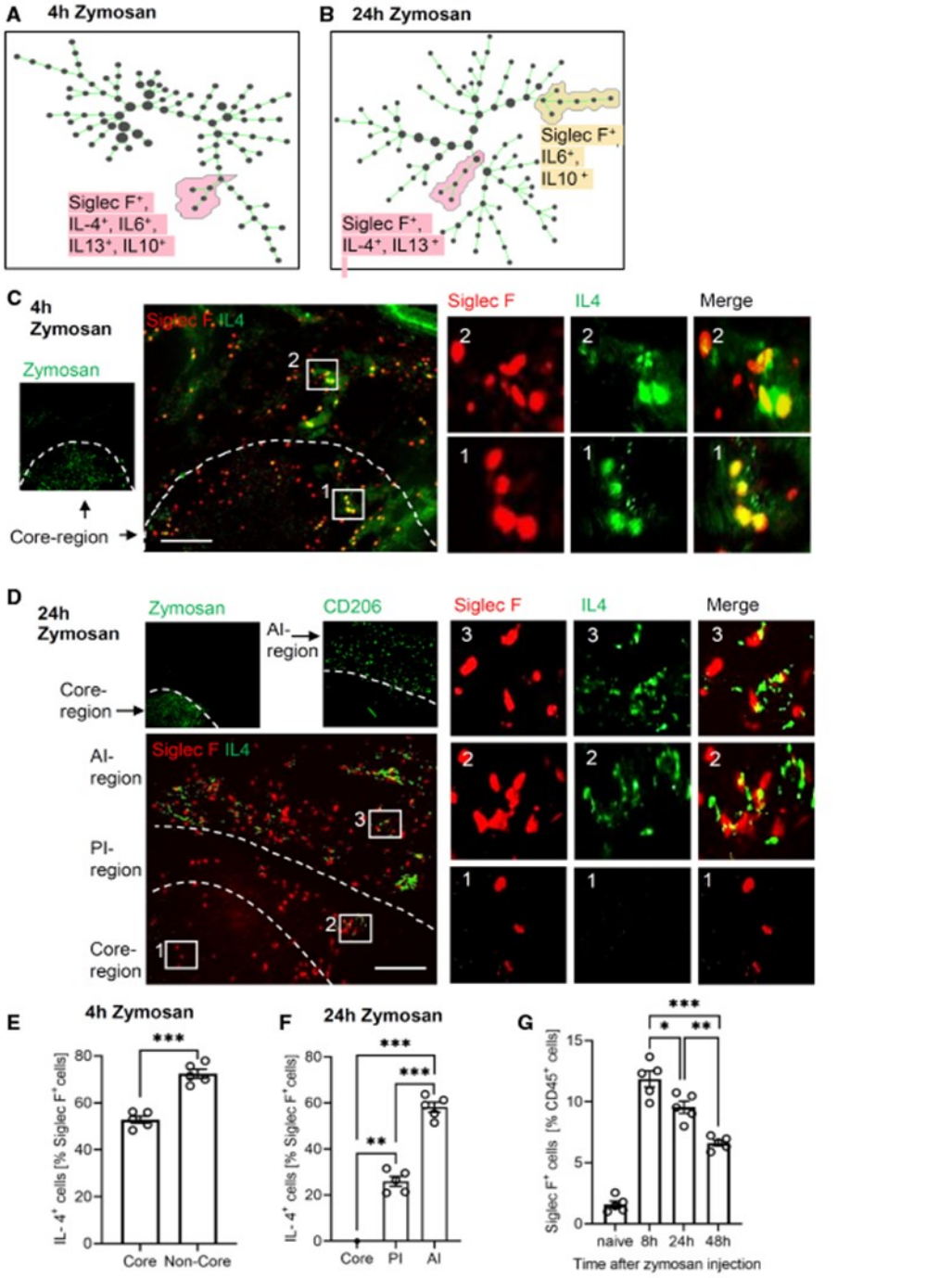

Figure 3.

Figure 3. Expression of IL-4 in eosinophils depends on their localization.

A, B Identification of eosinophil populations using SPADE analysis 4 (panel A) and 24 h (panel B) after zymosan injection.

C, D Representative MELC images showing the IL-4 and Siglec F expression 4 h (panel C) and 24 h (panel D) after zymosan injection. The white dotted lines depict the area where the transition between the neighboring regions occurs. Size bar represents 100 μm.

E Number of IL-4-expressing eosinophils in the core region and the surrounding area 4 h after zymosan injection. Data are shown as mean ($n = 5$ mice) ± SEM, two-tailed Students *t*-test ***$P < 0.001$.

F Number of IL-4-expressing eosinophils in the three regions 24 h after zymosan injection. Data are shown as mean ($n = 5$ mice) ± SEM, one-way ANOVA/Bonferroni **$P < 0.01$, ***$P < 0.001$.

G FACS analysis of the number of eosinophils at the indicated time points after zymosan injection in the inflamed paw. Data are shown as mean ($n = 5$ mice) ± SEM, one-way ANOVA/Bonferroni *$P < 0.05$, **$P < 0.01$, ***$P < 0.001$.

Source data are available online for this figure.

Eosinophil-derived IL-4 mediates macrophage polarization

Since IL-4-expressing eosinophils were cellular neighbors of M2-like macrophages, we hypothesized that eosinophil-derived IL-4 is necessary for correct polarization of M2-like macrophages. In support of this hypothesis, eosinophil depletion decreased the total IL-4 levels in the inflamed paws 8 and 24 h after zymosan injection (Fig 6A). To determine whether the altered resolution of inflammation induced by eosinophil depletion can be rescued by IL-4 application, we administered a stabilized form of IL-4 (IL-4c) (Finkelman *et al*, 1993; Milner *et al*, 2010; Jenkins *et al*, 2011). Administration of IL-4c did neither affect recruitment of eosinophils (Fig 6B) nor the number of resident ($Ly6C^-/CD45^+/F4\text{-}80^+$) or monocyte-derived macrophages ($Ly6C^+/CD45^+/F4\text{-}80^+$) (Fig 6C). However, eosinophil depletion and IL-4c administration altered macrophage polarization in several ways. First, as seen in the MELC analysis (Fig 5E), eosinophil depletion decreased the number of M2-like macrophages, which was rescued by IL-4c administration (Fig 6D). It should be noted that IL-4c administration to nondepleted mice induced a slight, but significant increase of macrophage polarization toward M2-like macrophages, which is in line with the known M2-like polarizing effect of IL-4 (Fig 6D). Second, the number of M1-like macrophages was not altered by eosinophil depletion, but decreased in mice receiving IL-4c (Fig 6E). This decrease could be expected, since IL-4 counters polarization towards M1-like phenotypes. Finally, the number of $CD86^+/CD206^+$ M0-macrophages was increased after eosinophil depletion (Fig 6F) reflecting the compromised M2-polarization due to decreased IL-4 levels. Administration of IL-4c to nondepleted mice increased the number of M0-macrophages to levels equal to eosinophil-depleted mice without further affecting their number in eosinophil-depleted mice (Fig 6F). Thus, eosinophil-depleted mice show a shift from M2-like macrophages toward M0 macrophages, while IL-4c-induced a shift from M1-like macrophages toward M0 and M2-like macrophages, thereby compensating the effects induced by eosinophil depletion.

Eosinophil-derived IL-4 mediates neutrophil recruitment and efferocytosis

Since MELC analyses shows an increased neutrophil recruitment in eosinophil-depleted mice (Fig 5I), we determined the levels of neutrophil-attractant mediators in inflamed paws of eosinophil-depleted mice. Screening of 26 chemokines, cytokines, and growth factors showed 9 mediators in the inflamed paw 24 h after zymosan injection. Eosinophil depletion significantly upregulated TNFα and the neutrophil-attractant chemokines CXCL1, CCL-2, CCL-3, CCL-4, CCL-5, and CCL-11 (Fig 7A), whereas IL-1α and IL-12 were not altered (Appendix Fig S6). FACS analysis confirmed the increased neutrophil numbers in eosinophil-depleted mice and showed that IL-4c application is able to reverse this increase of the number of neutrophils (Fig 7B). Notably, neutrophil levels were also increased in the blood of eosinophil-depleted mice, which normalized after IL-4c administration (Fig 7C). This is in accordance with a previous report showing that IL-4 suppresses neutrophil egress from the bone marrow (Panda *et al*, 2020). Eosinophil depletion was sufficient to increase neutrophil numbers also in the blood of mice without inflammation suggesting that eosinophils contribute to the IL-4-mediated homeostasis of neutrophil egress (Appendix Fig S7). Next, as predicted by the MELC analyses (Fig 5H), FACS analyses showed a reduced efferocytosis in eosinophil-depleted mice, which was rescued by IL-4c administration (Fig 7D). Notably, no change in the survival rate of neutrophils in dependence of eosinophil depletion was seen (Fig 7E) suggesting that the decreased efferocytosis is due to a decreased phagocytotic activity of macrophages.

Next we studied whether IL-4c administration can rescue the formation of inflammatory regions in eosinophil-depleted mice. Analysis of the cellular neighborhood of zymosan showed a similar cell cluster distribution in control and IL-4c-treated nondepleted mice (Fig 8A), although IL-4c administration induced M0 macrophages to shift from a direct to a random neighbor of zymosan. This can be attributed to the overall increased number of M0 macrophages in

Figure 4. Eosinophil depletion delays resolution of zymosan-induced inflammation.

A–C FACS analysis of eosinophils in the blood (panel A,B; $n = 6$ mice) or paws (panel C; $n = 8$ mice) at the indicated time points after zymosan injection. Anti-Siglec F antibody or the IgG-control (control) was administered with 0.883 mg/kg 24 h prior zymosan injection. Data are shown as mean ± SEM, student's *t*-test *$P < 0.05$, **$P < 0.01$, ***$P < 0.001$ vs. control mice.

D Paw volume after injection of zymosan. Data are presented as mean ± SEM ($n = 8$–10 mice). Two-way ANOVA/Bonferroni, ***$P < 0.001$.

E, F Zymosan-induced mechanical (panel E) and thermal (panel F) hypersensitivity of control or anti-Siglec F antibody-treated mice. Data are shown as the mean ± SEM ($n = 8$ mice). Two-way ANOVA/Bonferroni, **$P < 0.01$, ***$P < 0.001$ vs. control mice.

Source data are available online for this figure.

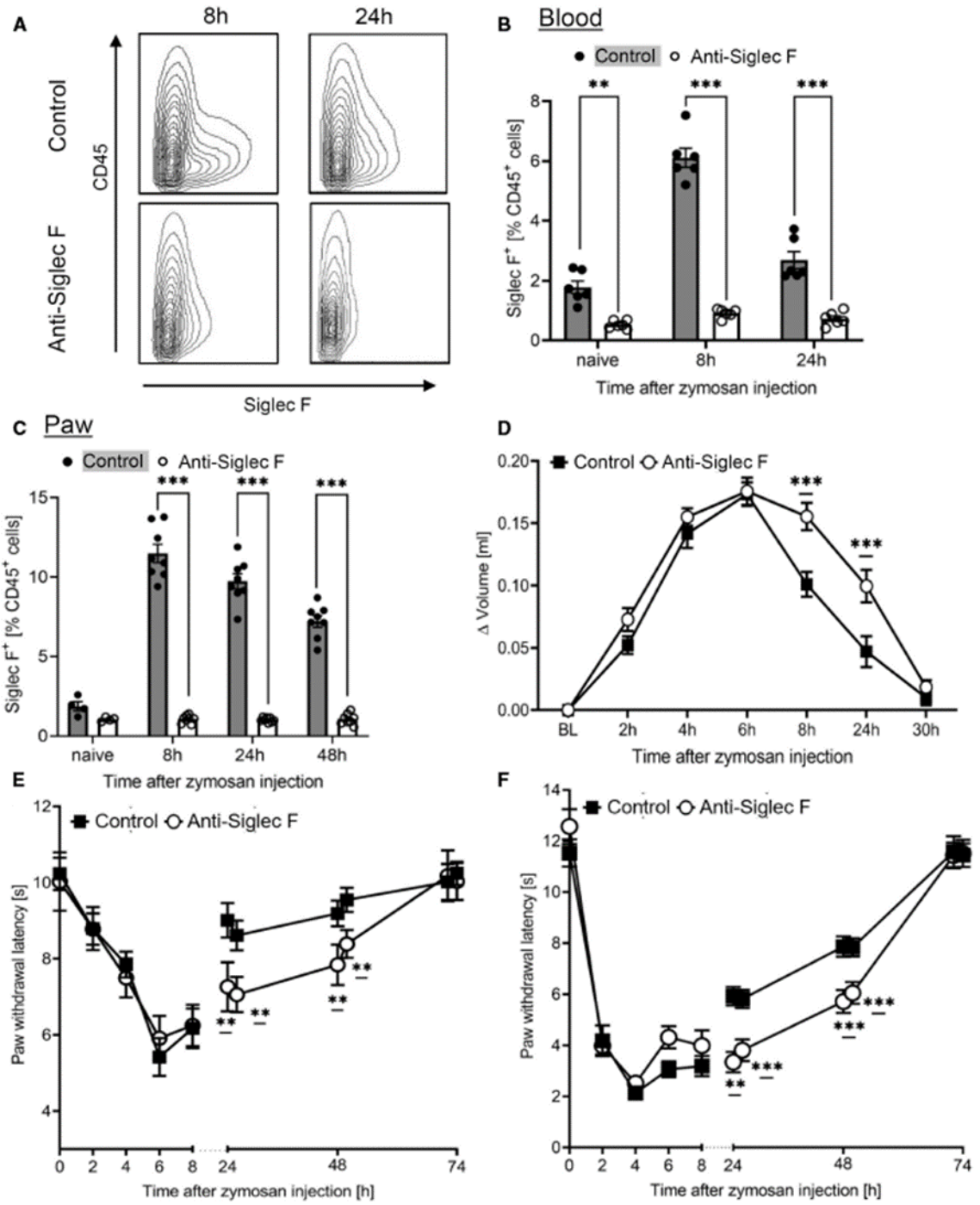

Figure 4.

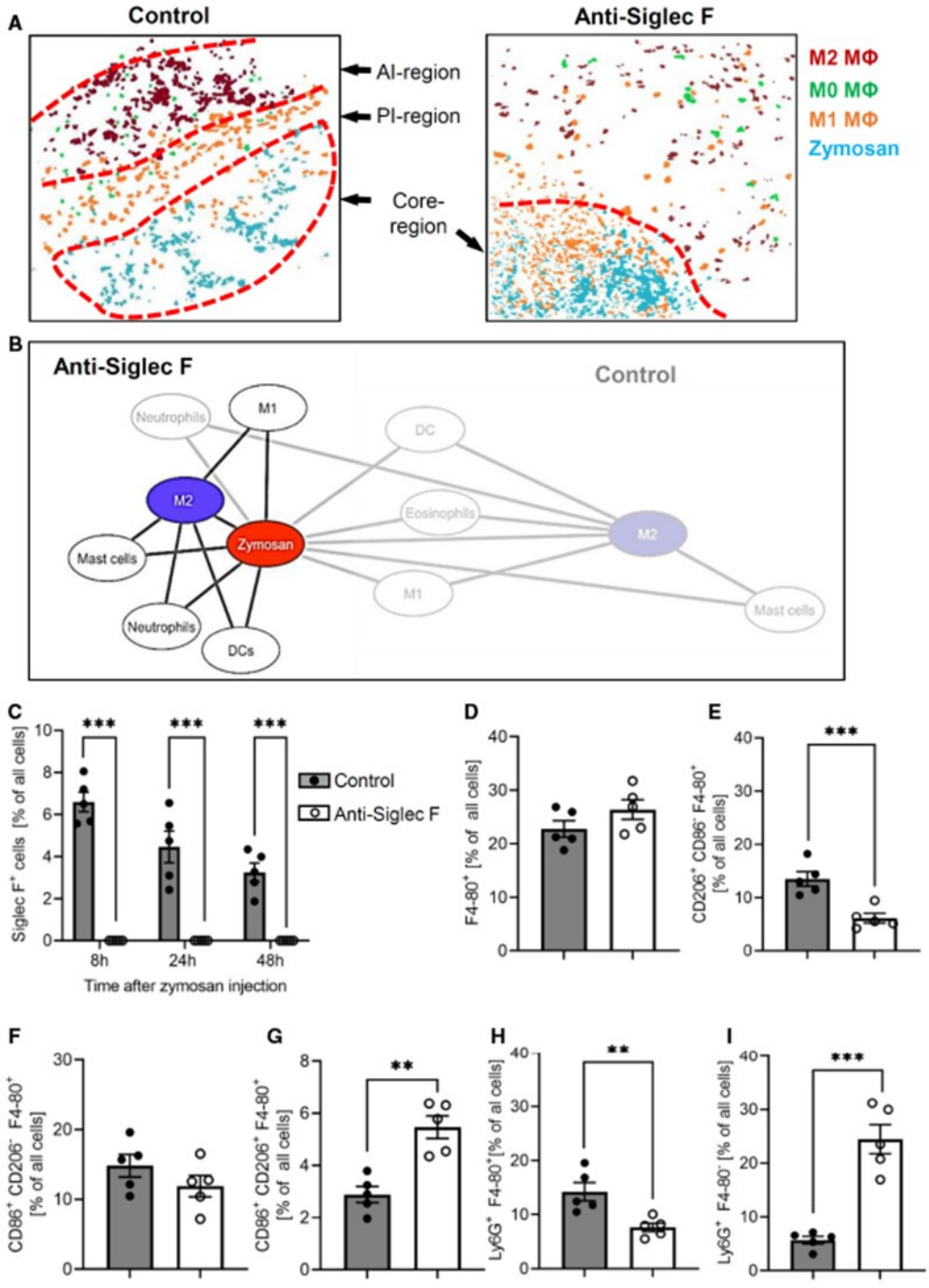

Figure 5.

Figure 5. Eosinophils maintain inflammatory regions.

A Composite MELC image showing the disappearance of the PI- and the AI-regions 24 h after zymosan injection in control or eosinophil-depleted mice. The red dotted lines depict the area where the transition between the neighboring regions occurs.

B Network visualization of the cellular neighborhoods of zymosan and M2-like macrophages 24 h after zymosan injection in eosinophil-depleted mice superimposed on control (transparent labels and lines as shown in Fig 2C).

C–I Quantification of eosinophils, the sum of all macrophages, M2-like, M1-like, and M0-macrophages (panels C–G) as well as efferocytosis (panel H) and neutrophils (panel I) in the MELC images of paws from control or eosinophil-depleted mice 24 h after zymosan injection. Data are presented as mean ± SEM ($n = 5$). Student's t-test, $^{**}P < 0.01$, $^{***}P < 0.001$.

Source data are available online for this figure.

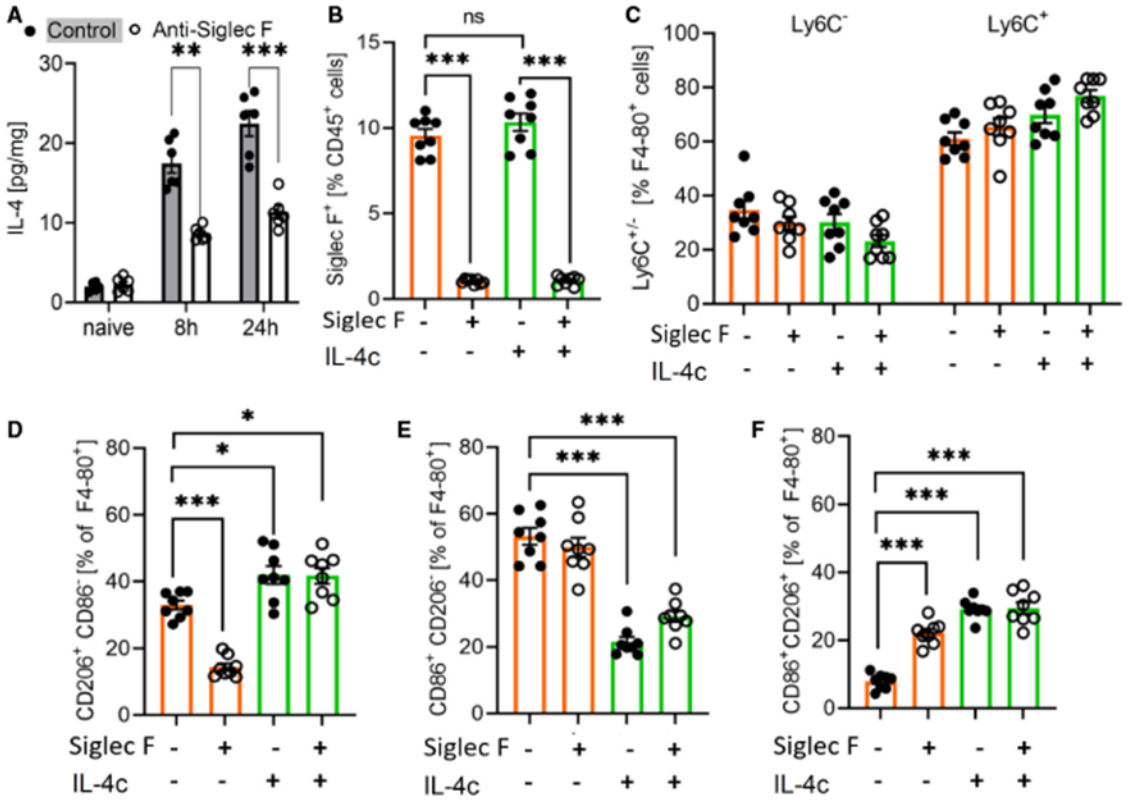

Figure 6. IL-4 mediates eosinophil effects during resolution of inflammation.

A IL-4 levels in paws from naive and zymosan-injected mice were determined by ELISA 8 and 24 h after injection of zymosan in paws of control or eosinophil-depleted mice. Data are shown as mean ± SEM ($n = 6$ mice). Student's t-test/two-way ANOVA/Bonferroni, control vs. anti-Siglec F antibody treatment: $^{**}P < 0.01$, $^{***}P < 0.001$.

B FACS analysis of the eosinophil number in paws from control and eosinophil-depleted mice with or without IL-4c treatment 24 h prior zymosan injection. Data are shown as the mean ± SEM ($n = 8$ mice). Two-way ANOVA/Bonferroni $^{***}P < 0.001$.

C Same as panel B except that resident ($Ly6C^{-}$) and monocyte-derived macrophages ($Ly6C^{+}$) were determined.

D–F Same as panel B except that M2-like (panel D), M1-like (panel E) and M0 macrophages (panel F) were determined. Data are shown as mean ± SEM ($n = 8$ mice). Student's t-test/Two-way ANOVA/Bonferroni, control vs. anti-Siglec F antibody treatment: $^{*}P < 0.05$, $^{***}P < 0.001$.

Source data are available online for this figure.

these mice and as consequence of a more widespread distribution. In eosinophil-depleted mice, the most important effect is the reversal of the decreased relative distance between zymosan and M2-like macrophages, after IL-4c application (Fig 8A). Also the dual-centered network analysis for zymosan and M2-like macrophages showed that IL-4c application prevented the eosinophil depletion-

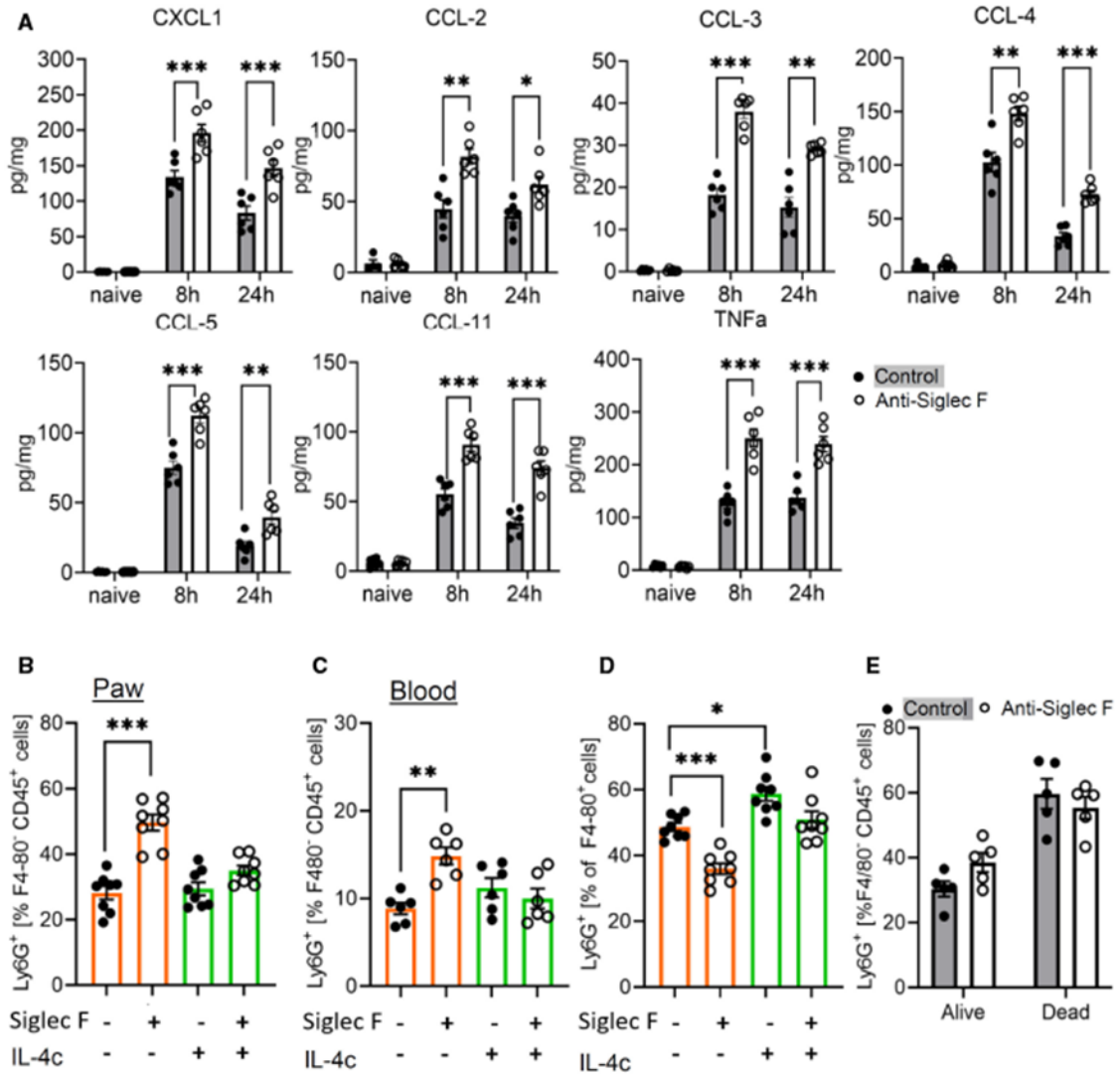

Figure 7. Eosinophil depletion increases neutrophil recruitment and lowers efferocytosis.

A Concentrations of cytokines and chemokines were determined by multiplex cytokine assay 8 and 24 h after injection of zymosan in paws from control or eosinophil-depleted mice. Data are mean ± SEM ($n = 6$ mice). Student's one-way ANOVA, significance between control and anti-Siglec F antibody treatment $^*P < 0.05$; $^{**}P < 0.01$; $^{***}P < 0.001$.

B, C FACS analysis of the neutrophil count in paws (panel B) and peripheral blood (panel C) from control or eosinophil-depleted mice with or without IL-4c treatment. Data are shown as the mean ± SEM ($n = 6$–8). Two-way ANOVA/Bonferroni, $^{**}P < 0.01$, $^{***}P < 0.001$.

D Same as panel B except that efferocytosis was determined. $^*P < 0.05$; $^{***}P < 0.001$.

E FACS analysis of alive and dying neutrophils in paws from control or eosinophil-depleted mice. Data are shown as the mean ± SEM ($n = 5$ mice).

Source data are available online for this figure.

induced collapse of the neighborhood architecture (Fig EV3). Visualization of cell cluster representing the major immune cell populations confirmed that IL-4c administration alone did not alter the basic overall structure of the inflammation in regard to the formation of the three inflammatory regions (Fig 8B) but was able to rescue the breakdown of the borders between the PI- and AI-regions

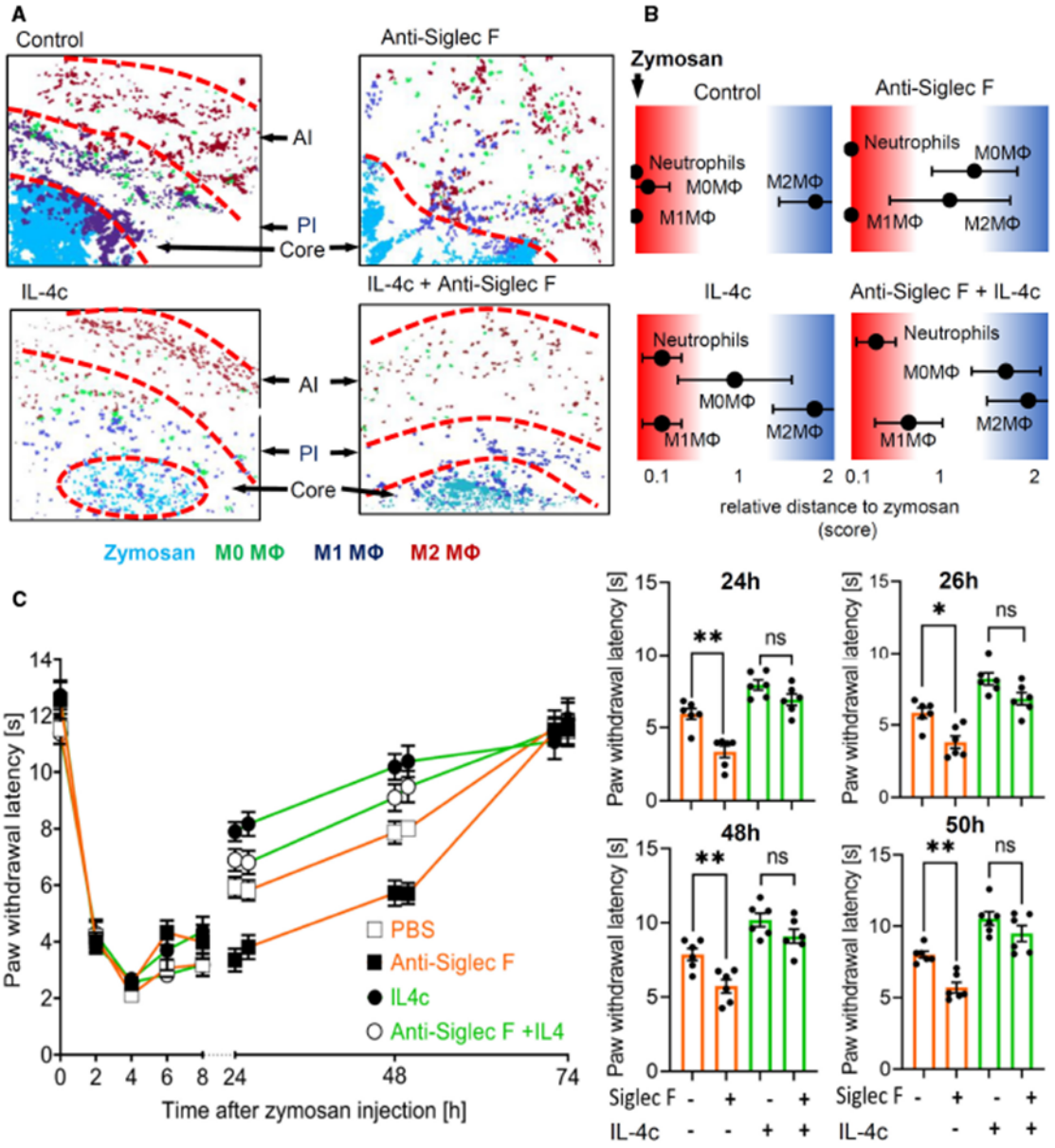

Figure 8. IL-4 mediates eosinophil effects on the inflammatory structure.

A Composite MELC image showing the disappearance of the pro- (PI) and the anti-inflammatory (AI) regions 24 h after zymosan injection. Shown are representative images of mice receiving anti-Siglec F or IL-4c. The red dotted lines depict the area where the transition between the neighboring regions occurs.

B Relative distance of various immune cell types based on the likelihood for a direct neighborhood of macrophage subtypes in regard to zymosan at the 24 h after zymosan injection. Data are shown as the mean ± SEM ($n = 5$ mice).

C Zymosan-induced thermal hypersensitivity in control or eosinophil-depleted mice with or without IL-4c treatment 24 h prior zymosan injection. The right panel shows the comparison of paw withdrawal latencies between the 4 treatment groups at the indicated time points. Data are shown as the mean ± SEM ($n = 6$ mice). Two-way ANOVA/Bonferroni, $^*P < 0.05$, $^{**}P < 0.01$; ns, not significant.

Source data are available online for this figure.

after eosinophil depletion (Fig 8B). Finally, IL-4c treatment removed the differences between control and eosinophil-depleted mice regarding the thermal paw withdrawal latencies during the resolution phase (24–48 h after zymosan injection; Fig 8C). Thus, we found that eosinophils support the resolution of zymosan-induced inflammation through IL-4 by enabling the development of an anti-inflammatory framework permitting appropriate macrophage polarization, neutrophil recruitment, and efferocytosis.

Discussion

Here, we identified three major inflammatory areas in our inflammation model based on the macrophage polarization and their cellular neighborhoods, whereby an inflammatory core region including the pathogen is surrounded by a proinflammatory region containing M1-like macrophages and an outer region containing anti-inflammatory cells. This regional structure, which starts to form within 8 h beginning with the polarization of M1-like macrophages in the neighborhood of the pathogen, is later followed by the formation of an outer region defined by M2-like macrophages. The finding that the pro- and anti-inflammatory regions coexist during an ongoing inflammation shows that the concept of a gradual temporal transition from pro- to anti-inflammation (Sansbury & Spite, 2016; Schett & Neurath, 2018; Serhan & Levy, 2018) needs further refinement in the sense that the temporal transition is reflective of a change in the ratio of the sizes of pro- and anti-inflammatory regions. The finding that the results of the MELC analysis were reproduced in the FACS analysis of total paw tissue, supports, and strengthen the point that the majority of M1-like and M2-like macrophages are indeed confounded to the specific inflammatory regions.

While probably a variety of events participate in the formation of the anti-inflammatory region, one triggering event may be neutrophil apoptosis. Recognition and phagocytosis of apoptotic neutrophils by M1-like macrophages has been shown to be a key element in the induction of resolution of inflammation (Filep, 2022). Efferocytosis has been demonstrated to induce a metabolic switch in macrophages and their reprogramming from M1-like to a M2-like phenotype (Morioka *et al*, 2018), which exhibits release of anti-inflammatory mediators (i.e. IL-10, TGF-β, and prostaglandin E2; Fadok *et al*, 1998; McDonald *et al*, 1999; Huynh *et al*, 2005; Girkontaite *et al*, 2007; Kumaran Satyanarayanan *et al*, 2019). However, also other signals from the inflammatory environment that can induce M2-like phenotypes in macrophages could be involved in the late appearance of these anti-inflammatory cells. In this regard, metabolic changes (i.e. bioenergetics) in immune cells can occur as response to external signals received either from other cells, such as signals and antigens activating pattern recognition receptors (PRRs) and cytokine receptors, or from changes in their microenvironment, including nutrient or oxygen availability (Tannahill *et al*, 2013), influencing transcriptional and posttranscriptional events in macrophages (O'Neill & Pearce, 2016). Thus, the formation of the AI-region might be initiated by early polarization events, leading then to the production of anti-inflammatory mediators by the M2-like macrophages. These mediators would over the time generate their own local microenvironment if located in a sufficient distance to the core region and the high density of proinflammatory signals in this region (Kern *et al*, 2018). Once this anti-inflammatory structure (in our model the AI-region) is established, newly recruited cells polarize according to the region they arrive in thereby reinforcing the character of this specific inflammatory region (Chen *et al*, 2020). The balance between the pro- and anti-inflammatory regions would depend on the amount of pro- and anti-inflammatory mediators generated locally ensuring a flexible response by expansion or shrinkage of either pro- or anti-inflammatory regions.

The observed basic architecture may provide the possibility to predict the role of an immune cell based on its localization within the given inflammatory setting. However, any attempt to make functional predictions based on the localization of an immune cell must take into consideration that several immune cell subtypes/phenotypes exist, which fulfill different and in some cases, for example, M1- and M2-like macrophages, even opposing functions (Murray & Wynn, 2011; Ortega-Gomez *et al*, 2013). We found that eosinophils were located in all three inflammatory regions, but adapted to its surroundings with an altered cytokine expression, which is in accordance to previous reports of environment-specific eosinophil subtypes (Andreev *et al*, 2020; Dolitzky *et al*, 2021). Depletion of eosinophils leads to increased neutrophil recruitment, decreased M2-like macrophage polarization, and decreased efferocytosis as well as the breakdown of the anti-inflammatory region. IL-4c administration restored these cellular functions, which is in line with previous publications showing that IL-4 is involved in the regulation of these three processes. However, since eosinophils are known to generate a multitude of mediators, it seems likely that eosinophil-derived IL-4 has a prominent role in mediating the observed phenotypes allowing to compensate for the loss of other potentially involved eosinophil-derived mediators. Although the net effect of eosinophil function in the zymosan-induced inflammation is anti-inflammatory, this net effect does not rule out local proinflammatory functions of eosinophils, that is, in the core region. Thus, the immune cells in question must be carefully examined for subtype-specific localizations, especially if they are located in regions, which would suggest opposing roles (i.e. core- and AI-region). In this regard, the observed seemingly even distribution of DCs throughout the three inflammatory regions may just be based on the lack of the use of more specialized DC markers.

It should be noted that the observed regional architecture of the zymosan-induced inflammation does not necessarily represent an architecture found in other inflammation models. The zymosan-induced inflammation model was chosen, since zymosan can be easily localized after fluorescence labeling (Pierre *et al*, 2017; Kern *et al*, 2018). This circumstance allows the immune response to form and maintain the observed regional structures. It would be expected that a similar inflammatory architecture will be seen in tissues with other pathogen-driven models for innate inflammation with relative immobile pathogens (e.g. bacteria, yeast). Moreover, it will be interesting to see if inflammation models with mixed immune responses, including components of the innate and the adaptive immune system, reproduce the observed structures or whether they exhibit other distinct inflammatory architectures. Finally, the methodological approach described in our report will allow new insights in therapeutic mechanisms and consequences, that is, immunosuppressants, in regard to immune cell interactions helping to refine therapeutic approaches.

Materials and Methods

Mice

Male C57BL/6N mice (6–8 weeks) were purchased from Janvier (Le Genest, France) and treated according to the International Association for the Study of Pain guidelines. For all experiments the ethics guidelines for investigations in conscious animals were obeyed and the procedures were approved by the local ethics committee (Regierungspräsidium Darmstadt). The animals had free access to food and water and were maintained in climate- (23 ± 0.5°C) and light-controlled rooms (light from 6.00 a.m. to 6.00 p.m.).

Inflammation was induced by injection of 10 µl zymosan (3 mg/ml in PBS; Merck, Darmstadt, Germany) subcutaneously into the plantar side of one hind paw. Eosinophil depletion was achieved by intraperitoneal (i.p.) injection of anti-Siglec F antibody (0.883 mg/kg; clone 238,047; R&D Systems, Minneapolis, MN) 24 h prior zymosan injection. As control purified rat IgG2a (Biolegend, San Diego, USA) was used. IL-4c was prepared using IL-4 (Peprotech, Hamburg, Germany) and anti-IL4 antibody (Biolegend, San Diego, USA) (Finkelman *et al*, 1993; Milner *et al*, 2010; Jenkins *et al*, 2011) and administered i.p. (0.166 mg/kg IL-4 and 0.883 mg/kg anti-IL4 antibody) 24 h prior zymosan injection. (Finkelman *et al*, 1993; Milner *et al*, 2010; Jenkins *et al*, 2011).

Multiepitope-ligand-carthographie

Multiepitope-ligand-carthographie is an automated immunohistological imaging method that can be used to visualize high numbers of antibodies on the same sample (Pierre & Scholich, 2010; Pierre *et al*, 2017; Kornstädt *et al*, 2020). Briefly, paw tissue sections were taken at 10 µm thickness on silanized cover slips, fixed in 4% paraformaldehyde in PBS for 15 min, permeabilized with 0.1% Triton X100 in PBS for 15 min, and blocked with 3% BSA in PBS for 1 h. The tissue sample was placed on the stage of a Leica DM-IRE2 and a picture was taken. Then, in an automated procedure, the sample was incubated with bleachable fluorescence-labeled antibodies and washed with PBS. Afterward, phase-contrast and fluorescence signals were imaged by an Apogee-KX4 camera (Apogee Instruments, Logan, UT). A bleaching step was performed to delete fluorescence signals and the post-bleaching image was recorded. Then the next antibody was applied and the process was repeated. For data analysis, fluorescence images produced by each antibody were aligned pixel-wise and corrected for illumination faults using flat-field correction. The post-bleaching images were subtracted from their following fluorescence image. The antibodies used are listed in Appendix Table S1.

Image analysis

First, all grayscale antibody channel images were processed using ImageJ v1.52 (NIH, Bethesda, MD, USA) to diminish noise, background fluorescence, and remove artifacts for further analyses if necessary. Then Cell Profiler (v3.1.9) (McQuin *et al*, 2018) was used for additional illumination correction and the generation of a cell mask for single-cell segmentation using the images for propidiumiodide (cell nuclei) and CD45. The segmentation mask was imported in histoCAT (v1.76) (20) with the corresponding antibody channel images. All images, excluding the images used for single-cell mask generation, were z-score normalized and used for Barnes-Hut t-SNE (BH t-SNE) (Amir *et al*, 2013) and PhenoGraph analysis (Levine *et al*, 2015) as implemented in histoCAT. PhenoGraph defines cell clusters based on single-cell mask and marker colocalization (k set to 20 or 30). BH t-SNE scatter plot was overlaid with a colored PhenoGraph cluster map. PhenoGraph clusters were determined on their marker expression and classified as different cell types for quantification of cells in the images. The number of objects per cluster was normalized to the total number of objects in the cell mask to calculate the relative number of cells per cell type. PhenoGraph clusters were exported as CSV file and further analyzed with the SPADE (v3.0) tool for Matlab to generate Spanning-trees of density-normalized events using standard conditions (Qiu *et al*, 2011). After defining single cells with the segmentation mask in histoCAT the z-score normalized images were exported and used for a FACS-like analysis in FlowJo (v10.8.1). To investigate the relationship between clusters, neighborhood analysis was performed under standard conditions as implemented in histoCAT (Schapiro *et al*, 2017). Here, pairwise interactions between cell phenotypes are calculated for each cell and its neighbors at a user-defined distance (4 pixels) and compared to a randomized version of the cell distribution. The permutation test provides either a significant ($P < 0.05$) interaction, avoidance, or no likelihood at all between cell phenotypes. The gained result was a score between 0 and 100 for all clusters which was imported in Cytoscape (v3.8.2) to generate neighborhood networks showing relative distances to the defined centers (Otasek *et al*, 2019).

FACS analysis

Tissue preparation for polychromatic flow cytometry was performed as described previously (Suo *et al*, 2014). Single-cell suspensions were incubated with 2% Fc-blocking reagent (Mouse BD Fc Block; BD Pharmingen, NJ, USA) in PBS (10 min, 4°C), followed by incubation with an antibody cocktail (Appendix Table S1) for 30 min at 4°C. Samples were acquired with a FACS Canto II flow cytometer and analyzed using FlowJo software v10 (both BD Biosciences, Heidelberg, Germany). For gating, fluorescence minus 1 (FMO) controls were used.

Behavioral tests and edema measurement

Mechanical hypersensitivity was determined by measuring paw withdrawal latency using a plantar aesthesiometer (Dynamic Plantar Aesthesiometer, Ugo Basile). A force range of 0 to 5 g with a ramp of 0.5 g/s was applied with a steel rod of 2 mm in diameter, until a strong and immediate withdrawal occurred. The cutoff time was set to 20 s. Thermal hypersensitivity was determined using the Hargreaves test as described previously (Hohmann *et al*, 2017). Paw withdrawal latency was determined by increasing heat at the mid-plantar region of a paw at the same rate for each trial (up to 12% starting at 32°C) using an IITC Plantar Analgesia Meter (Hargreaves Test; IITC Life Science, Woodland Hills, CA, USA) with a cutoff time of 20 s. Baseline measurements were performed on two consecutive days before zymosan injection.

The size of paw edemas was determined at the indicated times after injection of zymosan in one hind paw. A plethysmometer (IITC

The paper explained

Problem
An inflammation comprises numerous immune cells, which are positioned related to their function thereby allowing the appropriate interactions with other immune cells. Identification of the relevant immune cell interactions *in vivo* is crucial for successful interventions in immunological processes, but are normally rudimentary due to the limited numbers of markers, which can be visualized.

Results
Using multiplex immunohistology we identified cellular neighborhoods of the immune cell subtypes involved in a localized TLR-type 2 inflammation. The pathogen-containing region bordered to a proinflammatory region, which was enclosed by an antiinflammatory region. This structure remained steady throughout the course of the inflammation. Eosinophil-derived IL-4 was essential for forming the regions and correct resolution of inflammation.

Impact
This study shows that a pathogen-driven inflammation is based on pro- and anti-inflammatory processes, which are spatially, but not temporally, separated. The identification of the internal architecture of an inflammation allows the prediction of immune cell functions and interactions based on their localization providing new possibilities to develop and assess therapeutic interventions.

Life Science, Woodland Hills, CA, USA) was used to quantify the edema volume by immersion of the mouse paw as described previously (Tarighi *et al*, 2019).

Cytokine measurements

Cytokine and chemokine levels in paws of mice were determined using the Bio-Plex Pro mouse cytokine group I kit (Bio-Rad Feldkirchen, Germany). The tissue was lysed in 400 µl lysis buffer with 1x Protease Inhibitor Cocktail (Roche, Mannheim, Germany) in Tissue Extraction Reagent (Thermo Fisher Sciemtific, Waltham, MS). Samples were cut in small pieces and then sonicated twice at 60% power for 10 s with an Ultrasonic Homogenizer (SONOPULS HD2070 MS73, Bandelin, Berlin, Germany). Afterward, all samples were centrifuged for 10 min at 10,000 *g* and the supernatant harvested. The concentration of total protein in the samples was assessed by the bicinchoninic acid assay. All samples were diluted to a final protein concentration of 200–900 µg/ml, according to the kit requirements. IL-1α, IL-1β, IL-2, IL-3, IL-4, IL-5, IL-6, IL-9, IL-10, IL-12p40, IL12-p70, IL-13, IL-17, Eotaxin, G-CSF, GM-CSF, IFN-γ, CXCL1, CCL2, CCL3, CCL4, CCL5, and TNF-α levels were determined using a Bioplex-200 (Bio-Rad, Feldkirchen, Germany) according to the manufacturer's protocol. IL-4 was also measured using the Mouse IL-4 Quantikine ELISA Kit (R&D Systems, Minneapolis, MN) according to the manufacturer's protocol.

Data analysis and statistics

Determination of statistically significant difference in all experiments was conducted with One- or Two-way analysis of variance (ANOVA) followed by *post hoc* Bonferroni-correction. Comparison of two groups was performd by Student's *t*-test with Welch's correction. In all animal experiments, the mice were randomized, and the researcher was blinded in behavioral experiments edema measurements. All data show biological replicates.

Data availability

This study includes no data deposited in external repositories.

Expanded View for this article is available online.

Acknowledgements
The study was funded by the Deutsche Forschungsgemeinschaft (DFG) grants SCH0817/3-3, SFB1039 (TP A08) and GRK2336 (TP07) as well as the LOEWE initiative ACLF-I (P02) and the Fraunhofer Cluster of Excellence for Immune-Mediated Diseases (CIMD), Frankfurt/Main.

Author contributions
Anja Kolbinger: Investigation; visualization; writing—review and editing. **Tim J Schäufele:** Investigation; writing—review and editing. **Hanna Steigerwald:** Investigation; writing—review and editing. **Joschua Friedel:** Investigation; writing—review and editing. **Sandra Pierre:** Resources; investigation; writing—review and editing. **Gerd Geisslinger:** Resources; supervision; funding acquisition; writing—review and editing. **Klaus Scholich:** Conceptualization; resources; supervision; funding acquisition; writing—original draft; project administration; writing—review and editing.

Disclosure and competing interests statement
The authors declare that they have no conflict of interest.

For more information
i HistoCat: https://www.bodenmillerlab.com/#/
ii Cell profiler: https://cellprofiler.org/

References

Amir ED, Davis KL, Tadmor MD, Simonds EF, Levine JH, Bendall SC, Shenfeld DK, Krishnaswamy S, Nolan GP, Pe'er D (2013) viSNE enables visualization of high dimensional single-cell data and reveals phenotypic heterogeneity of leukemia. *Nat Biotechnol* 31: 545–552

Andreev D, Liu M, Kachler K, Llerins Perez M, Kirchner P, Kölle J, Gießl A, Rauber S, Song R, Aust O *et al* (2020) Regulatory eosinophils induce the resolution of experimental arthritis and appear in remission state of human rheumatoid arthritis. *Ann Rheum Dis* 80: 451–468

Chen M, Tse G, Wong WT (2020) Interleukin-4 increases phagocytosis of necrotic cells by macrophages through scavenger receptor CD36. *Clin Exp Pharmacol Physiol* https://doi.org/10.1111/1440-168113399

Dolitzky A, Shapira G, Grisaru-Tal S, Hazut I, Avlas S, Gordon Y, Itan M, Shomron N, Munitz A (2021) Transcriptional profiling of mouse eosinophils identifies distinct gene signatures following cellular activation. *Front Immunol* 12: 802839

Driss V, El Nady M, Delbeke M, Rousseaux C, Dubuquoy C, Sarazin A, Gatault S, Dendooven A, Riveau G, Colombel JF *et al* (2016) The schistosome glutathione S-transferase P28GST, a unique helminth protein, prevents intestinal inflammation in experimental colitis through a Th2-type response with mucosal eosinophils. *Mucosal Immunol* 9: 322–335

Fadok VA, Bratton DL, Konowal A, Freed PW, Westcott JY, Henson PM (1998) Macrophages that have ingested apoptotic cells in vitro inhibit proinflammatory cytokine production through autocrine/paracrine mechanisms involving TGF-beta, PGE2, and PAF. *J Clin Invest* 101: 890 – 898

Filep JG (2022) Targeting neutrophils for promoting the resolution of inflammation. *Front Immunol* 13: 866747

Finkelman FD, Madden KB, Morris SC, Holmes JM, Boiani N, Katona IM, Maliszewski CR (1993) Anti-cytokine antibodies as carrier proteins. Prolongation of in vivo effects of exogenous cytokines by injection of cytokine-anti-cytokine antibody complexes. *J Immunol* 151: 1235 – 1244

Friedenberger M, Bode M, Krusche A, Schubert W (2007) Fluorescence detection of protein clusters in individual cells and tissue sections by using toponome imaging system: Sample preparation and measuring procedures. *Nat Protoc* 2: 2285 – 2294

Girkontaite I, Urbonaviciute V, Maseda D, Neubert K, Herrmann M, Voll RE (2007) Apoptotic cells selectively suppress the Th1 cytokine interferon gamma in stimulated human peripheral blood mononuclear cells and shift the Th1/Th2 balance towards Th2. *Autoimmunity* 40: 327 – 330

Hoch T, Schulz D, Eling N, Gómez JM, Levesque MP, Bodenmiller B (2022) Multiplexed imaging mass cytometry of the chemokine milieus in melanoma characterizes features of the response to immunotherapy. *Sci Immunol* 7: eabk1692

Hohmann SW, Angioni C, Tunaru S, Lee S, Woolf CJ, Offermanns S, Geisslinger G, Scholich K, Sisignano M (2017) The G2A receptor (GPR132) contributes to oxaliplatin-induced mechanical pain hypersensitivity. *Sci Rep* 7: 446

Huynh M-LN, Malcolm KC, Kotaru C, Tilstra JA, Westcott JY, Fadok VA, Wenzel SE (2005) Defective apoptotic cell phagocytosis attenuates prostaglandin E2 and 15-hydroxyeicosatetraenoic acid in severe asthma alveolar macrophages. *Am J Respir Crit Care Med* 172: 972 – 979

Imhof BA, Aurrand-Lions M (2004) Adhesion mechanisms regulating the migration of monocytes. *Nat Rev Immunol* 4: 432 – 444

Jenkins SJ, Ruckerl D, Cook PC, Jones LH, Finkelman FD, van Rooijen N, MacDonald AS, Allen JE (2011) Local macrophage proliferation, rather than recruitment from the blood, is a signature of TH2 inflammation. *Science* 332: 1284 – 1288

Kern K, Schäfer SMG, Cohnen J, Pierre S, Osthues T, Tarighi N, Hohmann S, Ferreiros N, Brüne B, Weigert A *et al* (2018) The G2A receptor controls polarization of macrophage by determining their localization within the inflamed tissue. *Front Immunol* 9: 2261

Kolaczkowska E, Kubes P (2013) Neutrophil recruitment and function in health and inflammation. *Nat Rev Immunol* 13: 159 – 175

Kolbinger A, Kestner RI, Jencio L, Schäufele TJ, Vutukuri R, Pfeilschifter W, Scholich K (2022) Behind the wall-compartment-specific neovascularisation during post-stroke recovery in mice. *Cell* 11: 1659

Kornstädt L, Pierre S, Weigert A, Ebersberger S, Schäufele TJ, Kolbinger A, Schmid T, Cohnen J, Thomas D, Ferreirós N *et al* (2020) Bacterial and fungal toll-like receptor activation elicits type I IFN responses in mast cells. *Front Immunol* 11: 607048

Kumaran Satyanarayanan S, El Kebir D, Soboh S, Butenko S, Sekheri M, Saadi J, Peled N, Assi S, Othman A, Schif-Zuck S *et al* (2019) IFN-β is a macrophage-derived effector cytokine facilitating the resolution of bacterial inflammation. *Nat Commun* 10: 3471

Lastrucci C, Baillif V, Behar A, Al Saati T, Dubourdeau M, Maridonneau-Parini I, Cougoule C (2015) Molecular and cellular profiles of the resolution phase in a damage-associated molecular pattern (DAMP)-mediated peritonitis model and revelation of leukocyte persistence in peritoneal tissues. *FASEB J* 29: 1914 – 1929

Levine JH, Simonds EF, Bendall SC, Davis KL, Amir ED, Tadmor MD, Litvin O, Fienberg HG, Jager A, Zunder ER *et al* (2015) Data-driven phenotypic dissection of AML reveals progenitor-like cells that correlate with prognosis. *Cell* 162: 184 – 197

McDonald PP, Fadok VA, Bratton D, Henson PM (1999) Transcriptional and translational regulation of inflammatory mediator production by endogenous TGF-beta in macrophages that have ingested apoptotic cells. *J Immunol* 163: 6164 – 6172

McQuin C, Goodman A, Chernyshev V, Kamentsky L, Cimini BA, Karhohs KW, Doan M, Ding L, Rafelski SM, Thirstrup D *et al* (2018) CellProfiler 3.0: next-generation image processing for biology. *PLoS Biol* 16: e2005970

Milner JD, Orekov T, Ward JM, Cheng L, Torres-Velez F, Junttila I, Sun G, Buller M, Morris SC, Finkelman FD *et al* (2010) Sustained IL-4 exposure leads to a novel pathway for hemophagocytosis, inflammation, and tissue macrophage accumulation. *Blood* 116: 2476 – 2483

Moldoveanu D, Ramsay L, Lajoie M, Anderson-Trocme L, Lingrand M, Berry D, Perus LJM, Wei Y, Moraes C, Alkallas R *et al* (2022) Spatially mapping the immune landscape of melanoma using imaging mass cytometry. *Sci Immunol* 7: eabi5072

Morioka S, Perry JSA, Raymond MH, Medina CB, Zhu Y, Zhao L, Serbulea V, Onengut-Gumuscu S, Leitinger N, Kucenas S *et al* (2018) Efferocytosis induces a novel SLC program to promote glucose uptake and lactate release. *Nature* 563: 714 – 718

Murray PJ, Wynn TA (2011) Protective and pathogenic functions of macrophage subsets. *Nat Rev Immunol* 11: 723 – 737

Okabe Y, Medzhitov R (2014) Tissue-specific signals control reversible program of localization and functional polarization of macrophages. *Cell* 157: 832 – 844

O'Neill LAJ, Pearce EJ (2016) Immunometabolism governs dendritic cell and macrophage function. *J Exp Med* 213: 15 – 23

Ortega-Gomez A, Perretti M, Soehnlein O (2013) Resolution of inflammation: an integrated view. *EMBO Mol Med* 5: 661 – 674

Otasek D, Morris JH, Bouças J, Pico AR, Demchak B (2019) Cytoscape automation: empowering workflow-based network analysis. *Genome Biol* 20: 185

Panda SK, Wigerblad G, Jiang L, Jiménez-Andrade Y, Iyer VS, Shen Y, Boddul SV, Guerreiro-Cacais AO, Raposo B, Kasza Z *et al* (2020) IL-4 controls activated neutrophil FcγR2b expression and migration into inflamed joints. *Proc Natl Acad Sci USA* 117: 3103 – 3113

Pierre S, Scholich K (2010) Toponomics: studying protein-protein interactions and protein networks in intact tissue. *Mol Biosyst* 6: 641 – 647

Pierre S, Linke B, Suo J, Tarighi N, Del Turco D, Thomas D, Ferreiros N, Stegner D, Frolich S, Sisignano M *et al* (2017) GPVI and thromboxane receptor on platelets promote proinflammatory macrophage phenotypes during cutaneous inflammation. *J Invest Dermatol* 137: 686 – 695

Qiu P, Simonds EF, Bendall SC, Gibbs KDJ, Bruggner RV, Linderman MD, Sachs K, Nolan GP, Plevritis SK (2011) Extracting a cellular hierarchy from high-dimensional cytometry data with SPADE. *Nat Biotechnol* 29: 886 – 891

Rigoni A, Colombo MP, Pucillo C (2018) Mast cells, basophils and eosinophils: from allergy to cancer. *Semin Immunol* 35: 29 – 34

Sansbury BE, Spite M (2016) Resolution of acute inflammation and the role of Resolvins in immunity, thrombosis, and vascular biology. *Circ Res* 119: 113 – 130

Schapiro D, Jackson HW, Raghuraman S, Fischer JR, Zanotelli VRT, Schulz D, Giesen C, Catena R, Varga Z, Bodenmiller B (2017) histoCAT: analysis of cell phenotypes and interactions in multiplex image cytometry data. *Nat Methods* 14: 873 – 876

Schett G, Neurath MF (2018) Resolution of chronic inflammatory disease: universal and tissue-specific concepts. *Nat Commun* 9: 3261

Schubert W, Bonnekoh B, Pommer AJ, Philipsen L, Böckelmann R, Malykh Y, Gollnick H, Friedenberger M, Bode M, Dress AWM (2006) Analyzing proteome topology and function by automated multidimensional fluorescence microscopy. *Nat Biotechnol* 24: 1270 – 1278

Schuh CD, Pierre S, Weigert A, Weichand B, Altenrath K, Schreiber Y, Ferreiros N, Zhang DD, Suo J, Treutlein EM *et al* (2014) Prostacyclin mediates neuropathic pain through interleukin 1ß-expressing resident macrophages. *Pain* 155: 545 – 555

Serhan CN, Levy BD (2018) Resolvins in inflammation: emergence of the pro-resolving superfamily of mediators. *J Clin Invest* 128: 2657 – 2669

Shi C, Pamer EG (2011) Monocyte recruitment during infection and inflammation. *Nat Rev Immunol* 11: 762 – 774

Suo J, Linke B, dos Santos SM, Pierre S, Stegner D, Zhang DD, Denis CV, Geisslinger G, Nieswandt B, Scholich K (2014) Neutrophils mediate edema formation but not mechanical allodynia during zymosan-induced inflammation. *J Leukoc Biol* 96: 133 – 142

Tannahill GM, Curtis AM, Adamik J, Palsson-McDermott EM, McGettrick AF, Goel G, Frezza C, Bernard NJ, Kelly B, Foley NH *et al* (2013) Succinate is an inflammatory signal that induces IL-1β through HIF-1α. *Nature* 496: 238 – 242

Tarighi N, Menger D, Pierre S, Kornstädt L, Thomas D, Ferreirós N, Nüsing RM, Geisslinger G, Scholich K (2019) Thromboxane-induced α-CGRP release from peripheral neurons is an essential positive feedback loop in capsaicin-induced neurogenic inflammation. *J Invest Dermatol* 139: 656 – 664

Wang Y, Yang Y, Wang M, Wang S, Jeong J-M, Xu L, Wen Y, Emontzpohl C, Atkins CL, Duong K *et al* (2021) Eosinophils attenuate hepatic ischemia-reperfusion injury in mice through ST2-dependent IL-13 production. *Sci Transl Med* 13: eabb6576

Weller PF, Spencer LA (2017) Functions of tissue-resident eosinophils. *Nat Rev Immunol* 17: 746 – 760

Zimmermann N, McBride ML, Yamada Y, Hudson SA, Jones C, Cromie KD, Crocker PR, Rothenberg ME, Bochner BS (2008) Siglec-F antibody administration to mice selectively reduces blood and tissue eosinophils. *Allergy* 63: 1156 – 1163

Expanded View Figures

Figure EV1. Workflow of the bioinformatic analysis for the MELC images.

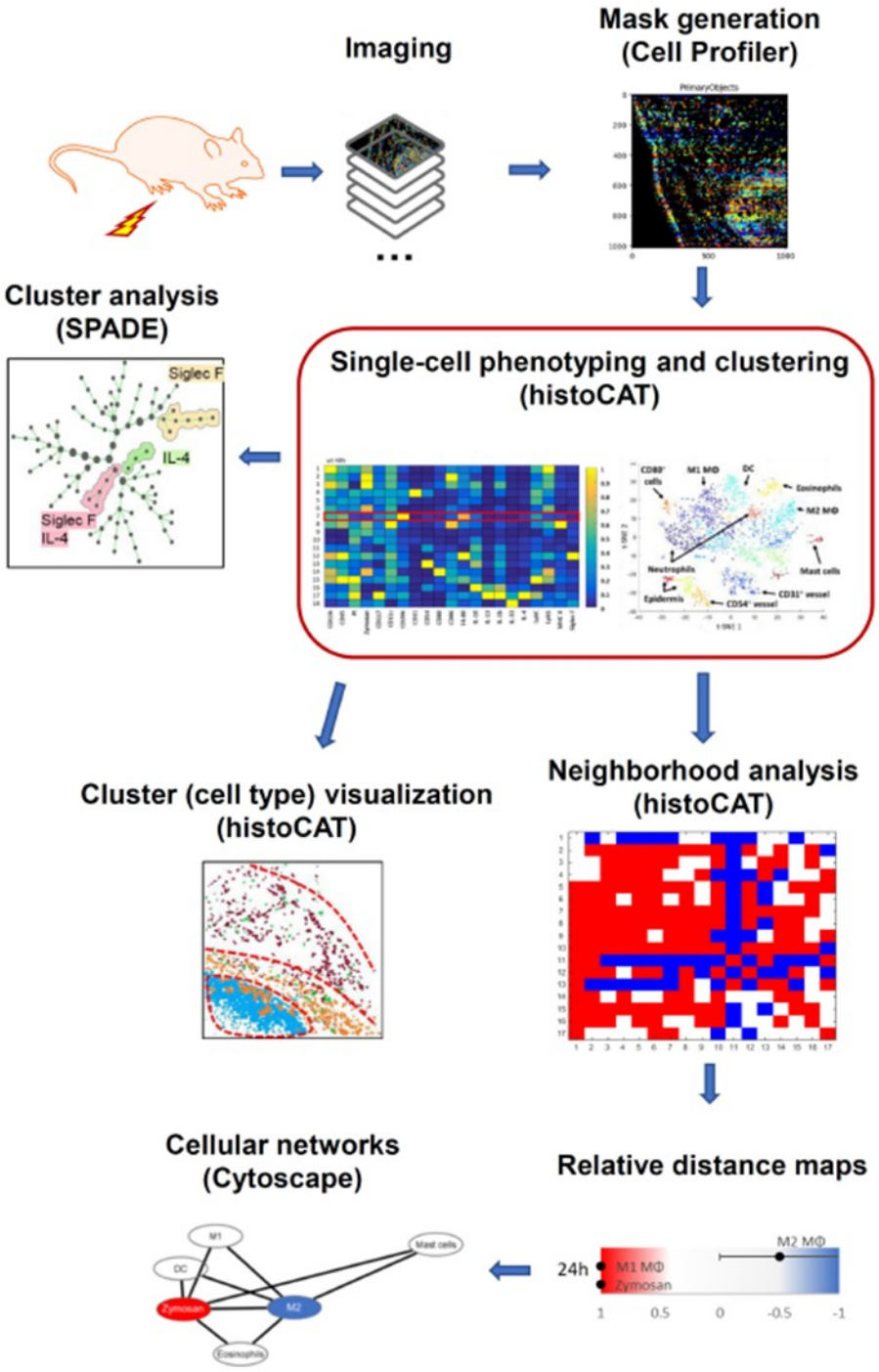

Figure EV1.

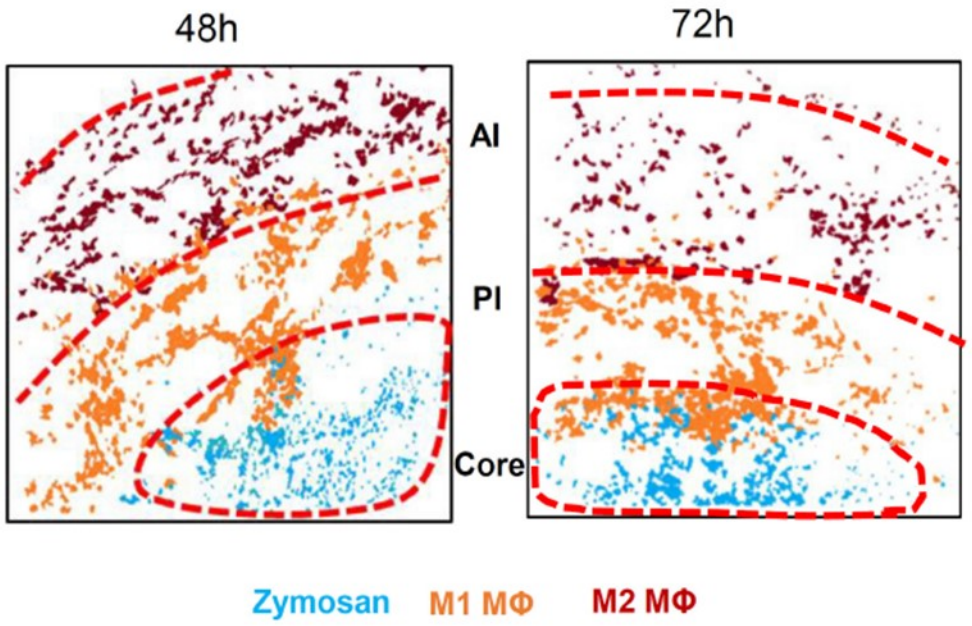

Figure EV2. Distribution of macrophage subpopulation 48 and 72 h after zymosan injection.

Composite MELC images 24 and 72 h after zymosan injection showing the position of the core-, PI- and the AI-regions in the tissue in regard to the localization of M1- and M2-like macrophages (MΦ) and zymosan. The red dotted lines depict the area where the transition between the neighboring regions occurs.

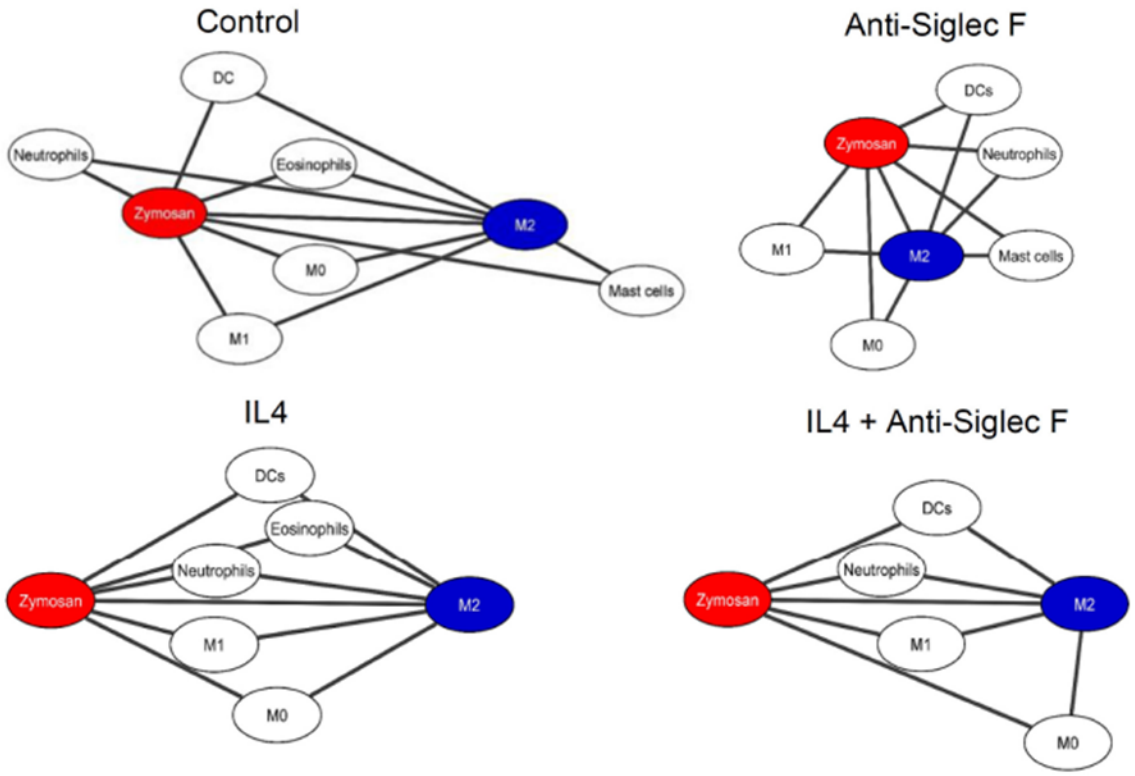

Figure EV3. Cellular neighborhood networks of zymosan and M2-like macrophages.

Dual centered network analysis of immune cells 24 h after zymosan injection based on the likelihood for a direct neighborhood of macrophage subtypes in regard to zymosan and M2-like macrophages at the. Data are shown as the mean ± SEM ($n = 5$ mice). Mice were treated with or without anti-Siglec F antibody and IL4c. The distances between the cells in the visualization represents the statistical probability of being direct neighbors.

Appendix table and figures

Appendix Table S1:

Table ST1: Antibodies used for MELC and FACS analysis

Target	Company	Clone number	Order number
CD3	Miltenyi Biotec	REAG1	130-109-838
CD4	Southern Biotech	L3T4	1540-02
CD8	BD Pharmingen	53-6.7	553030
CD11b	BioRad	M1/70.15	MCA74F
CD11c	Miltenyi Biotec	N418	130-102-799
CD19	BDPharmingen	1D3	557398
CD22	Miltenyi Biotec	Cy34.1	130-102-576
CD25	Miltenyi Biotec	7D4	130-102-550
CD29	Miltenyi Biotec	HMβ1-1	130-102-557
CD31	BD Biosciences	MEC13.3	553373
CD41	AbDSerotec	MWReg30	MCA2245F
CD45	Miltenyi Biotec	30F11.1	130-116-535
CD54	Biolegend	YN1/1.7.4	116105
CD80	Biolegend	16-10A1	104706
CD86	Biolegend	GL-1	105002
CD117	Bioss		bs-10005R-Cy5
CD127	eBiosciences	A7R34	11-1271-82
CD206	Biolegend	C068C2	141708
CD209	eBiosciences	LWC06	11-2092-80
Cytokeratin	eBiosciences	AE1/AE3	53-9003-82
CD335	Invitrogen	29A1.4	11-3351-82
F4-80	Biolegend	BM8	123107
GATA3	Santa Cruz	HG3-31	sc-268
IFNg	eBioscience	XMG1.2	12-7311-41
IL1b	Thermo Fisher	NJTEN3	11-7114-82
IL-4	Biolegend	11b11	504109
IL-6	eBioscience	MP5-20F3	11-7061-82
IL-10	eBioscience	JES5-16E3	11-7101-41
IL13	invitrogen	eBio13A	53-7133-82
IL-33	R&D	396118	IC3626P
Ki67	eBioscience	SolA15	11-5698-80
Ly6C	eBioscience	HK 1.4	17-5932-80
Ly6G	eBioscience	RB6-8C5	RM3005
MHC II	Miltenyi Biotec	REA813	130-112-233
NK1.1	BDPharmingen	PK136	561046
Propidium Iodide	Sigma		P4170
RORgt	eBioscience	B2D	12-6981-80
Sca1(Ly-6A/E)	Biolegend	E13-161.7	122511
Siglec F	BD Bioscience	E50-2440	552126
TNFa	Miltenyi	REA636	130-119-561
Antibodies used only for FACSAnalysis			
CD45	Miltenyi Biotec	REA737	130-110-665
Siglec F	Miltenyi Biotec	ES22-10D8	130-102-167
Ly6G	Biolegend	1A8	127624

Appendix Fig. S2

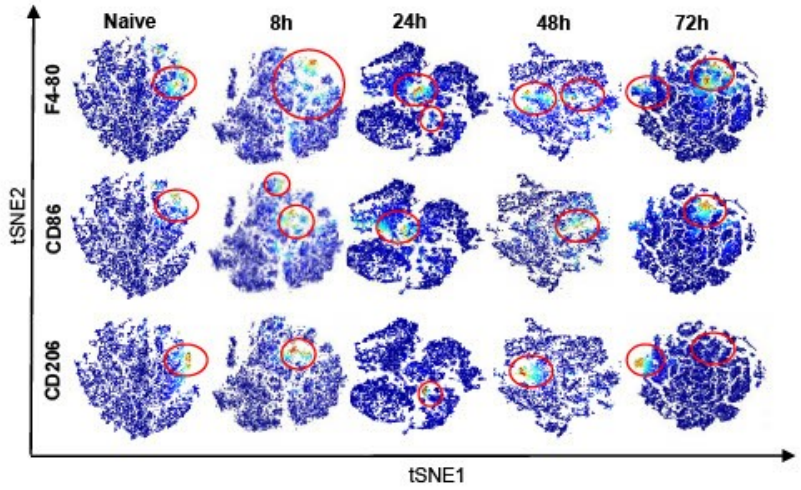

Fig. S2: MELC-based bioinformatic analysis of macrophage polarization. tSNE analysis of macrophage polarization based on M1-like (CD86) and M2-like (CD206) markers at various time points after zymosan injection in one hind paw

Appendix Fig. S3

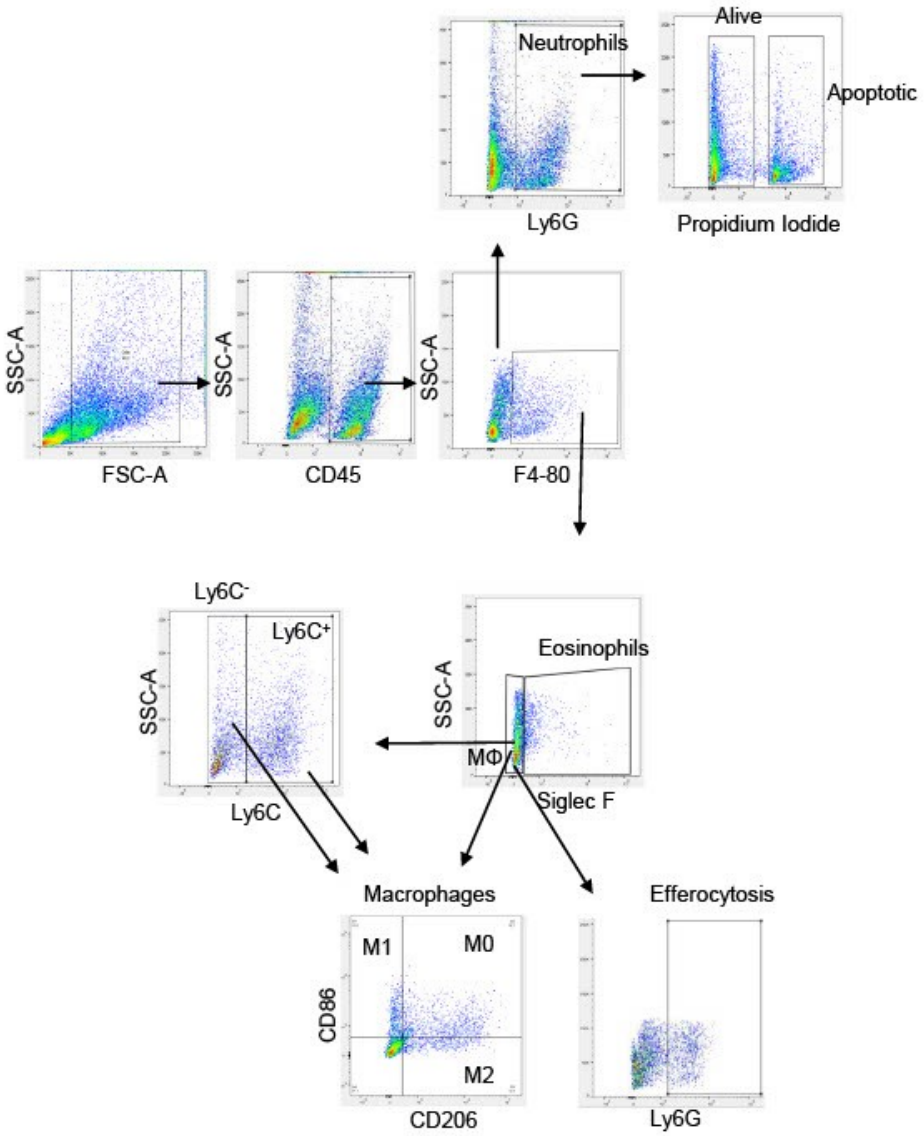

Fig. S3: Gating strategy for immune cells and their subtypes in paws after injection of zymosan (10 µl, 3 mg/ml). Cells were gated based on their side scatter area (SSC-A) and forward scatter area (FSC-A). Afterwards $CD45^+$ immune cells were identified. Within $F4\text{-}80^+$ cells $Siglec\ F^-$ cells were identified as macrophages and $Siglec\ F^+$ cells as eosinophils. $F4\text{-}80^+$ $Siglec\ F^-$ macrophages were also further analysed for in resident ($Ly6C^-$) and monocyte-derived macrophages ($Ly6C^+$). M1-like macrophages were defined as $CD86^+/CD206^-$ cells, M2-like macrophages as $CD86^-/CD206^+$ cells and double positive macrophages as M0 macrophages.
$Ly6G^+/F4\ 80^-$ cells were identified as neutrophils. The neutrophils were divided in dead cells positive for propidium iodide and alive cells negative for propidium iodide.

Appendix Fig. S4

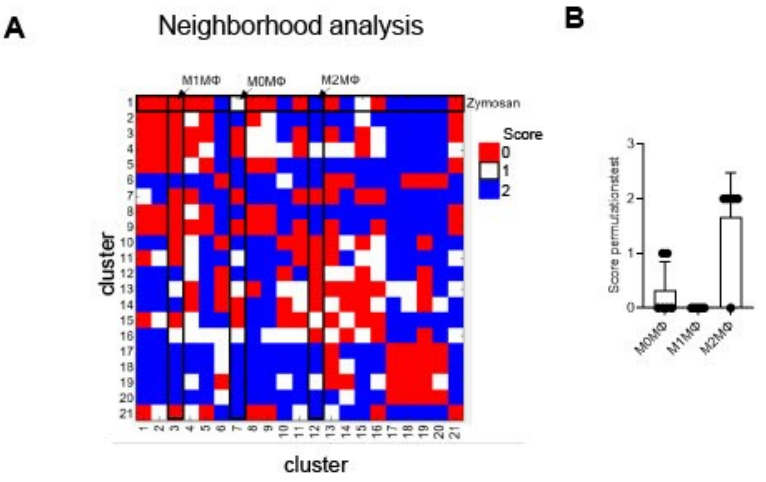

Fig. S4: MELC-based neighborhood analysis of zymosan and macrophage subpopulations. (A) Representative analysis of the zymosan neighborhood in inflamed paws 24 h after zymosan injection. Score 0 = neighbors, Score 1 = random distribution, score 2 = no neighbors. **(B)** Score distribution of macrorphage populations determined for the zymosan neighborhood in individual mice 24 h after zymosan injection.

Appendix Fig. S5

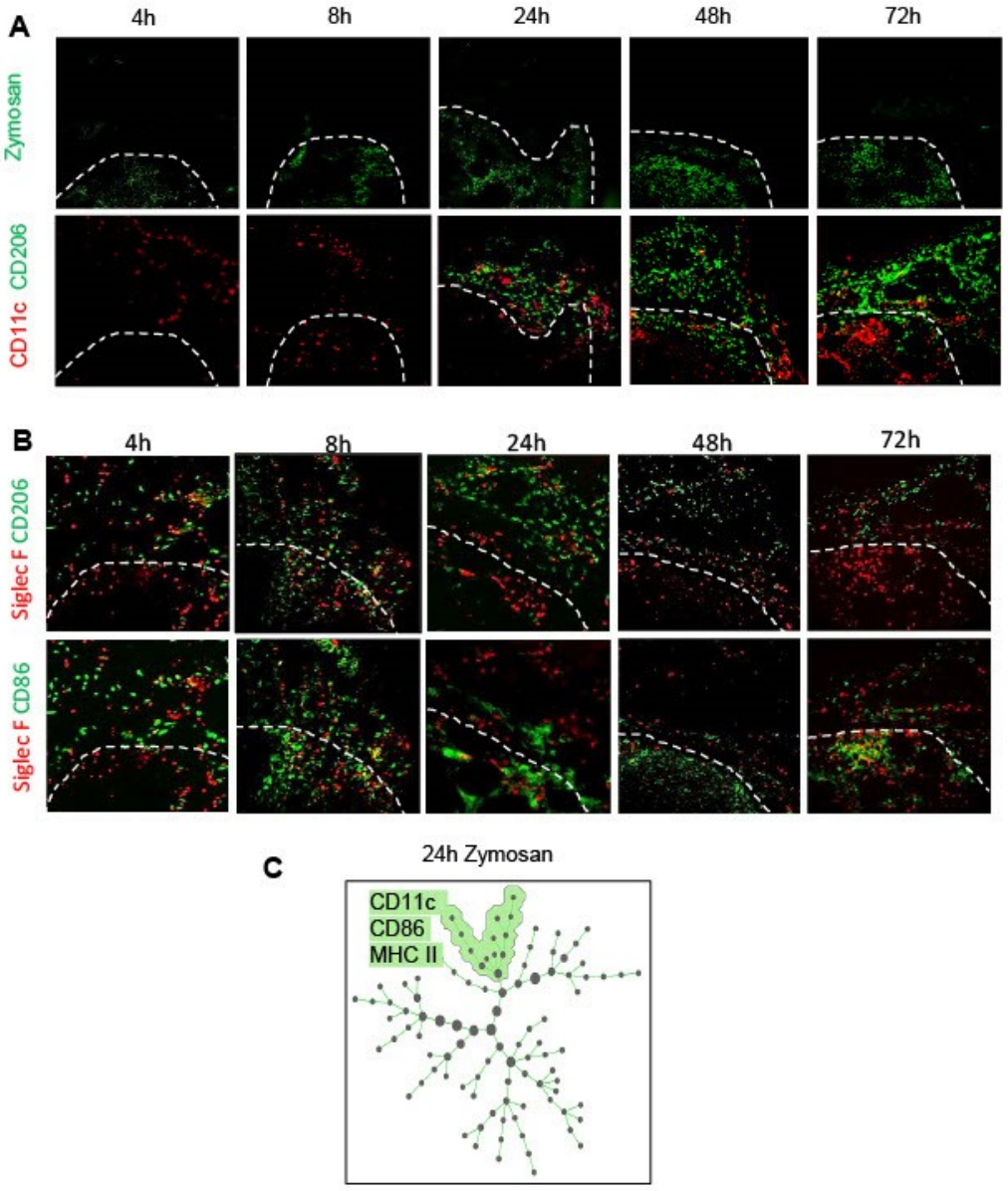

Fig. S5: MELC analysis for the distribution and dendritic cells and eosinophils. (A, B) Representative MELC images showing the distribution of DCs (panel A) and eosinophils (panel B) in the inflamed paw at different time points after zymosan injection. The white dotted lines depict the border of the core region. **(C)** SPADE analysis of the distribution of CD11c-expressing clusters 24 hours after zymosan injection in one hind paw.

Appendix Fig. S6

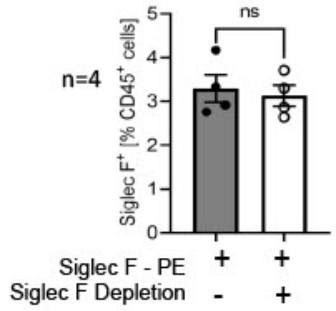

Fig. S6: The anti Siglec F-depletion antibody does not interfere with binding of the eosinophil detection antibody. Blood cells were incubated either with the anti-Siglec F FACS antibody (clone ES22-10D8, Miltenyi Biotech) alone or together with equal amounts of the depletion antibody (clone 238047, R&D Systems). Data are mean ± S.E.M. (n=4). Students T-test was used. No significance was detected.

Appendix Fig. S7

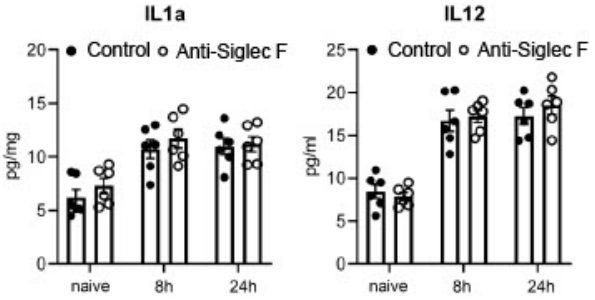

Fig. S7: Eosinophil-depletion does not alter IL1a and IL12 levels in inflamed hind paws. Concentrations of cytokines and chemokines were determined by multiplex cytokine assay 8 and 24 h after injection of zymosan in paws from control or eosinophil-depleted mice. Data are mean ± S.E.M. (n=6). Two-way ANOVA. No significance was detected.

Appendix Fig. S8

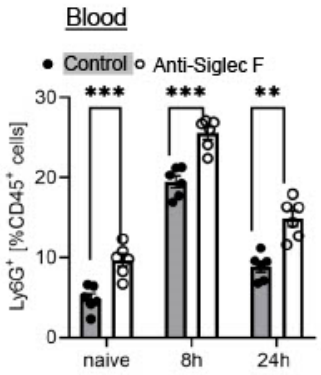

Fig. S8: FACS analysis of neutrophils in blood. FACS analysis of the neutrophil count in peripheral blood from control or eosinophil-depleted mice in naïve animals and 8 or 24 hours after zymosan injection. Data are shown as the mean ± S.E.M. (n=6). Two-way ANOVA/Bonferroni, **p< 0.01, ***p< 0.001.

cells

MDPI

Article

Behind the Wall—Compartment-Specific Neovascularisation during Post-Stroke Recovery in Mice

Anja Kolbinger [1,†], Roxane Isabelle Kestner [2,3,†], Lara Jencio [2], Tim J. Schäufele [1], Rajkumar Vutukuri [3], Waltraud Pfeilschifter [3,4,†] and Klaus Scholich [1,5,6,*,†]

[1] Institute of Clinical Pharmacology, *pharmazentrum frankfurt* Goethe-University, D-60590 Frankfurt am Main, Germany; kolbinger@med.uni-frankfurt.de (A.K.); schaeufele@med.uni-frankfurt.de (T.J.S.)
[2] Department of Neurology, Hospital of the Goethe University Frankfurt, Theodor-Stern-Kai 7, D-60590 Frankfurt am Main, Germany; roxane-isabelle.kestner@kgu.de (R.I.K.); lara.jencio@gmx.de (L.J.)
[3] Institute of Pharmacology and Toxicology, *pharmazentrum frankfurt* Goethe-University, D-60590 Frankfurt am Main, Germany; vutukuri@med.uni-frankfurt.de (R.V.); waltraud.pfeilschifter@klinikum-lueneburg.de (W.P.)
[4] Department of Neurology and Clinical Neurophysiology, Municipal Hospital Lüneburg, D-21339 Lüneburg, Germany
[5] Fraunhofer Institute for Translational Medicine and Pharmacology ITMP, Theodor-Stern-Kai 7, D-60596 Frankfurt am Main, Germany
[6] Fraunhofer Cluster of Excellence for Immune-Mediated Diseases CIMD, Theodor-Stern-Kai 7, D-60596 Frankfurt am Main, Germany
* Correspondence: scholich@em.uni-frankfurt.de
† These authors contributed equally to this work.

Citation: Kolbinger, A.; Kestner, R.I.; Jencio, L.; Schäufele, T.J.; Vutukuri, R.; Pfeilschifter, W.; Scholich, K. Behind the Wall—Compartment-Specific Neovascularisation during Post-Stroke Recovery in Mice. *Cells* 2022, *11*, 1659. https://doi.org/10.3390/cells11101659

Academic Editors: Ken Arai, Kazuto Masamoto, Elga Esposito, Wenlu Li and Emiri T. Mandeville

Received: 5 April 2022
Accepted: 13 May 2022
Published: 17 May 2022

Publisher's Note: MDPI stays neutral with regard to jurisdictional claims in published maps and institutional affiliations.

Abstract: Ischemic stroke is a highly prevalent vascular disease leading to oxygen- and glucose deprivation in the brain. In response, ischemia-induced neovascularization occurs, which is supported by circulating $CD34^+$ endothelial progenitor cells. Here, we used the transient middle cerebral artery occlusion (tMCAO) mouse model to characterize the spatio-temporal alterations within the ischemic core from the acute to the chronic phase using multiple-epitope-ligand cartography (MELC) for sequential immunohistochemistry. We found that around 14 days post-stroke, significant angiogenesis occurs in the ischemic core, as determined by the presence of $CD31^+/CD34^+$ double-positive endothelial cells. This neovascularization was accompanied by the recruitment of $CD4^+$ T-cells and dendritic cells as well as $IBA1^+$ and $IBA1^-$ microglia. Neighborhood analysis identified, besides pericytes only for T-cells and dendritic cells, a statistically significant distribution as direct neighbors of $CD31^+/CD34^+$ endothelial cells, suggesting a role for these cells in aiding angiogenesis. This process was distinct from neovascularization of the peri-infarct area as it was separated by a broad astroglial scar. At day 28 post-stroke, the scar had emerged towards the cortical periphery, which seems to give rise to a neuronal regeneration within the peri-infarct area. Meanwhile, the ischemic core has condensed to a highly vascularized subpial region adjacent to the leptomeningeal compartment. In conclusion, in the course of chronic post-stroke regeneration, the astroglial scar serves as a seal between two immunologically active compartments—the peri-infarct area and the ischemic core—which exhibit distinct processes of neovascularization as a central feature of post-stroke tissue remodeling. Based on our findings, we propose that neovascularization of the ischemic core comprises arteriogenesis as well as angiogenesis originating from the leptomenigeal vasculature.

Keywords: stroke; angiogenesis; dendritic cell; microglia; T-cell; multiplex immunohistochemistry

1. Introduction

Ischemic stroke is a highly prevalent vascular disease that carries a relevant burden of disability and socioeconomic strain. It is a consequence of the acute occlusion of a cerebral artery leading to oxygen- and glucose deprivation in the brain parenchyma of the respective

vascular territory. In this context, the activation of microglia and rapid deterioration of neurons occurs, leading to the release of damage-associated molecular pattern molecules (DAMPS) and thereby to further glial activation and subsequent secretion of cytokines and matrix metalloproteinases [1]. As a result, disruption of the blood–brain barrier (BBB) takes place, which paves the way for immune cell infiltration into the otherwise strictly immunologically privileged brain [2]. In the course of astrocyte activation, a broad glial scar forms around the ischemic border, virtually sealing the ischemic core (IC) off from the peri-infarct area. Whether it represents a protective mechanism keeping the surviving parenchyma separated from the inflamed and necrotic tissue or whether this separation in fact hinders regenerative processes to expand into the ischemic core is not yet clearly understood [3,4].

So far, studies on post-stroke recovery focused on the peri-infarct area because it is considered to represent the closest histological correlate of the penumbra. The penumbra was characterized in 1977 by Astrup et al. as a region where blood flow has dropped below the threshold necessary to uphold electrophysiological neuronal functions, but not yet below the threshold necessary to maintain structural integrity, retaining the potential of full recovery in case of reperfusion within a certain time window [5]. Today, all causal stroke therapies rely on this concept.

Furthermore, significant regenerative potential is attributed to the peri-infarct area, which is reflected, e.g., by the occurrence of strong ischemia-induced neovascularization [6]. This term summarizes three possible mechanisms: (a) *vasculogenesis*, the sprouting of new vasculature mainly taking place during embryogenesis and tumor formation, but also observed to a certain extent in cardio-vascular diseases [7]; (b) *arteriogenesis*, which means the enlargement of pre-existing collaterals mainly driven by shear stress sensed by the affected endothelium [8]; and (c) *angiogenesis*, where a stress signal such as ischemia activates endothelial cells to form new vessels, which is supported by circulating endothelial progenitor cells (EPCs) [9]. These EPCs share several characteristics with hematopoietic stem cells, e.g., the expression of hematopoietic progenitor cell antigen CD34 [10]. They stimulate or potentially even integrate into the activated endothelium of pre-existing vessels to differentiate into tip cells, which clear and guide the way for new sprouts through the surrounding extracellular matrix [11]. Tip cells are followed by stalk cells, which show high proliferative activity to elongate the forming vessel and create a vascular lumen and branches [12]. Supported by macrophages, tip cells subsequently fuse with other tip cells to build up vascular circuits [13]. During maturation, the newly formed vessels attract and integrate pericytes and other mural cells [14].

Although these newly formed vessels during post-stroke recovery have shown to lack a fully equipped BBB and possibly recede over the long term [15], angiogenesis has been associated with functional recovery [16]. It has been proposed that angiogenesis could support neural remodeling by stimulating neural progenitor cell proliferation through secreted mediators such as VEGF or BDNF [17] serving as scaffolds for the migration of those cells from the subventricular zone (SVZ) and supplier of nutrients and oxygen to enhance neural maturation [18]. Whether these processes also take place within the ischemic core remains elusive. So far, this compartment has received less attention as it is usually considered the necrotic remnant of the ischemic event.

Nevertheless, evidence is accumulating that certain aspects of the post-stroke inflammatory process are specific to this region [19,20]. It has been argued that stroke patients' outcomes rely less on the extent of the penumbra, which is relatively uniform between cases, and more on the varying volume of the ischemic core [21]. Multiple attempts to design immunomodulatory treatments for ischemic stroke have not yet translated into clinical therapeutic strategies. Therefore, a compartment-specific approach might be key to future research targets.

We therefore aimed at a comprehensive characterization of the spatio-temporal alterations within the ischemic core from the acute to the chronic phase after experimental stroke using a multiple-epitope immunohistochemical approach. For this purpose, mice

were nursed following an intensive post-stroke care protocol [22] and examined clinically and histologically at 1, 3, 7, 14 and 28 days after transient middle cerebral artery occlusion (tMCAO).

2. Materials and Methods

2.1. Ethics Statement

All animals involved in the presented experiments were approved by the local Ethics Committees for Animal Research (Darmstadt) under the permit number FU/1182. Experiments were performed in accordance with the German Protection of Animals Act and the guidelines for care and use of laboratory animals by the local committee (Regierungspräsidium Darmstadt).

2.2. Transient Middle Cerebral Artery Occlusion and Post-Stroke Care

In total, 25 male C57Bl/6J mice (25–30 g) at the age of 10 to 12 weeks old were purchased from Charles River Laboratories (Sulzfeld, Germany). The right middle cerebral artery was occluded as described previously [23]. In brief, mice were anesthetized using 1.5% isoflurane administered continuously via a breathing mask and kept on a temperature-controlled heating mat throughout surgeries. The right common and external carotid arteries were ligated before the insertion of a standard silicone-coated monofilament (6-0 medium, coating length 9 mm, catalog No. 6023910PK10; Doccol, Sharon, MA, USA) until the branching point of the middle cerebral artery. After 1 h, the filament was retracted to allow reperfusion. To achieve analgesia 0.1 mg/kg bodyweight buprenorphine was injected i.p. 30 min before surgery and every 8 h during the first 48 h. Up to 5 animals were grouped into cages and kept on a heating mat (Beurer, Ulm, Germany). The body weight, rectal temperature and clinical signs of pain, agitation or severe apathy were monitored daily. Functional scoring was performed on day 1, 3, 7, 14 and 28 after surgery, using the Experimental Stroke Scale (ESSf) developed by Lourbopoulos et al. [22]. This score comprises 11 items testing for sensory and motor dysfunction, neglect, behavioral and coordination deficits. To secure an adequate food and water supply, we followed the maximized post-stroke support protocol described before including easily accessible jelly food, oral feeding support and s.c. injections of warmed 0.9% saline adjusted to the animals' individual demand. The mortality rate was 24% including 3 mice that were excluded due to signs of herniation, subarachnoid hemorrhage, or late-onset ischemia. Surviving animals were followed-up for 24 h, 3 d, 7 d, 14 d or 28 d post-stroke, grouping 5 animals per observation timepoint. All procedures have been conducted in an unblinded and unrandomized manner as all animals received the same treatment and no intervention (e.g., drug administration) was performed. A total of 4 animals per group were used for MELC analysis. An overview of the study design is given in Figure 1A. All brains were examined macroscopically for signs of subarachnoid hemorrhage after removal. Tissue sections were macroscopically examined for blood-clot formations.

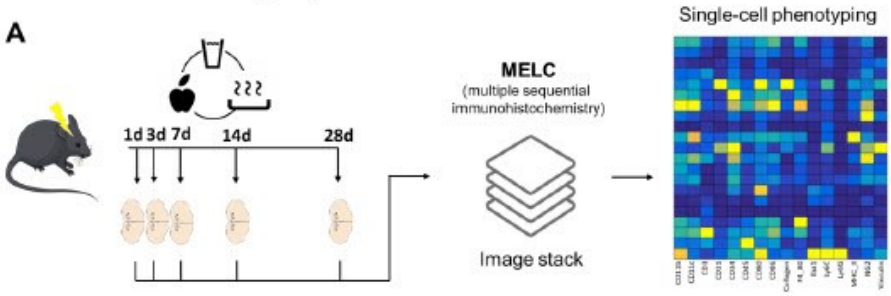

Figure 1. *Cont.*

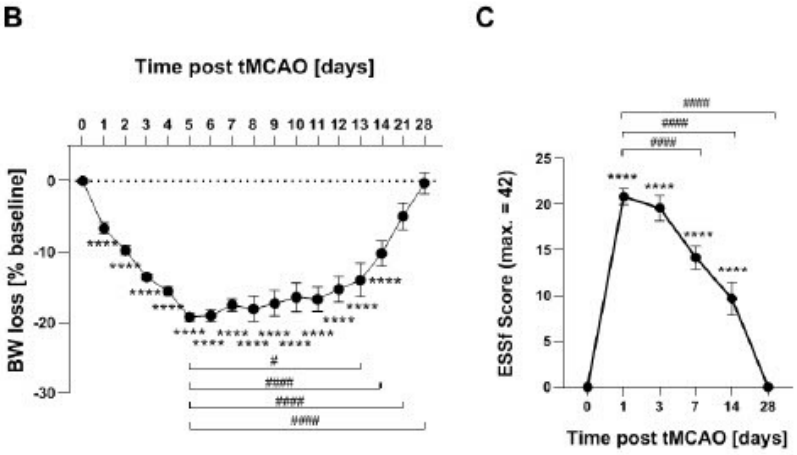

Figure 1. Long-term recovery in the tMCAO model. (**A**) Flow chart of study design. (**B**) Weight loss tMCAO surgery presented as percentage reduction from preoperative body weight ± SEM n = 25, **** $p < 0.0001$ vs. baseline, # $p < 0.05$, #### $p < 0.0001$ vs. d5. One-way ANOVA with Bartlett correction. (**C**) ESSf scores for mice taken at the indicated days after stroke induction ± SEM. n = 25, **** $p < 0.0001$ vs. baseline, #### $p < 0.0001$ vs. d5. One-way ANOVA with Bartlett correction.

2.3. Multi-Epitope-Ligand-Carthographie (MELC)

MELC technology is an automated immunohistological imaging method and can be used to visualize very high numbers of antibodies on the same sample as described before [24–26]. Briefly, whole brains were isolated and natively frozen in Tissue TEK O.C.T. Compound (Sakura Finetek, Torrance, CA, USA) on dry ice and stored at −80 °C until sectioning. Mid-brain coronal tissue sections were taken at a 10 µm thickness on silanized cover slips, fixed in 4% paraformaldehyde in PBS for 15 min, permeabilized with 0.1% Triton X100 in PBS for 15 min and blocked with 3% BSA in PBS for 1 h. The sample was placed on the stage of a Leica DM IRE2 and a picture was taken. Then, in an automated procedure, the sample was incubated for 15 min with bleachable fluorescence-labelled antibodies and rinsed with PBS. Afterward, the phase contrast and fluorescence signals were imaged by a cooled charge-coupled device camera (Apogee KX4, Apogee Instruments, Logan, UT, USA). A bleaching step was performed to delete fluorescence signals, and the post-bleaching image was recorded. Then, the next antibody was applied and the process was repeated. For data analysis, fluorescence images produced by each antibody were aligned pixel-wise and were corrected for illumination faults using flat-field correction. The post-bleaching images were subtracted from their following fluorescence image. The antibodies used are listed in Supplemental Table S1.

2.4. Analysis of MELC Data

In the first step, all greyscale antibody channel images were processed using ImageJ 1.52v to diminish noise, background fluorescence and remove artefacts for further analyses if necessary. The staining for NeuN, GFAP and Map2 were used to divide the images in areas containing stroke or healthy tissue. Subsequently, Cell Profiler (version 3.1.9) [27] was used for additional illumination correction and the generation of a cell mask for single-cell segmentation using the images for propidium iodide (cell nuclei) and CD45. The resulting segmentation mask was loaded into histoCAT (version 1.76) (20) together with the corresponding antibody channel images. All images, excluding the images used for single-cell mask generation, were z-score normalized and used for Barnes–Hut t-SNE (BH t-SNE) [28] and PhenoGraph analysis [29] as implemented in histoCAT. PhenoGraph defines cell clus-

ters based on single-cell mask and marker colocalization (k was set to 20 or 30). A BH t-SNE scatter plot was overlaid with a colored PhenoGraph cluster map. The clusters of the PhenoGraph were exported from histoCAT and further analysed with the SPADE V3.0 tool for Matlab to generate spanning trees of density-normalized events [30]. After defining the single cells with the segmentation mask in histoCAT, the z-score normalized images were exported and used for a FACS-like analysis in FlowJo (version 10.8.1). To investigate the relationship between clusters, neighborhood analysis under standard conditions as implemented in histoCAT was used [31]. The gained result was a score between 0 and 100 for all clusters which was imported in Cytoscape (version 3.8.2) to generate neighborhood trees [32].

2.5. Data Analysis and Statistics

All data are presented as mean ± SEM. Determination of statistically significant difference in all experiments including was conducted with one-way analysis of variance (ANOVA) followed by post hoc Bonferroni correction using GraphPad Prism. 7. For in vitro experiments comparing only two groups, Student's *t*-test was carried out with Welch's correction. A p value of <0.05 was considered statistically significant.

3. Results

3.1. Long-Term Recovery from Stroke

Using a recently established protocol for murine post-stroke care, we were able to achieve full recovery in 76% of the mice in the tMCAO model [22,33]. The mice undergoing tMCAO showed a weight loss of up to 20% after stroke induction whereby the weight loss reached the nadir at day 5. From day 6 onward, weight either stabilized or started to recover (Figure 1A). tMCAO-induced focal neurological or systemic behavioral deficits were measured using the experimental stroke scale (ESSf) [22]. The ESSf score was maximal after 1 day post-stroke and receded completely until day 28 post-stroke (Figure 1B).

To investigate the time course of neovascularization and immune cell recruitment in the tMCAO model, we used the MELC technology for multiple sequential immunohistochemistry. The MELC technology is an automated system, allowing the imaging of an unrestricted number of directly labelled antibodies on the same tissue sample. Overall, 26 antibodies were used to image vessels, neurons, glia cells and immune cells (Supplementary Table S1). Since the cellular and immunological responses in the stroke area are expected to undergo changes between stroke induction and full recovery, we tested the expression of these markers at times, which define the acute (day 1, 3 post-stroke), subacute (day 7) and the recovery phase (day 14) as well as day 28 where full recovery was achieved according to bodyweight and ESSf scores.

In a first step, brain slices were stained with either cresyl violet or hematoxylin/eosin stain to define stroke areas. Cresyl violet and hematoxylin/eosin staining showed a dramatic cellular loss in the right hemisphere starting 1 day after stroke; thereafter, the affected area decreased significantly over time towards a defined subpial cortical region (Figure 2A). Twenty-eight days after stroke induction, this region showed intense nuclear staining but only light cytoplasmic staining (Figure 2A). Surprisingly, a striking structural reorganization of the peri-infarct area including partial repopulation by neurons seemed to occur (Figure 2B). Immunofluorescent staining for GFAP confirmed the formation of a wide astroglial scar surrounding the ischemic core at the border to the peri-infarct area (Figure 2C), showing a strict compartmentalization of the ischemic hemisphere during long-term observation after tMCAO.

In accordance with previous reports, the ischemic area was defined by the absence of neurons and low expression of MAP2 (i.e., day 3–14 after stroke) [34,35] (Figure 2D). Thus, in the following experiments, the combined information from histological and immunohistochemical staining for neurons (NeuN) and the microtubule-associated protein 2 (MAP2) [34,35] was used to define the border of the stroke-affected area, which were chosen for the MELC analysis (Figure 2D).

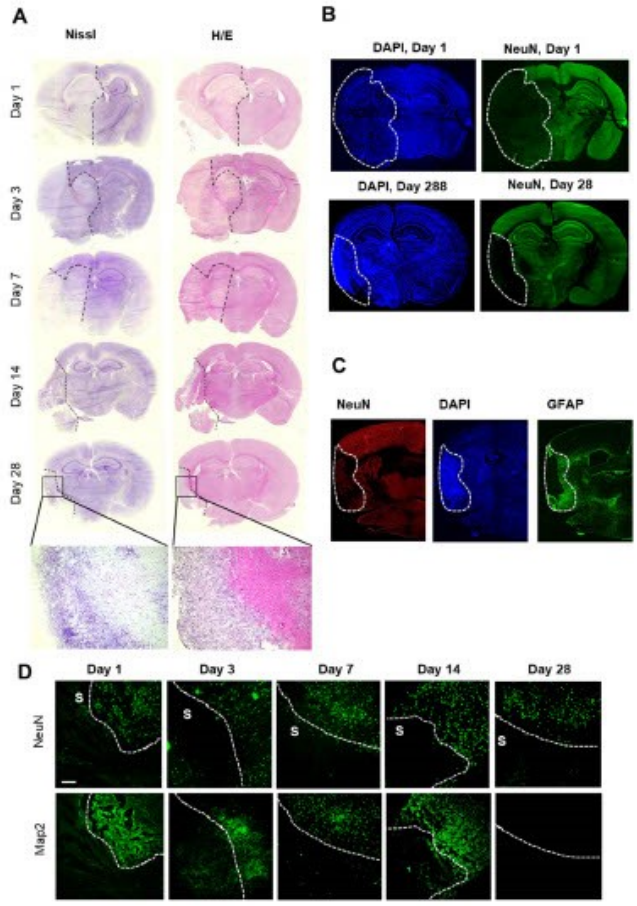

Figure 2. Histochemical and immunohistochemical analyses of the stroke area. (**A**) Nissl- and H/E-staining of brains at the indicated times after stroke induction. The black dashed lines depict regions with severe cell loss. (**B**) Immunohistochemical staining for nuclei (DAPI) and neurons (NeuN). The white lines depict areas with severe neuronal loss. (**C**) Immunohistochemical staining for nuclei (DAPI), astrocytes (GFAP) and neurons (NeuN). The white dotted lines depict the area with severe neuronal loss (ischemic core). (**D**) Immunohistochemical staining of areas at the border between stroke (S) and unaffected tissue for MAP2 and NeuN. The white dotted lines depict the border between stroke and unaffected tissue. The white bar represents 100 µm.

3.2. Temporal and Spatial Patterns of Neoangiogenesis during Stroke Recovery

To determine neovascularization, we analyzed the expression of $CD31^+/CD34^+$ vessels over the course of 28 days in the stroke area using the MELC technology. The fields of vision for MELC analyses were chosen at the border of the stroke area to compare vascularization in the ischemic core and peri-infarct area. For quantitative assessment of $CD31^+/CD34^+$ endothelial tip cells, we used a segmentation mask to extract single-cell data from images including abundances of all measured markers and the microenvironment of each cell such as cell neighbors and cell crowding. This information was compiled into a flow cytometry standard format (.fcs) file for further analysis, which showed a strong upregulation of $CD31^+/CD34^+$ endothelial cells starting at day 14 after stroke induction

(Figure 3A,B). Interestingly, at day 28, the granulomatous, subpially localized cortical remnants of the ischemic core exhibited an especially high amount of neovascularization and is in the following referred to as "ischemic core area of neovascularization" (IC-ANV; Figure 3A,B). Subsequent analysis using tSNE maps as a multi-dimensional reduction tool also showed a high amount of non-endothelial stem cells ($CD31^-/CD34^+$) in the ischemic core regions, apart from the $CD31^+/CD34^+$-populated IC-ANV (Figure 3C). The identification of cell subpopulations and cell transitions using spanning-tree progression analysis of density-normalized events (SPADE) confirmed the increased presence of the $CD31^+/CD34^+$ population in the IC-ANV as compared to the surrounding ischemic core (Figure 3D). Thus, so far, the data show that angiogenesis, as defined by the occurrence of $CD31^+/CD34^+$ endothelial tip cells, starts in the areas affected by the stroke 14 days after induction. Twenty-eight days post-ischemia, an especially strong neovascularisation is observed in the subpial cortical area, which might be due to a massive outgrowth of leptomeningeal vessels.

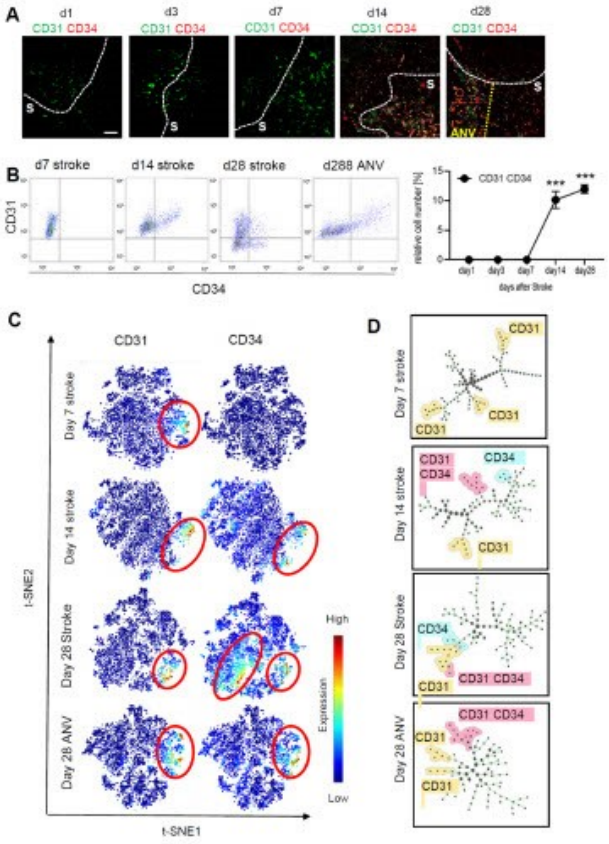

Figure 3. Analysis of neoangiogenesis over time of the stroke area. (**A**) Representative MELC images showing CD31 and CD34 staining in healthy tissue, stroke area (S) and the ischemic core area of neovascularization (IC-ANV) at the indicated times. The white bar represents 100 µm. (**B**) Quantitative assessment of $CD31^+/CD34^+$ endothelial cells based on the MELC images using flow cytometry standard format in the ischemic core and IC-ANV. Data are shown as mean ± S.E.M (n = 4). One-way ANOVA/Bonferroni *** $p < 0.001$. (**C**) tSNE maps with highlighted CD31 and CD34 expression at the indicated times. (**D**) Identification of cell subpopulations and cell transitions using SPADE analysis at the indicated times in the ischemic core and IC-ANV.

3.3. Temporal and Spatial Patterns of Immune Cell Recruitment

Since we observed an increased cell density in the IC-ANV and it has been shown that several immune cell types, such as macrophages and neutrophils, can induce or support post-stroke angiogenesis [36], we investigated the recruitment of immune cells to the ischemic core and especially their presence in the IC-ANV. Therefore, we performed MELC runs using antibodies to identify endothelial cells, microglia, monocyte-derived macrophages, dendritic cells, neutrophils, and various T-cell subtypes (Supplemental Table S1). We found that until day 7 post-stroke, only microglia (F4-80$^+$/Ly6C$^-$/Iba1$^-$) were detectable in the ischemic core (Figure 4A–C). However, starting at day 14 post-stroke, dendritic cells, T-cells and Iba1-expressing microglia also appeared in the stroke-affected region (Figure 4D). The number of neurons decreased rapidly after stroke induction (Figure 4B,D), while NG2-positve cells (probably oligodendrocyte precursor cells (OPCs) and pericytes) remained relatively stable over time (Figure 4B,D).

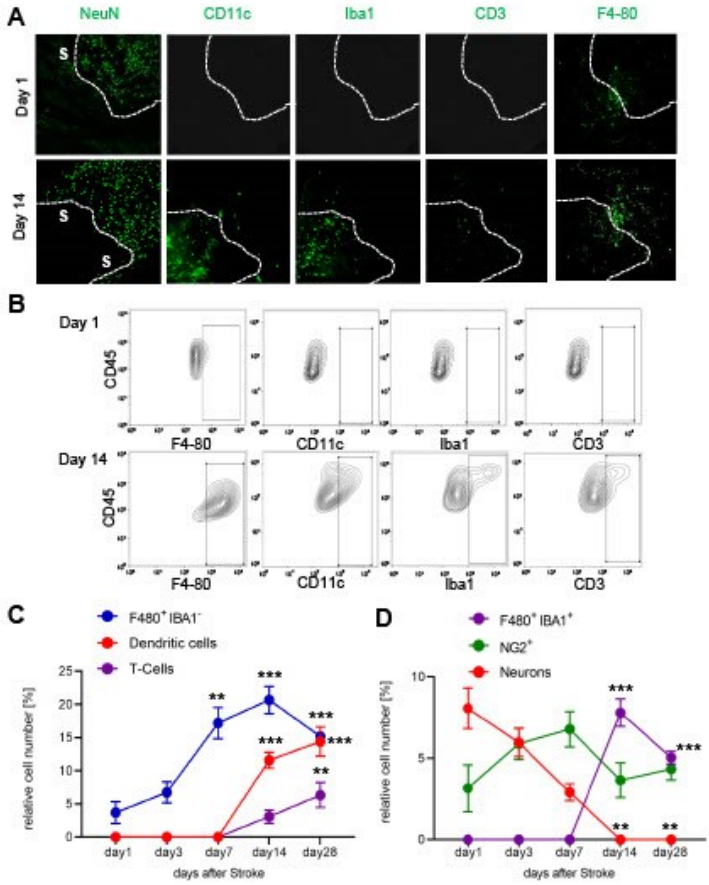

Figure 4. Analysis of immune cell recruitment to the stroke area. (**A**) Representative MELC images showing stroke-affected (S) and unaffected areas at day 1 and 14 after stroke induction. The white lines depict the borders between the two areas. The white bar represents 100 µm. (**B–D**) Quantitative analysis of immune cells based on the MELC images using flow cytometry standard format in the stroke-affected regions. Data are shown as mean ± S.E.M. (n = 4). One-way ANOVA/Bonferroni ** $p < 0.01$; *** $p < 0.001$.

Since we found that the subpial cortical IC-ANV showed a higher cell density as compared to the surrounding ischemic area (Figure 2B), in the next step, we investigated whether or not immune cell recruitment is increased in this area. Quantitative analysis of the MELC data confirmed that the number of $CD31^+/CD34^+$ endothelial tip cells was significantly increased in the IC-ANV as compared to neighboring stroke-affected areas, mainly comprising the astroglial scar (Figure 5A,B). In regard to the number of immune cells, we found that dendritic cells, Iba1-negative microglia, and T-cells showed a roughly twofold increase in the IC-ANV as compared to neighboring stroke-affected areas (Figure 5A,B). In contrast, the number of $NG2^+$ cells and pericytes and Iba1-positive microglia did not differ between both regions (Figure 5A,B).

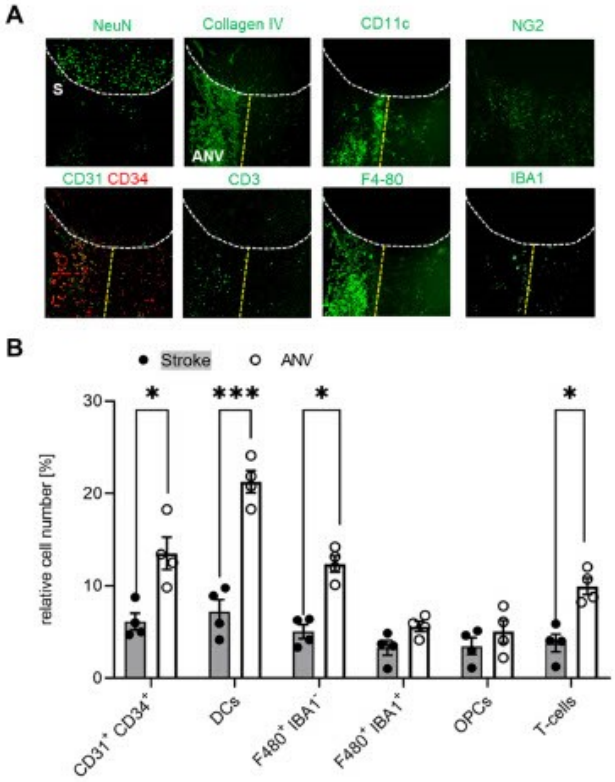

Figure 5. Localized differences of the immune cell distribution in the stroke-affected region. (**A**) Representative MELC images of different immune cells in unaffected and stroke-affected areas (S) as well as IC-ANV 28 days after stroke induction. White dotted lines depict the borders between the three areas. The white bar represents 100 µm. (**B**) Quantitative analysis of immune cells based on the MELC images using flow cytometry standard format in the ischemic core and IC-ANV. Data are shown as mean ± S.E.M (n = 4). Two tailed Student's *t*-test * $p < 0.05$; *** $p < 0.001$.

To study which of these cell types are putative interaction partners of $CD31^+/CD34^+$ endothelial tip cells and could influence angiogenesis, we aimed to determine the cellular neighborhood of these cells. Therefore, we performed a neighborhood analysis [31], which aims to identify cell types neighboring the $CD31^+/CD34^+$ endothelial cells more often, as expected for a random distribution. The scores received by the neighborhood analysis were then plotted using Cytoscape software to visualize the data as neighbor-

hood trees (Figure 6A). The neighborhood analysis showed that dendritic cells, T-cells, and NG2-positive cells, which most likely represent pericytes, were direct neighbors of $CD31^+/CD34^+$ endothelial tip cells, while microglia and astrocytes were more rarely in the neighborhood of the endothelial tip cells (Figure 6A). The T-cell population consisted of $CD3^+/CD4^+/CD27^+/CD8^-$ /T-$bet^-/ROR\gamma t^-$ expressing T-cells (Figure 6B) and the dendritic cells $CD11c^+/F4\ 80^-$ expressing cells (Figure 6C). Taken together, the data show an accumulation of immune cells in the IC-ANV including dendritic cells and CD4 T-cells, which neighbor the $CD31^+/CD34^+$ endothelial tip cells and therefore might support post-stroke angiogenesis.

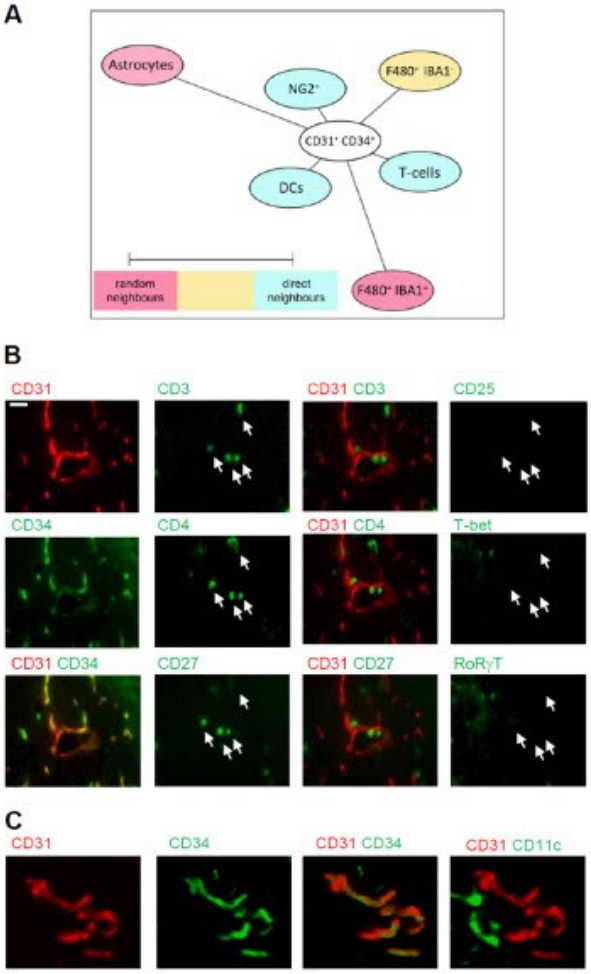

Figure 6. Cellular neighborhood of $CD31^+/CD34^+$ endothelial cells in the IC-ANV. (**A**) Network visualization using Cytoscape of the cellular neighborhood of $CD31^+/CD34^+$ endothelial cells in the IC-ANV 28 days after stroke induction. The distance between $CD31^+/CD34^+$ cells and the other cell types in the visualization represents the statistical probability of being direct neighbors. (**B**,**C**) Representative MELC images showing T-cells (panel (**B**)) and dendritic cells (panel (**C**)) in the neighborhood of $CD31^+/CD34^+$ endothelial cells in the IC-ANV at the indicated times. The white bar represents 10 µm.

4. Discussion

This study explored the spatio-temporal dynamics of post-stroke angiogenesis within the ischemic core after experimental stroke. We show a clear and reproducible compartmentalization of the affected brain tissue into (a) the peri-infarct area, which is separated by (b) a broad astroglial scar from (c) the ischemic core (Figure 7). In the context of chronic remodeling, the ischemic core transforms from the cell-deprived leftovers of sudden and broad cell death to (d) an immunological active zone at the subpial periphery ("ischemic core area of neovascularization/IC-ANV"). A strong vascular reorganization occurred starting 14 days after ischemia, which exceeded mere *arteriogenesis* by sprouting *angiogenesis* within the ischemic core. Importantly, our study shows for the first time that in addition to the peri-infarct area, there is strong vasculo-immunological activity within the infarct core. We therefore postulate that the post-ischemic parenchyma is subjected to transformative processes on both sides of the astroglial scar.

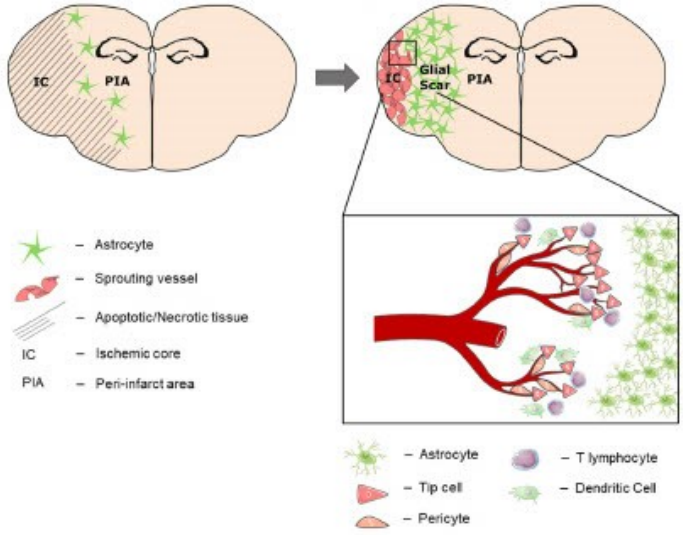

Figure 7. Tissue compartmentalization 28 days after stroke. During post-stroke recovery, the astroglial scar separates the affected hemisphere into the peri-infarcted area (PIA) and the ischemic core (IC). Over time, neural regeneration occurs within the PIA, which expands towards the cortical periphery as the IC shrinks. At the subpial cortex within the IC, another region of immune cell infiltration and neovascularization (IC-ANV) occurs in the late stage of post-stroke recovery.

In this context, the striking regenerative potential of the peri-infarct area in mice becomes apparent, which goes along with comprehensive neural repopulation of the post-ischemic hippocampus as well as the surrounding peri-infarcted parenchyma outside the astroglial scar. This correlates well with complete normalization of the animals' clinical neurological status and indicates a remarkable capacity for adult neurogenesis in the rodent brain. Artificial selection of mildly affected animals at late post-stroke stages was ruled-out in our study due to (1) the utilization of an intensive post-stroke care protocol. At this, we achieved a mortality rate of 26%, which reflects the one of patients facing a severe stroke of the anterior cerebral circulation [37] and reduced mortality bias to the model-specific minimum. (2) By subjecting the animals to regular clinical scoring, we verified that the study population was homogenous concerning their neurological deficits. Additionally, the weight-loss curve did not show sudden "pseudo improvement" after examination days 1, 3, 7 or 14, which would retrospectively hint at selective removal of severely affected animals. (3) All mice used for this study showed cortical infarction, which was proven by

cresyl violet and MAP2 staining, while at later timepoints, subcortical regions appeared largely intact. In the case of short-term or imperfect arterial occlusion, tMCAO is known to lead to subcortical infarctions, typically sparing the peripheral cortex [38,39]. Taken together, we can exclude selection bias towards smaller infarct sizes at later examination timepoints as an alternative explanation for the high density of neurons in the chronic stage of post-stroke regeneration.

Apart from this, a high degree of endothelial-cell proliferative activity developed within the ischemic cortex at late stages of post-stroke recovery. This IC-ANV was completely surrounded by the astroglial scar and was therefore clearly separated from the peri-infarct area. By immunohistochemical examination, we identified several subgroups of endothelial cells ranging from endothelial progenitor cells (EPCs) over $CD31^+/CD34^+$ tip cells to $CD31^+/CD34^-$ mature endothelial cells organized in clear tubular formations, hinting at the delayed induction of angiogenesis in this distinct zone within the IC. As the expected acute leptomeningeal *arteriogenesis*, defined as the activation of leptomeningeal collaterals, is rather dominated by the action of monocytes [40] and circulating $CD31^+/CD34^+$ stem cells would not integrate into the vessel wall as seen here [41], we postulate that this represents an additional *angiogenetic* potential of the leptomeningeal vasculature in the regenerative phase after stroke.

Differing from previous reports, we did not observe neural regeneration accompanying the *angiogenesis* in the IC-ANV, which might be due to the distance from the neural stem cell niche in the SVZ and the separation by the astroglial scar. In contrast to the peri-infarct area, the IC-ANV seems to condensate over time and might resolve completely at later timepoints in mice. Thus, the IC-ANV might represent a site of removal of necrotic tissue rather than regeneration of surviving tissue, whereas the scar serves as a separative seal between those two compartments. In this light, current attempts to modulate astrocyte polarization after stroke [42,43] should be handled carefully as a premature breakup of the compartmented structure might lead to the release of noxious agents towards the preserved brain tissue.

The assumingly leptomeningeal origin of the sprouting capillaries is interesting in that these vessels differ from the central cerebral vasculature, e.g., by the lack of an external elastic lamina [44] and by being equipped with a special blood–leptomeningeal barrier (BLMB) [45]. In contrast to the blood–brain barrier (BBB), it is not composed of a multitude of neurovascular cells but consists of a mono-cellular endothelium of regionally varying permeability [46], which seems to be a critical access point for inflammatory cells to the brain [47,48]. In this regard, it has been recently reported that before invasion of the ischemic parenchyma, immune cells aggregate within the leptomeningeal compartment adjacent to as well as inside the perivascular spaces within the subpial ischemic cortex [49,50]. Moreover, it has been shown that these invading cells access the meninges preferentially by direct vascular channels from the skull bone marrow [51]. Furthermore, there is some evidence that immune cell infiltration via the BLMB could be specifically inhibited targeting certain adhesion molecules [52].

In principle, the infiltrating immune cell populations identified by MELC analysis within the IC-ANV match previous reports in temporal dynamics and quantity [53,54]. Overall, the infiltration process within the IC-ANV seems somewhat delayed over those preceding observations; however, these studies usually refer to the peri-infarct area or to the whole ischemic hemisphere. Nevertheless, we assume the same immune–vascular crosstalk as the basis for the angiogenic processes within the IC-ANV, as has been reported for other sites of vascular remodeling [55] as neighborhood analysis revealed the close proximity of dendritic cells, T lymphocytes, and pericytes to the newly spouted vessels while glial cells such as astrocytes and microglia were more distant. An overlap of the tip-cell-associated $CD31^+/CD34^+$ co-expression with infiltrating or intravascular hematopoietic stem cells was not observed in the IC-ANV since $CD31^-/CD34^+$ were basically absent in this area.

One limitation of our study is the restricted field of view, which does not allow imaging of the complete ischemic hemisphere by which particular regional alterations

might have gone unnoticed. Moreover, we can only assume the leptomeningeal origin of angiogenesis within the IC-AVN due to its strictly subpial localization. Further studies are required to characterize this vascular compartment and to identify potential therapeutic targets, e.g., for differential immunomodulatory, cytoprotective or pro-angiogenic treatment strategies. For instance, acceleration of the post-ischemic clearing processes could create a secure time window for glial-focused therapeutic strategies, which might expand the regenerative potential of the peri-infarct area towards the ischemic core. On the other hand, cytoprotective agents such as the PSD-95 modulator Nerinetide, which is currently under clinical investigation in the context of large vessel occlusion with reperfusion, might exert higher effects when delivered specifically to the site of action outside the astroglial scar.

In conclusion, we assume that in the course of chronic post-stroke regeneration, a distinct process of neovascularization originating from the leptomeningeal vasculature plays a critical role for structural and functional recovery. Further insights into the compartment-specific infiltration and action of immune cells might allow tailor-made drug design in the future to enhance either regenerative or clearance processes within the affected hemisphere.

Supplementary Materials: The following supporting information can be downloaded at: https://www.mdpi.com/article/10.3390/cells11101659/s1, Table S1: Antibodies used for MELC analyses.

Author Contributions: R.I.K., L.J. and R.V. performed in vivo experiments. A.K. and K.S. performed MELC runs, A.K. and T.J.S. performed MELC data analysis. W.P. and R.I.K. designed in vivo experiments. K.S. and R.I.K. wrote the paper. All authors have read and agreed to the published version of the manuscript.

Funding: This work was supported by the DFG grants SFB1039 (TP A08 and B08) SCHO817/3-3, GRK2336 (TP07), Cardio-Pulmonary Institute (CPI), EXC 2026, Project ID: 390649896 and the LOEWE initiative ACLF-I and the Fraunhofer Cluster of Excellence for Immune-Mediated Diseases (CIMD), Frankfurt/Main, Germany.

Institutional Review Board Statement: All animals involved in the presented experiments were approved by the local Ethics Committees for Animal Research (Darmstadt) under the permit number FU/1182. Experiments were performed in accordance with the German Protection of Animals Act and the guidelines for care and use of laboratory animals by the local committee (Regierungspräsidium Darmstadt).

Informed Consent Statement: Not applicable.

Conflicts of Interest: The authors declare no conflict of interest.

References

1. Xu, S.; Lu, J.; Shao, A.; Zhang, J.H.; Zhang, J. Glial Cells: Role of the Immune Response in Ischemic Stroke. *Front. Immunol.* **2020**, *11*, 294. [CrossRef] [PubMed]
2. del Zoppo, G.J.; Frankowski, H.; Gu, Y.-H.; Osada, T.; Kanazawa, M.; Milner, R.; Wang, X.; Hosomi, N.; Mabuchi, T.; Koziol, J.A. Microglial cell activation is a source of metalloproteinase generation during hemorrhagic transformation. *J. Cereb. Blood Flow Metab.* **2012**, *32*, 919–932. [CrossRef] [PubMed]
3. Hayakawa, K.; Nakano, T.; Irie, K.; Higuchi, S.; Fujioka, M.; Orito, K.; Iwasaki, K.; Jin, G.; Lo, E.H.; Mishima, K.; et al. Inhibition of reactive astrocytes with fluorocitrate retards neurovascular remodeling and recovery after focal cerebral ischemia in mice. *J. Cereb. Blood Flow Metab.* **2010**, *30*, 871–882. [CrossRef] [PubMed]
4. Brunkhorst, R.; Kanaan, N.; Koch, A.; Ferreirós, N.; Mirceska, A.; Zeiner, P.; Mittelbronn, M.; Derouiche, A.; Steinmetz, H.; Foerch, C.; et al. FTY720 treatment in the convalescence period improves functional recovery and reduces reactive astrogliosis in photothrombotic stroke. *PLoS ONE* **2013**, *8*, e70124. [CrossRef]
5. Astrup, J.; Symon, L.; Branston, N.M.; Lassen, N.A. Cortical evoked potential and extracellular K^+ and H^+ at critical levels of brain ischemia. *Stroke* **1977**, *8*, 51–57. [CrossRef]
6. Marti, H.J.; Bernaudin, M.; Bellail, A.; Schoch, H.; Euler, M.; Petit, E.; Risau, W. Hypoxia-induced vascular endothelial growth factor expression precedes neovascularization after cerebral ischemia. *Am. J. Pathol.* **2000**, *156*, 965–976. [CrossRef]
7. Ratajska, A.; Jankowska-Steifer, E.; Czarnowska, E.; Olkowski, R.; Gula, G.; Niderla-Bielińska, J.; Flaht-Zabost, A.; Jasińska, A. Vasculogenesis and Its Cellular Therapeutic Applications. *Cells Tissues Organs* **2017**, *203*, 141–152. [CrossRef]
8. van Oostrom, M.C.; van Oostrom, O.; Quax, P.H.A.; Verhaar, M.C.; Hoefer, I.E. Insights into mechanisms behind arteriogenesis: What does the future hold? *J. Leukoc. Biol.* **2008**, *84*, 1379–1391. [CrossRef]

9. Yang, Y.; Torbey, M.T. Angiogenesis and Blood-Brain Barrier Permeability in Vascular Remodeling after Stroke. *Curr. Neuropharmacol.* **2020**, *18*, 1250–1265. [CrossRef]
10. Sidney, L.E.; Branch, M.J.; Dunphy, S.E.; Dua, H.S.; Hopkinson, A. Concise review: Evidence for CD34 as a common marker for diverse progenitors. *Stem Cells* **2014**, *32*, 1380–1389. [CrossRef]
11. Yana, I.; Sagara, H.; Takaki, S.; Takatsu, K.; Nakamura, K.; Nakao, K.; Katsuki, M.; Taniguchi, S.; Aoki, T.; Sato, H.; et al. Crosstalk between neovessels and mural cells directs the site-specific expression of MT1-MMP to endothelial tip cells. *J. Cell Sci.* **2007**, *120*, 1607–1614. [CrossRef]
12. Kamei, M.; Saunders, W.B.; Bayless, K.J.; Dye, L.; Davis, G.E.; Weinstein, B.M. Endothelial tubes assemble from intracellular vacuoles in vivo. *Nature* **2006**, *442*, 453–456. [CrossRef]
13. Fantin, A.; Vieira, J.M.; Gestri, G.; Denti, L.; Schwarz, Q.; Prykhozhij, S.; Peri, F.; Wilson, S.W.; Ruhrberg, C. Tissue macrophages act as cellular chaperones for vascular anastomosis downstream of VEGF-mediated endothelial tip cell induction. *Blood* **2010**, *116*, 829–840. [CrossRef]
14. Hellström, M.; Gerhardt, H.; Kalén, M.; Li, X.; Eriksson, U.; Wolburg, H.; Betsholtz, C. Lack of pericytes leads to endothelial hyperplasia and abnormal vascular morphogenesis. *J. Cell Biol.* **2001**, *153*, 543–553. [CrossRef]
15. Yu, S.W.; Friedman, B.; Cheng, Q.; Lyden, P.D. Stroke-evoked angiogenesis results in a transient population of microvessels. *J. Cereb. Blood Flow Metab.* **2007**, *27*, 755–763. [CrossRef]
16. Durán-Laforet, V.; Fernández-López, D.; García-Culebras, A.; González-Hijón, J.; Moraga, A.; Palma-Tortosa, S.; García-Yébenes, I.; Vega-Pérez, A.; Lizasoain, I.; Moro, M.Á. Delayed Effects of Acute Reperfusion on Vascular Remodeling and Late-Phase Functional Recovery After Stroke. *Front. Neurosci.* **2019**, *13*, 767. [CrossRef]
17. Li, Q.; Ford, M.C.; Lavik, E.B.; Madri, J.A. Modeling the neurovascular niche: VEGF- and BDNF-mediated cross-talk between neural stem cells and endothelial cells: An in vitro study. *J. Neurosci. Res.* **2006**, *84*, 1656–1668. [CrossRef]
18. Fujioka, T.; Kaneko, N.; Sawamoto, K. Blood vessels as a scaffold for neuronal migration. *Neurochem. Int.* **2019**, *126*, 69–73. [CrossRef]
19. Hatakeyama, M.; Ninomiya, I.; Kanazawa, M. Angiogenesis and neuronal remodeling after ischemic stroke. *Neural Regen. Res.* **2020**, *15*, 16–19. [CrossRef]
20. Radak, D.; Katsiki, N.; Resanovic, I.; Jovanovic, A.; Sudar-Milovanovic, E.; Zafirovic, S.; Mousad, S.A.; Isenovic, E.R. Apoptosis and Acute Brain Ischemia in Ischemic Stroke. *Curr. Vasc. Pharmacol.* **2017**, *15*, 115–122. [CrossRef]
21. Jovin, T.G.; Yonas, H.; Gebel, J.M.; Kanal, E.; Chang, Y.F.; Grahovac, S.Z.; Goldstein, S.; Wechsler, L.R. The cortical ischemic core and not the consistently present penumbra is a determinant of clinical outcome in acute middle cerebral artery occlusion. *Stroke* **2003**, *34*, 2426–2433. [CrossRef] [PubMed]
22. Lourbopoulos, A.; Mamrak, U.; Roth, S.; Balbi, M.; Shrouder, J.; Liesz, A.; Hellal, F.; Plesnila, N. Inadequate food and water intake determine mortality following stroke in mice. *J. Cereb. Blood Flow Metab.* **2017**, *37*, 2084–2097. [CrossRef] [PubMed]
23. Pfeilschifter, W.; Bohmann, F.; Baumgarten, P.; Mittelbronn, M.; Pfeilschifter, J.; Lindhoff-Last, E.; Steinmetz, H.; Foerch, C. Thrombolysis with recombinant tissue plasminogen activator under dabigatran anticoagulation in experimental stroke. *Ann. Neurol.* **2012**, *71*, 624–633. [CrossRef]
24. Pierre, S.; Scholich, K. Toponomics: Studying protein-protein interactions and protein networks in intact tissue. *Mol. Biosyst.* **2010**, *6*, 641–647. [CrossRef]
25. Pierre, S.; Linke, B.; Suo, J.; Tarighi, N.; Del Turco, D.; Thomas, D.; Ferreiros, N.; Stegner, D.; Frolich, S.; Sisignano, M.; et al. GPVI and Thromboxane Receptor on Platelets Promote Proinflammatory Macrophage Phenotypes during Cutaneous Inflammation. *J. Investig. Dermatol.* **2017**, *137*, 686–695. [CrossRef]
26. Kornstädt, L.; Pierre, S.; Weigert, A.; Ebersberger, S.; Schäufele, T.J.; Kolbinger, A.; Schmid, T.; Cohnen, J.; Thomas, D.; Ferreirós, N.; et al. Bacterial and Fungal Toll-Like Receptor Activation Elicits Type I IFN Responses in Mast Cells. *Front. Immunol.* **2020**, *11*, 607048. [CrossRef]
27. McQuin, C.; Goodman, A.; Chernyshev, V.; Kamentsky, L.; Cimini, B.A.; Karhohs, K.W.; Doan, M.; Ding, L.; Rafelski, S.M.; Thirstrup, D.; et al. CellProfiler 3.0: Next-generation image processing for biology. *PLoS Biol.* **2018**, *16*, e2005970. [CrossRef]
28. Amir, E.D.; Davis, K.L.; Tadmor, M.D.; Simonds, E.F.; Levine, J.H.; Bendall, S.C.; Shenfeld, D.K.; Krishnaswamy, S.; Nolan, G.P.; Pe'er, D. viSNE enables visualization of high dimensional single-cell data and reveals phenotypic heterogeneity of leukemia. *Nat. Biotechnol.* **2013**, *31*, 545–552. [CrossRef]
29. Levine, J.H.; Simonds, E.F.; Bendall, S.C.; Davis, K.L.; Amir, E.D.; Tadmor, M.D.; Litvin, O.; Fienberg, H.G.; Jager, A.; Zunder, E.R.; et al. Data-Driven Phenotypic Dissection of AML Reveals Progenitor-like Cells that Correlate with Prognosis. *Cell* **2015**, *162*, 184–197. [CrossRef]
30. Qiu, P.; Simonds, E.F.; Bendall, S.C.; Gibbs, K.D.J.; Bruggner, R.V.; Linderman, M.D.; Sachs, K.; Nolan, G.P.; Plevritis, S.K. Extracting a cellular hierarchy from high-dimensional cytometry data with SPADE. *Nat. Biotechnol.* **2011**, *29*, 886–891. [CrossRef]
31. Schapiro, D.; Jackson, H.W.; Raghuraman, S.; Fischer, J.R.; Zanotelli, V.R.T.; Schulz, D.; Giesen, C.; Catena, R.; Varga, Z.; Bodenmiller, B. histoCAT: Analysis of cell phenotypes and interactions in multiplex image cytometry data. *Nat. Methods* **2017**, *14*, 873–876. [CrossRef] [PubMed]
32. Otasek, D.; Morris, J.H.; Bouças, J.; Pico, A.R.; Demchak, B. Cytoscape Automation: Empowering workflow-based network analysis. *Genome Biol.* **2019**, *20*, 185. [CrossRef]

33. Kestner, R.-I.; Mayser, F.; Vutukuri, R.; Hansen, L.; Günther, S.; Brunkhorst, R.; Devraj, K.; Pfeilschifter, W. Gene Expression Dynamics at the Neurovascular Unit During Early Regeneration After Cerebral Ischemia/Reperfusion Injury in Mice. *Front. Neurosci.* **2020**, *14*, 280. [CrossRef]
34. Mages, B.; Fuhs, T.; Aleithe, S.; Blietz, A.; Hobusch, C.; Härtig, W.; Schob, S.; Krueger, M.; Michalski, D. The Cytoskeletal Elements MAP2 and NF-L Show Substantial Alterations in Different Stroke Models While Elevated Serum Levels Highlight Especially MAP2 as a Sensitive Biomarker in Stroke Patients. *Mol. Neurobiol.* **2021**, *58*, 4051–4069. [CrossRef]
35. Kharlamov, A.; LaVerde, G.C.; Nemoto, E.M.; Jungreis, C.A.; Yushmanov, V.E.; Jones, S.C.; Boada, F.E. MAP2 immunostaining in thick sections for early ischemic stroke infarct volume in non-human primate brain. *J. Neurosci. Methods* **2009**, *182*, 205–210. [CrossRef]
36. Ma, Y.; Yang, S.; He, Q.; Zhang, D.; Chang, J. The Role of Immune Cells in Post-Stroke Angiogenesis and Neuronal Remodeling: The Known and the Unknown. *Front. Immunol.* **2021**, *12*, 784098. [CrossRef] [PubMed]
37. Karamchandani, R.R.; Rhoten, J.B.; Strong, D.; Chang, B.; Asimos, A.W. Mortality after large artery occlusion acute ischemic stroke. *Sci. Rep.* **2021**, *11*, 10033. [CrossRef] [PubMed]
38. Wakayama, K.; Shimamura, M.; Sata, M.; Sato, N.; Kawakami, K.; Fukuda, H.; Tomimatsu, T.; Ogihara, T.; Morishita, R. Quantitative measurement of neurological deficit after mild (30 min) transient middle cerebral artery occlusion in rats. *Brain Res.* **2007**, *1130*, 181–187. [CrossRef]
39. Chiazza, F.; Pintana, H.; Lietzau, G.; Nyström, T.; Patrone, C.; Darsalia, V. The Stroke-Induced Increase of Somatostatin-Expressing Neurons is Inhibited by Diabetes: A Potential Mechanism at the Basis of Impaired Stroke Recovery. *Cell Mol. Neurobiol.* **2021**, *41*, 591–603. [CrossRef]
40. Sugiyama, Y.; Yagita, Y.; Oyama, N.; Terasaki, Y.; Omura-Matsuoka, E.; Sasaki, T.; Kitagawa, K. Granulocyte colony-stimulating factor enhances arteriogenesis and ameliorates cerebral damage in a mouse model of ischemic stroke. *Stroke* **2011**, *42*, 770–775. [CrossRef]
41. Kinnaird, T.; Stabile, E.; Burnett, M.S.; Lee, C.W.; Barr, S.; Fuchs, S.; Epstein, S.E. Marrow-derived stromal cells express genes encoding a broad spectrum of arteriogenic cytokines and promote in vitro and in vivo arteriogenesis through paracrine mechanisms. *Circ. Res.* **2004**, *94*, 678–685. [CrossRef] [PubMed]
42. Cao, J.; Dong, L.; Luo, J.; Zeng, F.; Hong, Z.; Liu, Y.; Zhao, Y.; Xia, Z.; Zuo, D.; Xu, L.; et al. Supplemental N-3 Polyunsaturated Fatty Acids Limit A1-Specific Astrocyte Polarization via Attenuating Mitochondrial Dysfunction in Ischemic Stroke in Mice. *Oxid. Med. Cell. Longev.* **2021**, *2021*, 5524705. [CrossRef] [PubMed]
43. Zhao, N.; Xu, X.; Jiang, Y.; Gao, J.; Wang, F.; Xu, X.; Wen, Z.; Xie, Y.; Li, J.; Li, R.; et al. Lipocalin-2 may produce damaging effect after cerebral ischemia by inducing astrocytes classical activation. *J. Neuroinflamm.* **2019**, *16*, 168. [CrossRef]
44. Hill, M.A.; Nourian, Z.; Ho, I.-L.; Clifford, P.S.; Martinez-Lemus, L.; Meininger, G.A. Small Artery Elastin Distribution and Architecture-Focus on Three Dimensional Organization. *Microcirculation* **2016**, *23*, 614–620. [CrossRef]
45. Gao, Y.; Whitaker-Dowling, P.; Barmada, M.A.; Basse, P.H.; Bergman, I. Viral infection of implanted meningeal tumors induces antitumor memory T-cells to travel to the brain and eliminate established tumors. *Neuro-Oncology* **2015**, *17*, 536–544. [CrossRef] [PubMed]
46. Mastorakos, P.; McGavern, D. The anatomy and immunology of vasculature in the central nervous system. *Sci. Immunol.* **2019**, *4*, eaav0492. [CrossRef]
47. Perez-de-Puig, I.; Miró-Mur, F.; Ferrer-Ferrer, M.; Gelpi, E.; Pedragosa, J.; Justicia, C.; Urra, X.; Chamorro, A.; Planas, A.M. Neutrophil recruitment to the brain in mouse and human ischemic stroke. *Acta Neuropathol.* **2015**, *129*, 239–257. [CrossRef]
48. Schläger, C.; Körner, H.; Krueger, M.; Vidoli, S.; Haberl, M.; Mielke, D.; Brylla, E.; Issekutz, T.; Cabañas, C.; Nelson, P.J.; et al. Effector T-cell trafficking between the leptomeninges and the cerebrospinal fluid. *Nature* **2016**, *530*, 349–353. [CrossRef]
49. Otxoa-de-Amezaga, A.; Gallizioli, M.; Pedragosa, J.; Justicia, C.; Miró-Mur, F.; Salas-Perdomo, A.; Diaz-Marugan, L.; Gunzer, M.; Planas, A.M. Location of Neutrophils in Different Compartments of the Damaged Mouse Brain After Severe Ischemia/Reperfusion. *Stroke* **2019**, *50*, 1548–1557. [CrossRef]
50. Houze, J.B.; Zhu, L.; Sun, Y.; Akerman, M.; Qiu, W.; Zhang, A.J.; Sharma, R.; Schmitt, M.; Wang, Y.; Liu, J.; et al. AMG 837: A potent, orally bioavailable GPR40 agonist. *Bioorg. Med. Chem. Lett.* **2012**, *22*, 1267–1270. [CrossRef]
51. Herisson, F.; Frodermann, V.; Courties, G.; Rohde, D.; Sun, Y.; Vandoorne, K.; Wojtkiewicz, G.R.; Masson, G.S.; Vinegoni, C.; Kim, J.; et al. Direct vascular channels connect skull bone marrow and the brain surface enabling myeloid cell migration. *Nat. Neurosci.* **2018**, *21*, 1209–1217. [CrossRef] [PubMed]
52. Michel, L.; Grasmuck, C.; Charabati, M.; Lécuyer, M.-A.; Zandee, S.; Dhaeze, T.; Alvarez, J.I.; Li, R.; Larouche, S.; Bourbonnière, L.; et al. Activated leukocyte cell adhesion molecule regulates B lymphocyte migration across central nervous system barriers. *Sci. Transl. Med.* **2019**, *11*, eaaw0475. [CrossRef] [PubMed]
53. Gelderblom, M.; Leypoldt, F.; Steinbach, K.; Behrens, D.; Choe, C.-U.; Siler, D.A.; Arumugam, T.V.; Orthey, E.; Gerloff, C.; Tolosa, E.; et al. Temporal and spatial dynamics of cerebral immune cell accumulation in stroke. *Stroke* **2009**, *40*, 1849–1857. [CrossRef] [PubMed]
54. Iadecola, C.; Buckwalter, M.S.; Anrather, J. Immune responses to stroke: Mechanisms, modulation, and therapeutic potential. *J. Clin. Investig.* **2020**, *130*, 2777–2788. [CrossRef]
55. Ribatti, D.; Crivellato, E. Immune cells and angiogenesis. *J. Cell. Mol. Med.* **2009**, *13*, 2822–2833. [CrossRef]

6.3 Contribution to publications

As the first author, I was involved in all data collection for the Publication Kolbinger et al. 2023. I performed the FACS analyses, ELISA, and multiplex cytokine measurements, did the behavior experiments with the animals, and executed the MELC analyses after collecting and preparing the necessary tissues. Together with Tim Schäufele and Joschua Friedel, I established the used antibody panels for the MELC and the FACS analysis and developed the bioinformatic pipeline. Using this pipeline, I analyzed all data generated with the MELC method. Together with Klaus Scholich, I planned the experiments and chose the used material and methods.

Roxane Kestner, Lara Jenico, and Rajkumar Vutukurind Rajkumar Vutukuri performed the in-vivo experiments for the Publication Kolbinger, Kestner et al. 2022 and prepared the tissue samples for the MELC. I executed the MELC experiments with Klaus Scholich and analyzed the generated data sets with the developed bioinformatical pipeline.

For both publications, I interpreted and graphically presented the results and was involved in writing the original draft of the submitted manuscripts, including figures and supplements, and approved the final versions. Additionally, I was responsible for the modifications and the data collection during the revision process.

References

1. Medzhitov R. Origin and physiological roles of inflammation. *Nature*. 2008;454(7203):428-435. doi:10.1038/nature07201
2. Varela ML, Mogildea M, Moreno I, Lopes A. Acute Inflammation and Metabolism. *Inflammation*. 2018;41(4):1115-1127. doi:10.1007/s10753-018-0739-1
3. Isobe Y, Kato T, Arita M. Emerging Roles of Eosinophils and Eosinophil-Derived Lipid Mediators in the Resolution of Inflammation. *Front Immunol*. 2012;3:270. doi:10.3389/fimmu.2012.00270
4. Ashley NT, Weil ZM, Nelson RJ. Inflammation: Mechanisms, Costs, and Natural Variation. *Annu Rev Ecol Evol Syst*. 2012;43(1):385-406. doi:10.1146/annurev-ecolsys-040212-092530
5. Feghali CA, Wright TM. Cytokines in acute and chronic inflammation. *Front Biosci J Virtual Libr*. 1997;2:d12-26. doi:10.2741/a171
6. Walsh D, McCarthy J, O'Driscoll C, Melgar S. Pattern recognition receptors--molecular orchestrators of inflammation in inflammatory bowel disease. *Cytokine Growth Factor Rev*. 2013;24(2):91-104. doi:10.1016/j.cytogfr.2012.09.003
7. Barton GM. A calculated response: control of inflammation by the innate immune system. *J Clin Invest*. 2008;118(2):413-420. doi:10.1172/JCI34431
8. Nathan C. Points of control in inflammation. *Nature*. 2002;420(6917):846-852. doi:10.1038/nature01320
9. Serhan CN, Savill J. Resolution of inflammation: the beginning programs the end. *Nat Immunol*. 2005;6(12):1191-1197. doi:10.1038/ni1276
10. Sansbury BE, Spite M. Resolution of Acute Inflammation and the Role of Resolvins in Immunity, Thrombosis, and Vascular Biology. *Circ Res*. 2016;119(1):113-130. doi:10.1161/CIRCRESAHA.116.307308
11. Buckley CD, Gilroy DW, Serhan CN, Stockinger B, Tak PP. The resolution of inflammation. *Nat Rev Immunol*. 2013;13(1):59-66. doi:10.1038/nri3362
12. Feehan KT, Gilroy DW. Is Resolution the End of Inflammation? *Trends Mol Med*. 2019;25(3):198-214. doi:10.1016/j.molmed.2019.01.006
13. van den Berg JM, Weyer S, Weening JJ, Roos D, Kuijpers TW. Divergent effects of tumor necrosis factor alpha on apoptosis of human neutrophils. *J Leukoc Biol*. 2001;69(3):467-473.
14. Ortega-Gómez A, Perretti M, Soehnlein O. Resolution of inflammation: an integrated view. *EMBO Mol Med*. 2013;5(5):661-674. doi:10.1002/emmm.201202382
15. Dalli J, Norling LV, Renshaw D, Cooper D, Leung KY, Perretti M. Annexin 1 mediates the rapid anti-inflammatory effects of neutrophil-derived microparticles. *Blood*. 2008;112(6):2512-2519. doi:10.1182/blood-2008-02-140533
16. Bournazou I, Pound JD, Duffin R, et al. Apoptotic human cells inhibit migration of granulocytes via release of lactoferrin. *J Clin Invest*. 2009;119(1):20-32. doi:10.1172/JCI36226
17. Fullerton JN, Gilroy DW. Resolution of inflammation: a new therapeutic frontier. *Nat Rev Drug Discov*. 2016;15(8):551-567. doi:10.1038/nrd.2016.39
18. Kourtzelis I, Hajishengallis G, Chavakis T. Phagocytosis of Apoptotic Cells in Resolution of Inflammation. *Front Immunol*. 2020;11. Accessed January 3, 2023. https://www.frontiersin.org/articles/10.3389/fimmu.2020.00553

19. Yao Y, Xu XH, Jin L. Macrophage Polarization in Physiological and Pathological Pregnancy. *Front Immunol*. 2019;10. Accessed January 3, 2023. https://www.frontiersin.org/articles/10.3389/fimmu.2019.00792
20. Patel U, Rajasingh S, Samanta S, Cao T, Dawn B, Rajasingh J. Macrophage polarization in response to epigenetic modifiers during infection and inflammation. *Drug Discov Today*. 2017;22(1):186-193. doi:10.1016/j.drudis.2016.08.006
21. Conaway EA, de Oliveira DC, McInnis CM, Snapper SB, Horwitz BH. Inhibition of Inflammatory Gene Transcription by IL-10 Is Associated with Rapid Suppression of Lipopolysaccharide-Induced Enhancer Activation. *J Immunol*. 2017;198(7):2906-2915. doi:10.4049/jimmunol.1601781
22. Martinez FO, Helming L, Gordon S. Alternative activation of macrophages: an immunologic functional perspective. *Annu Rev Immunol*. 2009;27:451-483. doi:10.1146/annurev.immunol.021908.132532
23. Saclier M, Yacoub-Youssef H, Mackey AL, et al. Differentially activated macrophages orchestrate myogenic precursor cell fate during human skeletal muscle regeneration. *Stem Cells Dayt Ohio*. 2013;31(2):384-396. doi:10.1002/stem.1288
24. Steinbach KH, Schick P, Trepel F, et al. Estimation of kinetic parameters of neutrophilic, eosinophilic, and basophilic granulocytes in human blood. *Blut*. 1979;39(1):27-38. doi:10.1007/BF01008072
25. Klion A. Recent advances in understanding eosinophil biology. *F1000Research*. 2017;6:1084. doi:10.12688/f1000research.11133.1
26. Ramirez GA, Yacoub MR, Ripa M, et al. Eosinophils from Physiology to Disease: A Comprehensive Review. *BioMed Res Int*. 2018;2018:9095275. doi:10.1155/2018/9095275
27. Fulkerson PC, Rothenberg ME. Targeting Eosinophils in Allergy, Inflammation and Beyond. *Nat Rev Drug Discov*. 2013;12(2):10.1038/nrd3838. doi:10.1038/nrd3838
28. Séguéla PE, Iriart X, Acar P, Montaudon M, Roudaut R, Thambo JB. Eosinophilic cardiac disease: Molecular, clinical and imaging aspects. *Arch Cardiovasc Dis*. 2015;108(4):258-268. doi:10.1016/j.acvd.2015.01.006
29. Lee JJ, Jacobsen EA, Ochkur SI, et al. Human versus mouse eosinophils: “that which we call an eosinophil, by any other name would stain as red.” *J Allergy Clin Immunol*. 2012;130(3):572-584. doi:10.1016/j.jaci.2012.07.025
30. Rosenberg HF, Dyer KD, Foster PS. Eosinophils: changing perspectives in health and disease. *Nat Rev Immunol*. 2013;13(1):9-22. doi:10.1038/nri3341
31. Berek C. Eosinophils: important players in humoral immunity. *Clin Exp Immunol*. 2016;183(1):57-64. doi:10.1111/cei.12695
32. Chu VT, Beller A, Rausch S, et al. Eosinophils Promote Generation and Maintenance of Immunoglobulin-A-Expressing Plasma Cells and Contribute to Gut Immune Homeostasis. *Immunity*. 2014;40(4):582-593. doi:10.1016/j.immuni.2014.02.014
33. Bass DA. Behavior of eosinophil leukocytes in acute inflammation. I. Lack of dependence on adrenal function. *J Clin Invest*. 1975;55(6):1229-1236. doi:10.1172/jci108041

34. Valent P, Klion AD, Horny HP, et al. Contemporary consensus proposal on criteria and classification of eosinophilic disorders and related syndromes. *J Allergy Clin Immunol*. 2012;130(3):607-612.e9. doi:10.1016/j.jaci.2012.02.019
35. Roufosse F, Kahn JE, Rothenberg ME, et al. Efficacy and safety of mepolizumab in hypereosinophilic syndrome: A phase III, randomized, placebo-controlled trial. *J Allergy Clin Immunol*. 2020;146(6):1397-1405. doi:10.1016/j.jaci.2020.08.037
36. Diny NL, Rose NR, Čiháková D. Eosinophils in Autoimmune Diseases. *Front Immunol*. 2017;8:484. doi:10.3389/fimmu.2017.00484
37. Sheikh J, Weller PF. Advances in diagnosis and treatment of eosinophilia. *Curr Opin Hematol*. 2009;16(1):3-8. doi:10.1097/MOH.0b013e32831c841f
38. Acharya KR, Ackerman SJ. Eosinophil granule proteins: form and function. *J Biol Chem*. 2014;289(25):17406-17415. doi:10.1074/jbc.R113.546218
39. Erjefält JS, Persson CGA. New Aspects of Degranulation and Fates of Airway Mucosal Eosinophils. *Am J Respir Crit Care Med*. 2000;161(6):2074-2085. doi:10.1164/ajrccm.161.6.9906085
40. Yousefi S, Gold JA, Andina N, et al. Catapult-like release of mitochondrial DNA by eosinophils contributes to antibacterial defense. *Nat Med*. 2008;14(9):949-953. doi:10.1038/nm.1855
41. Svensson L, Wennerås C. Human eosinophils selectively recognize and become activated by bacteria belonging to different taxonomic groups. *Microbes Infect*. 2005;7(4):720-728. doi:10.1016/j.micinf.2005.01.010
42. Spencer LA, Szela CT, Perez SAC, et al. Human eosinophils constitutively express multiple Th1, Th2, and immunoregulatory cytokines that are secreted rapidly and differentially. *J Leukoc Biol*. 2009;85(1):117-123. doi:10.1189/jlb.0108058
43. Galdiero MR, Varricchi G, Seaf M, Marone G, Levi-Schaffer F, Marone G. Bidirectional Mast Cell–Eosinophil Interactions in Inflammatory Disorders and Cancer. *Front Med*. 2017;4:103. doi:10.3389/fmed.2017.00103
44. van Furth R, Cohn ZA, Hirsch JG, Humphrey JH, Spector WG, Langevoort HL. The mononuclear phagocyte system: a new classification of macrophages, monocytes, and their precursor cells. *Bull World Health Organ*. 1972;46(6):845-852.
45. Steinman RM, Cohn ZA. Identification of a novel cell type in peripheral lymphoid organs of mice. I. Morphology, quantitation, tissue distribution. *J Exp Med*. 1973;137(5):1142-1162. doi:10.1084/jem.137.5.1142
46. Varol C, Mildner A, Jung S. Macrophages: Development and Tissue Specialization. *Annu Rev Immunol*. 2015;33(1):643-675. doi:10.1146/annurev-immunol-032414-112220
47. Sica A, Erreni M, Allavena P, Porta C. Macrophage polarization in pathology. *Cell Mol Life Sci CMLS*. 2015;72(21):4111-4126. doi:10.1007/s00018-015-1995-y
48. Epelman S, Lavine KJ, Randolph GJ. Origin and functions of tissue macrophages. *Immunity*. 2014;41(1):21-35. doi:10.1016/j.immuni.2014.06.013
49. Hashimoto D, Chow A, Noizat C, et al. Tissue-resident macrophages self-maintain locally throughout adult life with minimal contribution from circulating monocytes. *Immunity*. 2013;38(4):792-804. doi:10.1016/j.immuni.2013.04.004
50. Davies LC, Jenkins SJ, Allen JE, Taylor PR. Tissue-resident macrophages. *Nat Immunol*. 2013;14(10):986-995. doi:10.1038/ni.2705

51. Ginhoux F, Jung S. Monocytes and macrophages: developmental pathways and tissue homeostasis. *Nat Rev Immunol*. 2014;14(6):392-404. doi:10.1038/nri3671
52. Das A, Sinha M, Datta S, et al. Monocyte and macrophage plasticity in tissue repair and regeneration. *Am J Pathol*. 2015;185(10):2596-2606. doi:10.1016/j.ajpath.2015.06.001
53. Sica A, Mantovani A. Macrophage plasticity and polarization: in vivo veritas. *J Clin Invest*. 2012;122(3):787-795. doi:10.1172/JCI59643
54. Yunna C, Mengru H, Lei W, Weidong C. Macrophage M1/M2 polarization. *Eur J Pharmacol*. 2020;877:173090. doi:10.1016/j.ejphar.2020.173090
55. Biswas SK, Chittezhath M, Shalova IN, Lim JY. Macrophage polarization and plasticity in health and disease. *Immunol Res*. 2012;53(1-3):11-24. doi:10.1007/s12026-012-8291-9
56. Bashir S, Sharma Y, Elahi A, Khan F. Macrophage polarization: the link between inflammation and related diseases. *Inflamm Res Off J Eur Histamine Res Soc Al*. 2016;65(1):1-11. doi:10.1007/s00011-015-0874-1
57. Kurowska-Stolarska M, Stolarski B, Kewin P, et al. IL-33 Amplifies the Polarization of Alternatively Activated Macrophages That Contribute to Airway Inflammation1. *J Immunol*. 2009;183(10):6469-6477. doi:10.4049/jimmunol.0901575
58. Braga TT, Agudelo JSH, Camara NOS. Macrophages During the Fibrotic Process: M2 as Friend and Foe. *Front Immunol*. 2015;6:602. doi:10.3389/fimmu.2015.00602
59. Porta C, Riboldi E, Ippolito A, Sica A. Molecular and epigenetic basis of macrophage polarized activation. *Semin Immunol*. 2015;27(4):237-248. doi:10.1016/j.smim.2015.10.003
60. Jetten N, Verbruggen S, Gijbels MJ, Post MJ, De Winther MPJ, Donners MMPC. Anti-inflammatory M2, but not pro-inflammatory M1 macrophages promote angiogenesis in vivo. *Angiogenesis*. 2014;17(1):109-118. doi:10.1007/s10456-013-9381-6
61. Belgiovine C, D'Incalci M, Allavena P, Frapolli R. Tumor-associated macrophages and anti-tumor therapies: complex links. *Cell Mol Life Sci CMLS*. 2016;73(13):2411-2424. doi:10.1007/s00018-016-2166-5
62. Pérez S, Rius-Pérez S. Macrophage Polarization and Reprogramming in Acute Inflammation: A Redox Perspective. *Antioxidants*. 2022;11(7):1394. doi:10.3390/antiox11071394
63. Amir E ad D, Davis KL, Tadmor MD, et al. viSNE enables visualization of high dimensional single-cell data and reveals phenotypic heterogeneity of leukemia. *Nat Biotechnol*. 2013;31(6):545-552. doi:10.1038/nbt.2594
64. Lin JR, Fallahi-Sichani M, Chen JY, Sorger PK. Cyclic Immunofluorescence (CycIF), A Highly Multiplexed Method for Single-cell Imaging. *Curr Protoc Chem Biol*. 2016;8(4):251-264. doi:10.1002/cpch.14
65. Pang L, Ernst M, Huynh J. Development of a Multiplex Immunohistochemistry Workflow to Investigate the Immune Microenvironment in Mouse Models of Inflammatory Bowel Disease and Colon Cancer. *Int J Mol Sci*. 2021;22(20):11001. doi:10.3390/ijms222011001

66. Elaldi R, Hemon P, Petti L, et al. High Dimensional Imaging Mass Cytometry Panel to Visualize the Tumor Immune Microenvironment Contexture. *Front Immunol*. 2021;12. Accessed May 29, 2023. https://www.frontiersin.org/articles/10.3389/fimmu.2021.666233
67. Bonnekoh B, Pommer AJ, Böckelmann R, Philipsen L, Hofmeister H, Gollnick H. In-situ-topoproteome analysis of cutaneous lymphomas: Perspectives of assistance for dermatohistologic diagnostics by Multi Epitope Ligand Cartography (MELC). *JDDG J Dtsch Dermatol Ges*. 2008;6(12):1038-1051. doi:10.1111/j.1610-0387.2008.06754.x
68. Sheng W, Zhang C, Mohiuddin TM, et al. Multiplex Immunofluorescence: A Powerful Tool in Cancer Immunotherapy. *Int J Mol Sci*. 2023;24(4):3086. doi:10.3390/ijms24043086
69. Black S, Phillips D, Hickey JW, et al. CODEX multiplexed tissue imaging with DNA-conjugated antibodies. *Nat Protoc*. 2021;16(8):3802-3835. doi:10.1038/s41596-021-00556-8
70. Liu CC, McCaffrey EF, Greenwald NF, et al. Multiplexed Ion Beam Imaging: Insights into Pathobiology. *Annu Rev Pathol Mech Dis*. 2022;17(1):403-423. doi:10.1146/annurev-pathmechdis-030321-091459
71. Dixon AR, Bathany C, Tsuei M, White J, Barald KF, Takayama S. Recent developments in multiplexing techniques for immunohistochemistry. *Expert Rev Mol Diagn*. 2015;15(9):1171-1186. doi:10.1586/14737159.2015.1069182
72. Hickey JW, Neumann EK, Radtke AJ, et al. Spatial mapping of protein composition and tissue organization: a primer for multiplexed antibody-based imaging. *Nat Methods*. 2022;19(3):284-295. doi:10.1038/s41592-021-01316-y
73. Schapiro D, Yapp C, Sokolov A, et al. MITI minimum information guidelines for highly multiplexed tissue images. *Nat Methods*. 2022;19(3):262-267. doi:10.1038/s41592-022-01415-4
74. Schapiro D, Jackson HW, Raghuraman S, et al. histoCAT: analysis of cell phenotypes and interactions in multiplex image cytometry data. *Nat Methods*. 2017;14(9):873-876. doi:10.1038/nmeth.4391
75. Dey N. Uneven illumination correction of digital images: A survey of the state-of-the-art. *Optik*. 2019;183:483-495. doi:10.1016/j.ijleo.2019.02.118
76. Stirling DR, Swain-Bowden MJ, Lucas AM, Carpenter AE, Cimini BA, Goodman A. CellProfiler 4: improvements in speed, utility and usability. *BMC Bioinformatics*. 2021;22(1):433. doi:10.1186/s12859-021-04344-9
77. Wählby C, Sintorn IM, Erlandsson F, Borgefors G, Bengtsson E. Combining intensity, edge and shape information for 2D and 3D segmentation of cell nuclei in tissue sections. *J Microsc*. 2004;215(1):67-76. doi:10.1111/j.0022-2720.2004.01338.x
78. Berg S, Kutra D, Kroeger T, et al. ilastik: interactive machine learning for (bio)image analysis. *Nat Methods*. 2019;16(12):1226-1232. doi:10.1038/s41592-019-0582-9
79. Valen DAV, Kudo T, Lane KM, et al. Deep Learning Automates the Quantitative Analysis of Individual Cells in Live-Cell Imaging Experiments. *PLOS Comput Biol*. 2016;12(11):e1005177. doi:10.1371/journal.pcbi.1005177
80. Ronneberger O, Fischer P, Brox T. U-Net: Convolutional Networks for Biomedical Image Segmentation. In: Navab N, Hornegger J, Wells WM, Frangi AF,

eds. *Medical Image Computing and Computer-Assisted Intervention – MICCAI 2015*. Lecture Notes in Computer Science. Springer International Publishing; 2015:234-241. doi:10.1007/978-3-319-24574-4_28
81. Levine JH, Simonds EF, Bendall SC, et al. Data-driven phenotypic dissection of AML reveals progenitor-like cells that correlate with prognosis. *Cell*. 2015;162(1):184-197. doi:10.1016/j.cell.2015.05.047
82. Qiu P, Simonds EF, Bendall SC, et al. Extracting a cellular hierarchy from high-dimensional cytometry data with SPADE. *Nat Biotechnol*. 2011;29(10):886-891. doi:10.1038/nbt.1991
83. Windhager J, Bodenmiller B, Eling N. An end-to-end workflow for multiplexed image processing and analysis. Published online November 13, 2021:2021.11.12.468357. doi:10.1101/2021.11.12.468357
84. Eling N, Damond N, Hoch T, Bodenmiller B. cytomapper: an R/Bioconductor package for visualization of highly multiplexed imaging data. *Bioinforma Oxf Engl*. 2021;36(24):5706-5708. doi:10.1093/bioinformatics/btaa1061
85. Schett G, Neurath MF. Resolution of chronic inflammatory disease: universal and tissue-specific concepts. *Nat Commun*. 2018;9(1):3261. doi:10.1038/s41467-018-05800-6
86. McGrath EE, Marriott HM, Lawrie A, et al. TNF-related apoptosis-inducing ligand (TRAIL) regulates inflammatory neutrophil apoptosis and enhances resolution of inflammation. *J Leukoc Biol*. 2011;90(5):855-865. doi:10.1189/jlb.0211062
87. Brown SB, Savill J. Phagocytosis triggers macrophage release of Fas ligand and induces apoptosis of bystander leukocytes. *J Immunol Baltim Md 1950*. 1999;162(1):480-485.
88. Morioka S, Perry JSA, Raymond MH, et al. Efferocytosis induces a novel SLC program to promote glucose uptake and lactate release. *Nature*. 2018;563(7733):714-718. doi:10.1038/s41586-018-0735-5
89. Sugimoto MA, Sousa LP, Pinho V, Perretti M, Teixeira MM. Resolution of Inflammation: What Controls Its Onset? *Front Immunol*. 2016;7. Accessed July 19, 2023. https://www.frontiersin.org/articles/10.3389/fimmu.2016.00160
90. Chen M, Tse G, Wong WT. Interleukin-4 increases phagocytosis of necrotic cells by macrophages through scavenger receptor CD36. *Clin Exp Pharmacol Physiol*. Published online August 27, 2020. doi:10.1111/1440-1681.13399
91. Kolaczkowska E, Kubes P. Neutrophil recruitment and function in health and inflammation. *Nat Rev Immunol*. 2013;13(3):159-175. doi:10.1038/nri3399
92. Lastrucci C, Baillif V, Behar A, et al. Molecular and cellular profiles of the resolution phase in a damage-associated molecular pattern (DAMP)-mediated peritonitis model and revelation of leukocyte persistence in peritoneal tissues. *FASEB J*. 2015;29(5):1914-1929. doi:10.1096/fj.14-259341
93. Murray PJ, Wynn TA. Protective and pathogenic functions of macrophage subsets. *Nat Rev Immunol*. 2011;11(11):723-737. doi:10.1038/nri3073
94. Okabe Y, Medzhitov R. Tissue-specific signals control reversible program of localization and functional polarization of macrophages. *Cell*. 2014;157(4):832-844. doi:10.1016/j.cell.2014.04.016
95. Dolitzky A, Shapira G, Grisaru-Tal S, et al. Transcriptional Profiling of Mouse Eosinophils Identifies Distinct Gene Signatures Following Cellular Activation. *Front*

Immunol. 2021;12. Accessed March 12, 2023. https://www.frontiersin.org/articles/10.3389/fimmu.2021.802839
96. Andreev D, Liu M, Kachler K, et al. Regulatory eosinophils induce the resolution of experimental arthritis and appear in remission state of human rheumatoid arthritis. *Ann Rheum Dis*. 2021;80(4):451-468. doi:10.1136/annrheumdis-2020-218902
97. Simon HU, Yousefi S, Germic N, et al. The Cellular Functions of Eosinophils: Collegium Internationale Allergologicum (CIA) Update 2020. *Int Arch Allergy Immunol*. 2020;181(1):11-23. doi:10.1159/000504847
98. Leiferman KM, Peters MS. Eosinophil-Related Disease and the Skin. *J Allergy Clin Immunol Pract*. 2018;6(5):1462-1482.e6. doi:10.1016/j.jaip.2018.06.002
99. Radonjic-Hoesli S, Brüggen MC, Feldmeyer L, Simon HU, Simon D. Eosinophils in skin diseases. *Semin Immunopathol*. 2021;43(3):393-409. doi:10.1007/s00281-021-00868-7
100. Kenne E, Erlandsson A, Lindbom L, Hillered L, Clausen F. Neutrophil depletion reduces edema formation and tissue loss following traumatic brain injury in mice. *J Neuroinflammation*. 2012;9:17. doi:10.1186/1742-2094-9-17
101. Suo J, Linke B, Meyer dos Santos S, et al. Neutrophils mediate edema formation but not mechanical allodynia during zymosan-induced inflammation. *J Leukoc Biol*. 2014;96(1):133-142. doi:10.1189/jlb.3A1213-628R
102. Kim YH, Park CS, Lim DH, et al. Antiallergic effect of anti-Siglec-F through reduction of eosinophilic inflammation in murine allergic rhinitis. *Am J Rhinol Allergy*. 2013;27(3):187-191. doi:10.2500/ajra.2013.27.3866
103. Junttila IS. Tuning the Cytokine Responses: An Update on Interleukin (IL)-4 and IL-13 Receptor Complexes. *Front Immunol*. 2018;9. Accessed March 12, 2023. https://www.frontiersin.org/articles/10.3389/fimmu.2018.00888
104. Fulkerson PC, Fischetti CA, McBride ML, Hassman LM, Hogan SP, Rothenberg ME. A central regulatory role for eosinophils and the eotaxin/CCR3 axis in chronic experimental allergic airway inflammation. *Proc Natl Acad Sci U S A*. 2006;103(44):16418-16423. doi:10.1073/pnas.0607863103
105. Piehler D, Stenzel W, Grahnert A, et al. Eosinophils Contribute to IL-4 Production and Shape the T-Helper Cytokine Profile and Inflammatory Response in Pulmonary Cryptococcosis. *Am J Pathol*. 2011;179(2):733-744. doi:10.1016/j.ajpath.2011.04.025
106. Diny NL, Baldeviano GC, Talor MV, et al. Eosinophil-derived IL-4 drives progression of myocarditis to inflammatory dilated cardiomyopathy. *J Exp Med*. 2017;214(4):943-957. doi:10.1084/jem.20161702
107. Sasse C, Barinberg D, Obermeyer S, Debus A, Schleicher U, Bogdan C. Eosinophils, but Not Type 2 Innate Lymphoid Cells, Are the Predominant Source of Interleukin 4 during the Innate Phase of Leishmania major Infection. *Pathog Basel Switz*. 2022;11(8):828. doi:10.3390/pathogens11080828
108. Wang N, Liang H, Zen K. Molecular Mechanisms That Influence the Macrophage M1–M2 Polarization Balance. *Front Immunol*. 2014;5. Accessed March 12, 2023. https://www.frontiersin.org/articles/10.3389/fimmu.2014.00614
109. Wills-Karp M, Finkelman FD. Untangling the Complex Web of IL-4– and IL-13–Mediated Signaling Pathways. *Sci Signal*. 2008;1(51):pe55-pe55. doi:10.1126/scisignal.1.51.pe55

110. Gray MJ, Poljakovic M, Kepka-Lenhart D, Morris SM. Induction of arginase I transcription by IL-4 requires a composite DNA response element for STAT6 and C/EBPβ. *Gene*. 2005;353(1):98-106. doi:10.1016/j.gene.2005.04.004
111. Wang LM, Myers MG, Sun XJ, Aaronson SA, White M, Pierce JH. IRS-1: Essential for Insulin- and IL-4-Stimulated Mitogenesis in Hematopoietic Cells. *Science*. 1993;261(5128):1591-1594. doi:10.1126/science.8372354
112. Jiménez-Garcia L, Herránz S, Luque A, Hortelano S. Critical role of p38 MAPK in IL-4-induced alternative activation of peritoneal macrophages. *Eur J Immunol*. 2015;45(1):273-286. doi:10.1002/eji.201444806
113. Daseke MJ, Tenkorang-Impraim MAA, Ma Y, et al. Exogenous IL-4 shuts off pro-inflammation in neutrophils while stimulating anti-inflammation in macrophages to induce neutrophil phagocytosis following myocardial infarction. *J Mol Cell Cardiol*. 2020;145:112-121. doi:10.1016/j.yjmcc.2020.06.006
114. Szanto A, Balint BL, Nagy ZS, et al. STAT6 transcription factor is a facilitator of the nuclear receptor PPARγ-regulated gene expression in macrophages and dendritic cells. *Immunity*. 2010;33(5):699-712. doi:10.1016/j.immuni.2010.11.009
115. Huang JT, Welch JS, Ricote M, et al. Interleukin-4-dependent production of PPAR-gamma ligands in macrophages by 12/15-lipoxygenase. *Nature*. 1999;400(6742):378-382. doi:10.1038/22572
116. Park SY, Jung MY, Lee SJ, et al. Stabilin-1 mediates phosphatidylserine-dependent clearance of cell corpses in alternatively activated macrophages. *J Cell Sci*. 2009;122(Pt 18):3365-3373. doi:10.1242/jcs.049569
117. Korns D, Frasch S, Fernandez-Boyanapalli R, Henson P, Bratton D. Modulation of Macrophage Efferocytosis in Inflammation. *Front Immunol*. 2011;2. Accessed March 12, 2023. https://www.frontiersin.org/articles/10.3389/fimmu.2011.00057
118. Egholm C, Heeb LEM, Impellizzieri D, Boyman O. The Regulatory Effects of Interleukin-4 Receptor Signaling on Neutrophils in Type 2 Immune Responses. *Front Immunol*. 2019;10. Accessed March 12, 2023. https://www.frontiersin.org/articles/10.3389/fimmu.2019.02507
119. Seki T, Kumagai T, Kwansa-Bentum B, et al. Interleukin-4 (IL-4) and IL-13 Suppress Excessive Neutrophil Infiltration and Hepatocyte Damage during Acute Murine Schistosomiasis Japonica. *Infect Immun*. 2012;80(1):159-168. doi:10.1128/IAI.05581-11
120. Panda SK, Wigerblad G, Jiang L, et al. IL-4 controls activated neutrophil FcγR2b expression and migration into inflamed joints. *Proc Natl Acad Sci U S A*. 2020;117(6):3103-3113. doi:10.1073/pnas.1914186117
121. Woytschak J, Keller N, Krieg C, et al. Type 2 Interleukin-4 Receptor Signaling in Neutrophils Antagonizes Their Expansion and Migration during Infection and Inflammation. *Immunity*. 2016;45(1):172-184. doi:10.1016/j.immuni.2016.06.025
122. Choy DF, Hart KM, Borthwick LA, et al. TH2 and TH17 inflammatory pathways are reciprocally regulated in asthma. *Sci Transl Med*. 2015;7(301):301ra129. doi:10.1126/scitranslmed.aab3142

Schriftliche Erklärung

Ich erkläre ehrenwörtlich, dass ich die dem Fachbereich Medizin der Johann Wolfgang Goethe-Universität Frankfurt am Main zur Promotionsprüfung eingereichte Dissertation mit dem Titel

The organization of microenvironments by eosinophil granulocytes and macrophages during local inflammation

im Institut für Klinische Pharmakologie unter Betreuung und Anleitung von Prof. Dr. Dr. Klaus Scholich mit Unterstützung durch Prof. Dr. Andreas Weigert ohne sonstige Hilfe selbst durchgeführt und bei der Abfassung der Arbeit keine anderen als die in der Dissertation angeführten Hilfsmittel benutzt habe. Darüber hinaus versichere ich, nicht die Hilfe einer kommerziellen Promotionsvermittlung in Anspruch genommen zu haben.

Ich habe bisher an keiner in- oder ausländischen Universität ein Gesuch um Zulassung zur Promotion eingereicht. Die vorliegende Arbeit wurde bisher nicht als Dissertation eingereicht.

Vorliegende Ergebnisse der Arbeit wurden in folgendem Publikationsorgan veröffentlicht:

Kolbinger A, Schäufele TJ, Steigerwald H, Friedel J, Pierre S, Geisslinger G, Scholich K. Eosinophil-derived IL-4 is necessary to establish the inflammatory structure in innate inflammation. EMBO Molecular Medicine. 2023;15(2):e16796.

Kolbinger A, Kestner RI, Jencio L, Schäufele TJ, Vutukuri R, Pfeilschifter W, Scholich K. Behind the Wall - Compartment-Specific Neovascularisation during Post-Stroke Recovery in Mice. Cells. 2022;11(10):1659.

_____ _____

(Ort, Datum) (Unterschrift)